Sandro Wieser, BSc

# Thermal conductivity in metal-organic frameworks based on molecular and lattice dynamics simulations

**MASTER'S THESIS**

to achieve the university degree of

Diplom-Ingenieur

Master's degree programme: Advanced Materials Science

submitted to

**Graz University of Technology**

Supervisor

Ao.Univ.-Prof. Dipl.-Ing. Dr.techn. Egbert Zojer

Institute of Solid State Physics

Co-Supervisor
Dr. Natalia Bedoya-Martínez

Graz, September 2019

## AFFIDAVIT

I declare that I have authored this thesis independently, that I have not used other than the declared sources/resources, and that I have explicitly indicated all material which has been quoted either literally or by content from the sources used. The text document uploaded to TUGRAZonline is identical to the present master‘s thesis.

Date

Signature

# Abstract

Metal-Organic Frameworks (MOFs) represent a family of highly porous materials, that have shown promising properties for numerous applications including gas-storage and catalysis. As most of the applications for MOFs rely on the effectiveness of heat dissipation, it is crucial to investigate their thermal transport properties in detail. Since these materials allow for easy modifications in their structural composition and architecture, an in-depth understanding of the structure-to-property relationship will invite precise tailoring of the material to the individual requirements. To derive these relationships, molecular dynamics (MD) simulations are applied, employing specially designed empirical force fields to investigate heat transport for different configurations of MOFs varying the properties of the organic and inorganic components. Special care is taken to analyze the periodic interfaces between the individual segments occurring in MOFs, as they are identified as a major limiting factor for heat transport. It has been found that longer organic components lead to a reduction in thermal conductivity due to an increase of pore size. Additionally, reducing the large mass mismatch between organic and inorganic component, by utilizing lighter metals, leads to significant increases in thermal transport.

On more technical grounds, for the determination of thermal transport properties equilibrium and non-equilibrium MD methodologies have been employed in a complementary fashion. In order to carry out the simulations for all materials of interest, it was necessary to parameterize additional force-fields based on ab initio obtained reference data. Additionally, vibrational properties have been supplementarily investigated by using force-fields, in order to provide further analysis leading to a more generally applicable prediction of the thermal conductivity for different MOF morphologies. Using the Boltzmann transport equation within the relaxation time approximation, the thermal conductivity was also obtained by calculating the phonon lifetimes in the framework of lattice dynamics providing additional insight about the origin of thermal transport in MOFs.

# Kurzfassung

Metallorganische Gerüste (engl. Metal-Organic Frameworks, MOFs) stellen eine Familie von hoch porösen Materialien dar, die vielversprechende Eigenschaften für zahlreiche Anwendungen wie Gasspeicherung und Katalyse aufweisen. Nachdem sich die meisten dieser Anwendungen auf die Effektivität des Wärmeabtransportes verlassen, ist es entscheidend die Wärmetransporteigenschaften von MOFs im Detail zu untersuchen. Da diese Materialien einfache Abänderungen in deren strukturellen Komposition und Aufbau erlauben, wird ein tiefes Verständnis der Struktur-zu-Eigenschaft Relation dazu führen, MOFs für entsprechende Anforderungen zu entwerfen. Um diese Beziehungen zu erlangen, werden Molekulardynamik (MD) simulationen angewandt. Dazu werden speziell entworfene empirische Kraftfeldpotentiale verwendet, um den Wärmetransport für MOFs mit unterschiedlichen organischen und inorganischen Komponenten zu ermitteln. Besonders wert gelegt wurde auf die Auswertung der periodischen Verbindungspunkte der unterschiedlichen Komponenten der MOFs, da diese als ein wesentlich limitierender Faktor für den Wärmetransport identifiziert wurden. Es wurde ermittelt, dass längere organische Verbindungsstränge zu einer Verringerung der Wärmeleitfähigkeit aufgrund eines vergrößerten Leerraumes führt. Zusätzlich führt eine Reduktion des Massenverhältnisses zwischen den organischen und inorganischen Komponenten, indem leichtere Metallatome verwendet werden, zu einem signifikanten Anstieg der Wärmeleitfähigkeit.

Technisch wurde die Wärmeleitfähigkeit mithilfe von Gleichgewichts und nicht-Gleichgewichts MD Methodologien bestimmt. Um die Simulationen für alle Materialien von Interesse durchzuführen, war es notwendig zusätzliche Kraftfelder mithilfe von Ab-Initio basierenden Referenzdaten zu parametrisieren. Zusätzlich wurden Schwingungseigenschaften von MOFs untersucht, um zusätzliche Aspekte und mögliche Ursachen des Wärmetransportes zu analysieren. Zuletzt wurde die Wärmeleitfähigkeit durch Ermittlung der Phononen Lebensdauern bestimmt, was zusätzliche Auswertungsmöglichkeiten lieferte.

# Acknowledgements

Special thanks should be given to Tomas Kamencek, who provided the ab initio reference data and has been of great help throughout the entire thesis. Also, thanks should be given to Rochus Schmid and Johannes P. Dürholt for all their support in using MOF-FF, as well as for providing tools to create additional force-fields. Thanks is also given to the supervisors Egbert Zojer and Natalia O. Bedoya-Martínez, who provided support throughout the work.

The Graz, University of Technology is acknowledged for financial support through the Lead Project (LP-03), as well as the ThermOLED project (No. 848905) provided by the FFG. Lastly, the Vienna Scientific Cluster (VSC) is acknowledged for providing the computational resources required for this work.

# Contents

# 1 Introduction

Metal Organic Frameworks (MOFs) represent a group of crystalline materials that have gained a significant amount of attention in the recent years. They show promising properties for many applications like gas storage [1–3], gas separation [4, 5], drug delivery [6] and catalysis [7]. They also occur in many different forms leading to potential future applications utilizing their unique individual properties leading to favorable thermoelectricity [8, 9], semiconductivity [10, 11], piezoelectricity [12], ferroelectricity [13], magnetism [14] and to superconductivity [15], which can frequently be tuned by adjusting the MOF material. The reason for this broad field of different properties lies in their modular nature. They are materials consisting out of two different types of building blocks. One of them is an inorganic node – typically a metal-oxide – and the other is an organic linker, connecting the nodes with each other to form a highly porous crystalline material. The organic and inorganic building blocks are often connected to each other by a carboxylic acid group of the organic linker. This type of connection allows the linkers to be changed easily without modifying the connecting chemistry of the MOF. This makes them easily functionalizeable with various side groups, while maintaining their high internal surface area, making MOFs attractive for many of their applications. But there are also completely different types of MOFs, that do not rely on oxygen and use nitrogen, sulfur or other elements to form the inorganic node and its connection with the organic linkers. This work will focus on investigating the more "classical" MOFs based on metal oxides and aromatic organic linkers.
Many of the current and potential applications of MOFs involve chemical reactions or electric current, which inevitably lead to the generation of heat. For these processes to reach a high efficiency and to prevent large temperature fluctuations it is of importance that the utilized materials are capable of dissipating heat in a reasonable timeframe. Thermal transport can also be a major limiting factor for hydrogen storage [16]. This is especially important for MOFs since many of them suffer from a low thermal stability. Many current studies focus on creating new MOFs that are more thermally stable [17], but the framework of interest of any given application might not be as favorable. Contrary to this, a low thermal conductivity is desired in addition to a high electrical conductivity and a high Seebeck coefficient leading to favorable thermoelectricity. This leads to significant interest in studying and modeling transport properties in these materials. MOFs typically show poor

heat conduction [8, 18] and so far very few publications tried to understand the thermal conductivity in detail. In this work the focus will be to investigate some of these materials for their thermal transport properties and to attempt to explain those by applying computational methods.
Primarily, calculations will be carried out utilizing Molecular Dynamics (MD) simulations. There, equilibrium and non-equilibrium approaches will be applied. Complementary to the molecular dynamics results, internal vibrations, the phonons, which constitute the main carriers of heat in MOFs, will be analyzed by using lattice dynamics techniques. These will provide greater understanding about the origin of differences in heat transport. Since MOFs are relatively large and complex structures, classical force fields will be utilized to carry out the majority of simulations. These are required to save computational resources, especially for the MD simulations, which are prone to converge slowly or to suffer from significant finite size effects. Since the transferability of many force fields in the literature is questionable at best, only those, specifically developed for MOFs, will be used in this work. For a few materials of interest, additional force field parameters will be fitted based on density functional theory (DFT) obtained reference data. The objective is to use the acquired results to make statements on the thermal conductivity in metal-organic frameworks, while also remaining critical of the various methods that lead to these values. This is important, because the thermal conductivity is known to be an observable that is difficult to measure and simulate leading to large errors in many cases [19].

# 2 Metal-Organic Frameworks

This section should give an overview of the structures investigated in this work and the reasons why they were chosen. The primary goal is to provide structure-to-property relationships that help predicting the thermal conductivity of future MOFs. For this it is necessary to investigate several materials of similar geometry which differ in a systematic way.
MOFs exist in many different shapes and forms. Some of the simplest and most frequently investigated MOFs belong to the group of isoreticular metal-organic frameworks (IRMOFs), of which some examples are given in figure 2.1. The figures containing atomic structures used in this work were all created using the VESTA software [20]. IRMOFs are built from $M_4O$ nodes, where $M$ is the metal, with the same type of organic linkers in each direction forming a cubic structure. Most commonly, these MOFs are made with $Zn_4O$ nodes but possible replacements for $Zn$ include $Mg$ and $Ca$ [21]. The organic linkers belong to the group of the dicarboxylic acids with the most common one being terephthalic acid (TPH) which form the so-called IRMOF-1 (also referred to in literature as MOF-5). This MOF has been chosen as a starting point, as it was studied in many other publications and is one of the most well known MOFs. Other examples for linkers with this architecture that will be investigated in this work are oxalic acid (IRMOF-130), biphenyl-dicarboxylic acid (BPDC, IRMOF-10) and terphenyl-dicarboxylic acid (TPDC, IRMOF-16). This set of materials will be investigated in order to study the impact of linker length on heat transport. While this has been performed before to some extent [22], it will be studied in more detail and also serves as a starting point for further statements. In addition to changing the organic linkers connecting the inorganic nodes, it is also of interest how different metal atoms impact heat transport. While it is also possible to attach additional groups to the organic component, and there are also MOFs that form the inorganic nodes with other elements like sulfur or nitrogen instead of oxygen, but considering them would exceed the scope of this work. Inspired by the investigations for the different metal atoms, computational experiments have been carried out changing the masses of the linkers, which should be functionally similar to using a linker with additional functionalized groups, as the connecting chemistry would hardly be disturbed by such a modification.

One class of MOFs pictured in figure 2.2 will also be investigated in this work. These MOFs posses an entirely different inorganic building block with

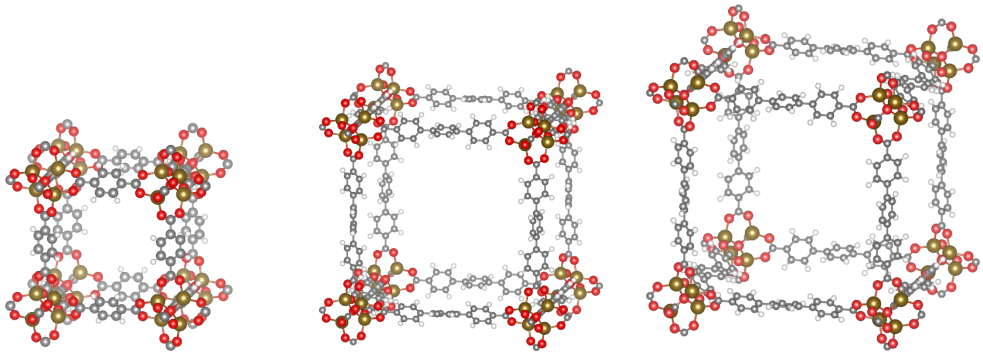

(a) IRMOF-1 (b) IRMOF-10 (c) IRMOF-16

Figure 2.1: Molecular structure of typical IRMOFS with different organic linkers. a) terephthalic acid, b) biphenyl-dicarboxylic acid and c) terphenyl-dicarboxylic acid

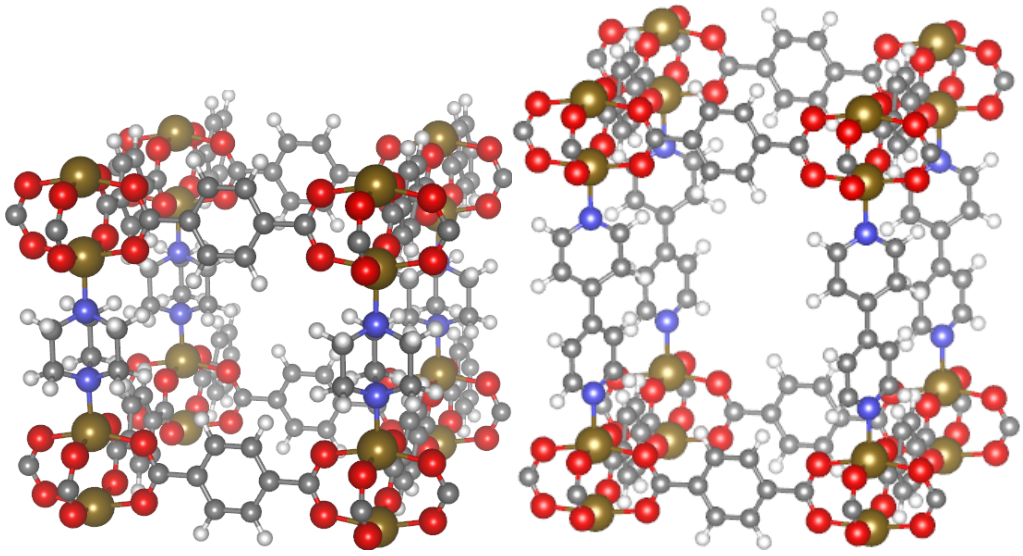

(a) JAST-1 (b) MOF-508

Figure 2.2: Molecular structures of JAST-1 and MOF-508 with a paddle-wheel node forming a pillar structure with nitrogen based linkers.

only two metal atoms that form a so-called paddlewheel structure with the oxygen atoms from the organic components. In two directions, the linkers of these systems are of the same type as for the IRMOFs – a terephthalic acid

– while in one direction a nitrogen atom connects the organic linker directly to the metal atoms on either side of the linker. These are commonly referred to as pillared MOFs. Examples for the organic building blocks in this architecture are bipyridine (forming MOF-508) and 1,4-Diazabicyclo[2.2.2]octane (DABCO, forming JAST-1). Common metals for these structures are $Cu$ and $Zn$, but only the zinc variant will be considered in this work. These MOFs have been chosen alongside the IRMOFs as they are tetragonal, making them relatively easy to compare. Another reason is, that they have a different type of organic-inorganic connecting chemistry, making it interesting to observe different interactions at the interfaces between the building blocks. Moreover, MOF-508 has shown promising adsorption properties in the past [23] and has been successfully synthesized in many instances. JAST-1 also possesses high adsorption capacity and is of interest for the process of polymerization [24].
It is important to note that many MOFs do not occur in such straightforward and simple geometries. Linkers do not always strictly connect to two inorganic nodes and the geometry is often far from cubic. This is why the last MOF that will be considered is MOF-74, which is depicted in figure 2.3. This structure deviates strongly from the previously considered MOFs, both in shape and in its properties. It consists of hexagonal linker-node clusters stacked on top of each other. The organic linkers mainly consist of an aromatic ring. But they are now connected at four different points to the inorganic nodes. Two of these connections are accomplished with a carboxylic acid like previously, while the other two involve an oxygen atom directly connected to the aromatic ring. These linkers form the faces of the hexagonal cell. The inorganic nodes at the corners of the hexagon contain three zinc atoms, each connected to four oxygens, which all connect to the organic linkers. These inorganic components are stacked on top of each other in three alternating configurations without a linker in between. This leads to some sort of helical node-chain that elongates itself through the entire length of the MOF. Its many connections and the fact that the linker-node structure only expands in two dimension, makes this a much more rigid MOF than those mentioned before. This is also a material that has been thoroughly investigated before and has gained attention for its gas adsorption properties [24].

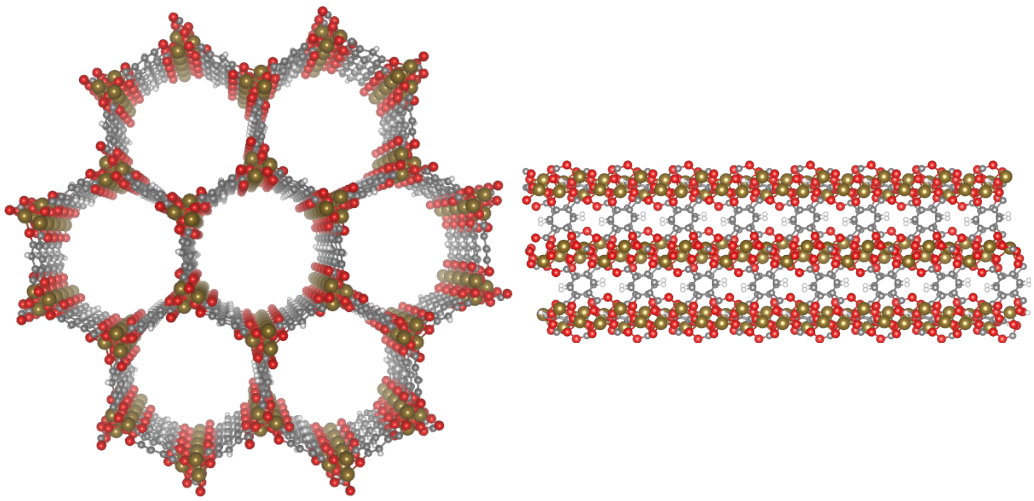

Figure 2.3: Molecular structures of MOF-74 from a top and side perspective.

# 3 Computational Methods and Theory

This section serves as an introduction to the fundamental theory of thermal conductivity and how it can be calculated. In addition, the computational methods used in this work will be introduced. Additionally, their ability to aid the prediction of properties in materials will be described.

## 3.1 Lattice thermal conductivity

Early in the history of physics most correlations between observables have been obtained by phenomenological observations of nature. The thermal conductivity $\kappa$ represents one of these cases and correlates a temperature gradient $\nabla T$ to the heat flux $J$ through a material. This expression is commonly known as Fourier's law.

$$\mathbf{J} = -\kappa_{ij} \nabla T \tag{3.1}$$

Since then this initially phenomenological proportionality constant has been investigated with modern methods. Expressions have been derived describing how thermal transport depends on other properties of solids. The two major contributions to the thermal conductivity arise due to phononic or electronic heat transport. Typically $\kappa$ is low for electrically insulating materials, but there are exceptions, like AlN that show a relatively large thermal conductivity under certain conditions [25]. Since the materials to be investigated – the metal-organic-frameworks – typically possess a low electrical conductivity [26], heat transport will arise from phonons. The basic considerations portrayed in below, follow a book by Ibach and Lüth [27]. Just as for electronic transport and many other transport properties, the Boltzmann transport equation (BTE) can be applied for phononic heat transport. It covers a change in a distribution function $f$ over time due to external forces, diffusion of particles and their collisions with each other.

$$\frac{df}{dt} = \left.\frac{\partial f}{\partial t}\right|_{ext} + \left.\frac{\partial f}{\partial t}\right|_{diff} + \left.\frac{\partial f}{\partial t}\right|_{coll} \tag{3.2}$$

We begin the considerations by assuming no external forces and neglecting the first term. The collision term can be approximated by the relaxation

time approximation (RTA) which introduces the relaxation time $\tau$.

$$\left.\frac{\partial f}{\partial t}\right|_{coll} = -\frac{f - f_0}{\tau} \tag{3.3}$$

This describes the function $f$ eventually returning to its equilibrium condition $f_0$. The relaxation time serves to define the speed of this process. The diffusive term can be expressed as

$$\left.\frac{\partial f}{\partial t}\right|_{diff} = -\mathbf{v} \cdot \nabla f \tag{3.4}$$

where $\mathbf{v}$ is the group velocity. The transport function's gradient $\nabla f$ can then be related to the temperature gradient leading, under stationary conditions, to the following expression of the Boltzmann transport equation:

$$\frac{df}{dt} = -\mathbf{v} \cdot \frac{\partial f_0}{\partial T} \nabla T - \frac{f - f_0}{\tau} \tag{3.5}$$

In order to lead this to the actual transport property given by a proportionality law like equation 3.1, it is necessary to consider the corresponding flux quantity $\mathbf{J}$. For a wavelike particle, the flux can be described with the group velocity $\mathbf{v}$, the frequency $\omega_\lambda$ of each mode and the corresponding distribution function.

$$\mathbf{J} = \frac{1}{V} \sum_{\lambda} \mathbf{v}_\lambda \hbar \omega_\lambda f \tag{3.6}$$

Here $\lambda$ is used as an index for each phonon mode in a reciprocal grid of wave vectors $i\mathbf{q}$, $\hbar$ is the reduced Planck's constant and $V$ is the volume of the material in which the heat flux is observed. When using the expression for the distribution function from equation 3.5 one obtains for the heat flux:

$$J_i = \frac{1}{V} \sum_{\lambda} \hbar \omega_\lambda \tau_\lambda \mathbf{v}_{\lambda,i}^2 \frac{\partial f_{0,\lambda}}{\partial T} \frac{\partial T}{\partial x_i}. \tag{3.7}$$

For phononic heat transport, the equilibrium distribution function $f_0$ is given by the Bose-Einstein distribution.

$$f_0 = \frac{1}{\exp(\hbar \omega_\lambda / (k_B T)) - 1} \tag{3.8}$$

Here $k_B$ is the Boltzmann constant. If one now uses equation 3.7 with the Bose-Einstein distribution in Fourier's law, one can obtain the following expression for the thermal conductivity tensor.

$$\kappa_{ij} = \frac{1}{V} \sum_{\lambda} \mathbf{v}_{\lambda,i} \cdot \mathbf{v}_{\lambda,j} C_{\lambda} \tau_{\lambda} \tag{3.9}$$

with the mode heat capacity $C_\lambda$ given as

$$C_{\lambda} = k_B \left( \frac{\hbar \omega_{\lambda}}{k_B T} \right)^2 \frac{\exp(\hbar \omega_{\lambda} / (k_B T))}{[\exp(\hbar \omega_{\lambda} / (k_B T)) - 1]^2}. \tag{3.10}$$

In literature, equation 3.9 is frequently expressed using the mean free path of a phonon $l_\lambda = v_\lambda \tau_\lambda$ instead of the phonon lifetime. This is the distance a phonon has to traverse on average until a collision event occurs. It is a property that is also very important for converging cell sizes in atomistic simulations, as they should be large enough to encompass the phonon mean free for many observables of interest. It is also important to note, that this mode heat capacity in equation 3.10 is not the same as the classical heat capacity that can be obtained from its integral over the entire density of states in any given system. This is the heat capacity depending on the energy of each phonon mode. The shape of this function is depicted in figure 3.1 for different temperatures. The heat capacity is the easiest component of the thermal conductivity to calculate, as it is only correlated to the system, by the phonon frequencies in reciprocal space. Another straightforward component, the group velocity, which is the derivative of the phonon dispersion curves in reciprocal space.

$$v_{\lambda,j} = \frac{\partial \omega_{\lambda}}{\partial q_j} \tag{3.11}$$

In the next section, a computational method will be presented which can be used to obtain the phonon frequencies in the first Brillouin zone for each normal mode. Subsequently, the most difficult component to obtain in equation 3.9 will be discussed, the phonon lifetime.

## 3.2 Lattice Dynamics

In the previous section the thermal conductivity based on phonon transport has been introduced. For calculating it, it is necessary to obtain the phonon frequencies and lifetimes for the system of interest. The considerations for

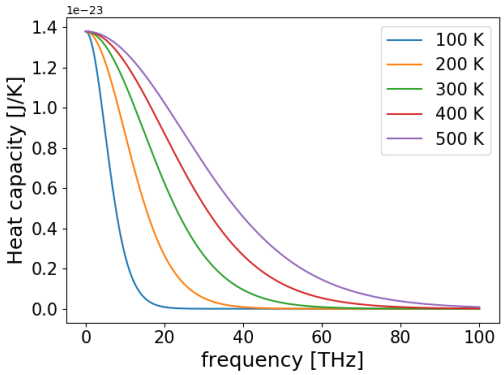


Figure 3.1: Mode heat capacity for various temperatures depending on frequency.

harmonic phonon calculations are taken from [27] while the background for anharmonic effects is taken from [28,29]. First we will focus on how to obtain the phonon band structure with atomistic simulations. For this, Newton's equations of motion have to be solved for all atoms in the system. It is necessary to describe all forces between the atoms. The most straightforward way of achieving this, is by imagining the interatomic interactions in the form of springs. These should not only be considered pairwise but for all many-body interactions. For obtaining the individual spring constants, the impact of displacing one or multiple atoms relative to the other atoms has to be investigated. Therefore, it is necessary to describe the potential energy $\phi$ of the system as a function of the displacements and coordinates of all the individual atoms. This is generally achieved in form of a Taylor series expansion.

$$\begin{aligned}\Phi(\mathbf{r}+\mathbf{u}) = \Phi(\mathbf{r}) &+ \frac{1}{2}\sum_{n\alpha i}\sum_{m\beta j}\frac{\partial^2\Phi}{\partial r_{n\alpha i}\partial r_{m\beta j}}u_{n\alpha i}u_{m\beta j} \\ &+ \frac{1}{6}\sum_{n\alpha i}\sum_{m\beta j}\sum_{o\gamma k}\frac{\partial^3\Phi}{\partial r_{n\alpha i}\partial r_{m\beta j}\partial r_{o\gamma k}}u_{n\alpha i}u_{m\beta j}u_{o\gamma k} + \ldots\end{aligned} \tag{3.12}$$

Here $n$, $m$ and $o$ indicate the unit cell the atom is located in, $\alpha$, $\beta$ and $\gamma$ represent the index of the atom in its respective primitive unit cell, $i$, $j$ and $k$ are the Cartesian indices, $\mathbf{r}$ are the coordinates of an atom and $\mathbf{u}$ the displacement. It is necessary to include interactions with atoms from adjacent

unit cells, hence the specific indices. This form includes terms up to the third order. For the initial considerations we will only consider terms up to the second order. Then this potential merely describes a harmonic oscillator for a many particle system and this is known as the harmonic approximation. The derivatives of the potential are known as the force constants

$$\Phi_{n\alpha i,m\beta j} = \frac{\partial^2 \Phi}{\partial r_{n\alpha i} \partial r_{m\beta j}}. \tag{3.13}$$

We will now consider the equations of motions. For a displacement $u_{n\alpha i}$, the sum of all forces resulting from interactions with other atoms and the inertia force has to be zero.

$$m_\alpha \ddot{u}_{n\alpha i} + \sum_{m\beta j} \Phi_{n\alpha i,m\beta j} u_{m\beta j} = 0 \tag{3.14}$$

Here $m_\alpha$ is the mass of the atom. This now results into $3N$ coupled differential equations, where $N$ is the total number of atoms. For periodic systems it is possible to describe the displacements in the form of a plane wave at the lattice points $\mathbf{r}_n$ with amplitude $y_{\alpha i}$.

$$u_{n\alpha i} = \frac{1}{\sqrt{m_\alpha}} y_{\alpha i}(\mathbf{q}) e^{i(\mathbf{q}\mathbf{r}_n - \omega t)} \tag{3.15}$$

When inserting this expression into equation 3.14 one obtains the following:

$$-\omega^2 y_{\alpha i}(\mathbf{q}) + \sum_{\beta j} \underbrace{\sum_m \frac{1}{\sqrt{m_\alpha m_\beta}} \Phi_{n\alpha i,m\beta j} e^{i\mathbf{q}(\mathbf{r}_m - \mathbf{r}_n)}}_{D_{\alpha i,\beta j}(\mathbf{q})} y_{\beta j}(\mathbf{q}) = 0 \tag{3.16}$$

This simplifies solving the equations of motion to a diagonalization problem of the so-called dynamical matrix $D_{\alpha i,\beta j}(\mathbf{q})$. This matrix is the summation over the cells $m$ in the equation above and is responsible for the coupling of the amplitudes of the waves with each other independent of $n$. This independence follows from the translational invariance of the lattice by its cell length, implying that the force constants are only allowed to depend on the difference between $m$ and $n$: $\Phi_{n\alpha i,m\beta j} = \Phi_{0\alpha i,(m-n)\beta j}$. This now leads to a linear homogeneous system of equations.

$$-\omega^2 y_{\alpha i}(\mathbf{q}) + \sum_{\beta j} D_{\alpha i,\beta j}(\mathbf{q}) y_{\alpha i}(\mathbf{q}) = 0 \tag{3.17}$$

This eigenvalue problem can be solved to directly obtain the phonon frequencies $\omega_\lambda$ and the corresponding eigenvectors $y_\lambda$ at every wave vector $\mathbf{q}$. This is now sufficient to describe two of the components required for the thermal conductivity in equation 3.9. With this, the mode heat capacity can be obtained from the density of states and the group velocities $v_{\lambda i}$ can now be obtained from the derivative of the eigenvalue equation.

$$v_{\lambda i} = \frac{\partial \omega_\lambda}{\partial q_i} = \frac{1}{2\omega_\lambda} \sum_{\alpha\beta jk} y_{\lambda\alpha j} \frac{\partial D_{\alpha j,\beta k}(\mathbf{q})}{\partial q_i} y_{\lambda\beta k} \tag{3.18}$$

But the phonon lifetimes cannot be obtained from harmonic force constant as they are an inherently anharmonic effect. They arise from the collision term in the BTE and for collisions to occur, at least three particles need to be involved at the same time. This is due to the requirement of conservation of energy and momentum. When one phonon scatters it has to split into at least two different phonons with the same amount of total energy and momentum. Thus at least terms of the third order have to be considered in the Taylor expansion in equation 3.12 to obtain the phonon scattering rates for three phonon processes $\xi_{\lambda\lambda'\lambda''}$. They can be obtained from equation 3.15 and the third order term in equation 3.14.

$$\begin{aligned}\xi_{\lambda\lambda'\lambda''} = \frac{1}{\sqrt{N}} \frac{1}{6} \sum_{\alpha\beta\gamma} \sum_{ijk} y_{\alpha i\lambda} y_{\beta j\lambda'} y_{\gamma k\lambda''} \sqrt{\frac{\hbar^3}{8 m_\alpha m_\beta m_\gamma \omega_\lambda \omega_{\lambda'} \omega_{\lambda''}}} \\ \cdot \sum_{mn} \Phi_{0\alpha i, m\beta j, n\gamma k} e^{i\mathbf{q}'(\mathbf{r}_{m\beta} - \mathbf{r}_{0\alpha})} e^{i\mathbf{q}''(\mathbf{r}_{n\gamma} - \mathbf{r}_{0\alpha})} e^{i(\mathbf{q}+\mathbf{q}'+\mathbf{q}'')\mathbf{r}_{0\alpha}} \Delta(\mathbf{q}+\mathbf{q}'+\mathbf{q}'')\end{aligned} \tag{3.19}$$

Here $\Delta(\mathbf{q}+\mathbf{q}'+\mathbf{q}'')$ is 1 when $\mathbf{q}+\mathbf{q}'+\mathbf{q}''$ is a reciprocal lattice vector, otherwise it is zero. $0\alpha$ refers to an atom in the primitive unit cell and $\Phi_{0\alpha i, m\beta j, n\gamma k}$ are the third order force constants. With help of many-body perturbation theory the imaginary self-energy $\Gamma_\lambda(\omega)$ can now be calculated up to second order [29]. This energy is equal to half the phonon linewidth and the phonon lifetimes can be obtained with $\tau_\lambda = 1/(2\Gamma_\lambda(\omega_\lambda))$.

$$\begin{aligned}\Gamma_\lambda(\omega) = \frac{18\pi}{\hbar^2} \sum_{\lambda'\lambda''} |\xi_{-\lambda\lambda'\lambda''}|^2 \{ (f_{0,\lambda'} + f_{0,\lambda''} + 1) \delta(\omega - \omega_{\lambda'} - \omega_{\lambda''}) \\ + (f_{0,\lambda'} - f_{0,\lambda''}) [\delta(\omega + \omega_{\lambda'} - \omega_{\lambda''}) - \delta(\omega - \omega_{\lambda'} + \omega_{\lambda''})] \}\end{aligned} \tag{3.20}$$

Here the $f_0$ is the Bose-Einstein distribution (equation 3.8) describing phonon occupation. It also is the factor responsible for the temperature dependence. Calculating this equation is not entirely straightforward, as it contains Dirac functions of three phonon processes. The collision processes are described by $[\delta(\omega + \omega_{\lambda'} - \omega_{\lambda''}) - \delta(\omega - \omega_{\lambda'} + \omega_{\lambda''})]$ and decay processes are included with $\delta(\omega - \omega_{\lambda'} - \omega_{\lambda''})$. The energies of the phonons involved in these processes show a continuous shape in reciprocal space, but these expressions have to be evaluated on a discrete grid of wave vectors. There are several methods to interpolate the energies in between the grid points. Commonly used are the smearing method and linear tetrahedron integration [30]. The latter is utilized in this work, as it does not rely on an arbitrary smearing width, that would have to be converged for each calculation.
With this, all components required for the thermal conductivity from lattice dynamics simulations are accounted for. But this formulation only includes three phonon processes. While these are the most dominant anharmonic contributions in many materials, there are also examples where higher order terms cannot be neglected [31, 32]. Molecular dynamics (MD) provides the tools to consider all anharmonic terms at once. There are several possible techniques available to extract the phonon lifetimes with the help of MD trajectories [33, 34]. But accurate MD simulations are expensive and these methods require long simulation times to converge and are often difficult to post process. Still, there are less convoluted ways to obtain the thermal conductivity using MD, which will be discussed in the next section.

## 3.3 Molecular Dynamics

Molecular Dynamics (MD) represents a method commonly applied to carry out dynamic atomistic simulations in computational chemistry and physics. It is based on solving the Newtonian equations of motion for a large amount of sequential time steps. Especially for deriving thermal transport in materials dominated by phonon transport, molecular dynamics has the significant advantage of completely describing all many body interactions that can be captured by the interatomic model. This results in a proper description of scattering mechanisms without further approximations, for as long as the simulation cell is sufficiently large.

The core of these simulations is a time integrator solving the equations of motion and propagating the system as a function of time. This has to be performed for discrete timesteps and, therefore, requires numerical integrators. Most commonly applied in MD is the velocity Verlet integrator [35, 36].

$$\mathbf{r}_i(\Delta t) = \mathbf{r}_i(0) + \Delta t \frac{\mathbf{p}_i(0)}{m_i} + \frac{\Delta t^2}{2m_i}\mathbf{F}_i(\mathbf{r}(0)) \tag{3.21}$$

$$\mathbf{p}_i(\Delta t) = \mathbf{p}_i(0) + \frac{\Delta t}{2}[\mathbf{F}_i(\mathbf{r}(0)) + \mathbf{F}_i(\mathbf{r}(\Delta t))] \tag{3.22}$$

Where $\mathbf{p}_i$ are the momenta, $\mathbf{r}_i$ are the atom coordinates and $\mathbf{F}_i$ are the forces acting on an atom. Velocity Verlet is typically chosen because of its good numerical stability, ease of implementation and application, as well as a relatively low computational cost at an acceptable error. There are other possibilities like the reversible reference system propagator algorithm (r-RESPA) [35] that are more computationally efficient, but require significant additional effort to set up. Regardless of the algorithm used, a suitable timestep has to be defined, depending on the system. It should be small enough to allow all motions of the atoms that would occur in a real system. On the other hand, a larger timestep results in lower computational cost. A guideline for the choice can be provided by the highest frequency modes in the phonon density of states. These lie in the THz range which leads to vibrations that require time steps in the femtosecond range to describe properly. A commonly applied rule of thumb is to choose a timestep depending on the highest vibrational frequency occuring int the system as $\Delta t = 1/(10 \cdot f_max)$. Following this, for the case of organic molecules, that typically show carbon-hydrogen stretches at around 90-100 THz, a timestep

of 1 fs should be appropriate. But this is not always applicable, as MOFs demanded an even smaller timestep, even though they do not show any higher frequencies.
In order to ensure that the molecular dynamics simulations represent motions that are representative of realistic temperatures, one has to define thermostats. They serve to equilibrate the system of interest before the simulations at a desired temperature. This is achieved in an NVT (constant number of atoms, volume and temperature) ensemble. Additionally, thermostats serve to control the evolution of temperature during non-equilibrium simulations. Many thermostats can be given in a general form starting with the Hamiltonian equations of motion.

$$\dot{\mathbf{r}}_i = \frac{\mathbf{p}_i}{m_i} \tag{3.23}$$

Where the momentum $\mathbf{p}_i$ can be described as the sum of the force on each particle given by interatomic interactions $\mathbf{F}_i$ and the force $\mathbf{F}_i^T$ given by the thermostat.

$$\mathbf{p}_i = \mathbf{F}_i + \mathbf{F}_i^T \tag{3.24}$$

Many different statistical approaches to define these forces have been used with molecular dynamics in mind. One of the most commonly applied thermostats is the Nose-Hoover thermostat [37, 38]. It deviates from the Hamiltonian equations of motion in that it introduces a scale variable $s$, in order to include an additional degree of freedom for the heat bath. This leads to the modified Nose-Hoover equations of motion.

$$\begin{aligned} \frac{d\mathbf{r}_i}{dt'} &= \frac{\mathbf{p}_i'}{m} \\ \frac{d\mathbf{p}_i'}{dt'} &= \mathbf{F}_i - \frac{\xi}{Q}\mathbf{p}_i' \\ \frac{d\xi}{dt'} &= \left(\sum_i \frac{p_i'^2}{m} - 3Nk_BT\right) \end{aligned} \tag{3.25}$$

with

$$\begin{aligned} \mathbf{p}_i' &= \frac{\mathbf{p}_i}{s} \\ t' &= \int_0^t dt/s \\ Q &= 3Nk_BT\tau^2 \end{aligned} \tag{3.26}$$

Here $\mathbf{p}_i'$ and $t'$ are the scaled momentum and time, $N$ is the number of atoms in the system and $Q$ is a fictitious mass parameter that represents the coupling strength that can be adjusted by choosing the time constant $\tau$ appropriately. A further expansion of this relatively simple approach is given by the Nose-Hoover chain equations [39] that introduced a chain of heat bath variables instead of just one in order to even out fluctuation of thermostat variables. The resulting Nose-Hoover chain thermostat is generally considered as one of the most reliable choices for equilibrium molecular dynamics simulations.
While efforts have been made in the development of thermostats that function outside of the classical limit [40, 41], this is barely explored and tested for complex, strongly anharmonic systems. This is the reason for the continued use of their classical counterparts. This means that it is important to analyze at which temperature quantum effects cease to matter. This is reached once the heat capacity converges to a constant only depending on the number density of atoms $n$.

$$C_v = \frac{3}{2} n k_B \tag{3.27}$$

Under these circumstances it can be ensured that low temperature quantum effects can be neglected. But for many crystalline materials the low frequency phonon modes show dominating contributions towards many physical observables. These are occupied at much lower temperatures than the often irrelevant high frequency modes. For this reason it is possible to perform correct molecular dynamics simulations long before the classical limit is reached. The temperature dependent heat capacity can not be obtained by means of classical molecular dynamics and, therefore, will be derived by lattice dynamics simulations as introduced in section 3.2.

Just like thermostats serve to force a certain temperature on a system, barostats are used to enforce a certain pressure. Conceptually, they function analogous to their thermal counterparts. The equations of motion are modified by an additional term including the pressure dependence. Just as with the thermostats there are several statistical approaches to achieve this. The Nose-Hoover chain barostat [36] is the only such approach employed in this

work.

$$\begin{aligned} \frac{d\mathbf{r}_i}{dt'} &= \frac{\mathbf{p}'_i}{m} + \frac{p_\epsilon}{W}\mathbf{r}_i \\ \frac{d\mathbf{p}_i}{dt'} &= \mathbf{F}_i - \left(1 + \frac{1}{N}\right)\frac{p_\epsilon}{W}\mathbf{p}_i \end{aligned} \tag{3.28}$$

Here $p_\epsilon$ is the sum of the Nose-Hoover chain. This concludes the introduction of some very basic tools employed in molecular dynamics simulations. In the following an introduction of methods to obtain the thermal conductivity will be given.

### 3.3.1 Non-equilibrium Molecular Dynamics

Non-equilibrium Molecular Dynamics (NEMD) provides the most straightforward method to obtain the thermal conductivity in atomistic simulations. It is inspired by experimental approaches to obtain thermal transport properties for macroscopic samples. Figure 3.2 represents a simulation box used in this approach. First the entire system has to be thermalized at the temperature of interest using a thermostat. Then two areas of the cell are respectively heated and cooled by adding and subtracting an equal amount of energy. After the system reaches steady state, it is possible to determine the heat flux flowing from the hot to the cold region as well as the temperature gradient occurring in the bulk of the system. This allows one to obtain the thermal conductivity as a scalar value in the direction of interest by directly using Fourier's law.
System sizes in NEMD simulations are small compared to realistic measurement setups. This leads to very large temperature gradients. Therefore, it is important to make sure that Fourier's law is valid for the chosen energy difference. This can be achieved by performing a simulation for several temperature differences $\Delta T$.
Several different approaches have been explored to properly achieve the temperature difference in the simulation box. Typically, the cell is divided into equally large slabs that correspond to the periodicity of the material of interest [42]. Then two of these slabs are defined as the cold and hot area with an equal spacing in between them when considering periodic boundary condition. It is now possible to either directly increase and reduce the kinetic energies of these areas [19] or to use thermostats at a certain temperature. There is also a technique involving the direct exchange of kinetic

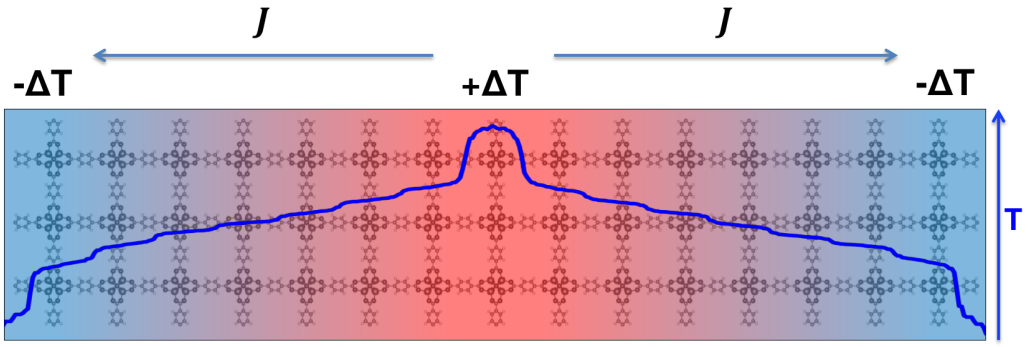


Figure 3.2: Temperature profile in a simulation cell during a NEMD simulation. A hot thermostat ($+\Delta T$) and a cold thermostat ($-\Delta T$) have been applied with periodic boundary conditions.

energy between the slabs which guarantees the conservation of energy [43]. A typical issue occurring for the methods based on scaling the kinetic energies and, therefore, the atomic velocities, is that the center-of-mass motion of the entire system has to remain zero throughout the simulation. Another flaw is that especially for rigid systems with high differences in masses of the individual atoms, as is the case in MOFs, the energy exchange between individual atoms can lead to thermal instabilities during the simulation. When utilizing thermostats, the conservation of energy is not inherently guaranteed, but once the system reaches steady state, the added and subtracted energy should converge to the same value. It is also of vital importance to choose the proper thermostat for NEMD simulations, as the boundary between thermostatted and non-thermostatted region has to be well defined.
A thermostat that has been proven to work well for non-equilibrium molecular dynamics simulations is the Langevin thermostat [44]. The added forces are given by a dissipative component $-\gamma \mathbf{v}_i$, where $\gamma$ is the friction coefficient, and a random force $\mathbf{F}_i^R(t)$.

$$\mathbf{p}_i = \mathbf{F}_i - \gamma \mathbf{v}_i + \mathbf{F}_i^R(t) \tag{3.29}$$

$\left\langle \mathbf{F}_i^R(t) \right\rangle$ has to be zero and

$$\left\langle F_{ia}^R(t) F_{jb}^R(t) \right\rangle = 2\gamma T k_B \delta_{ij} \delta_{ab} \delta(t - t') \tag{3.30}$$

defines the condition for selection of the random force component. Here $\gamma$ is the friction coefficient, $\mathbf{v}_i$ is the particle velocity, $i$ and $j$ are indices for the

particles and $a$ as well as $b$ are the Cartesian vector components.
A different phenomenon that can be observed in 3.2 is the steep temperature step occurring at the thermostat boundary. This arises due to phonon scattering at the interface between thermostatted and non-thermostatted region. It leads to severe finite size effects if the cell is not significantly larger than the mean-free-path [19]. The thermal conductivity is then reduced based on an effective mean free path $l_{eff}$ that can be reached given a certain cell length $L_x$. There is a solution to this problem other than using massive simulation boxes. It is possible to correlate the inverse effective mean-free-path with the inverse cell length and infinite mean-free-path $l_\infty$.

$$\frac{1}{l_{eff}} = \frac{1}{l_\infty} + \frac{4}{L_x} \tag{3.31}$$

In periodic NEMD simulation the system's bulk is cut in half on either side of the source and sink. A phonon should be able to travel half the distance between the heated and cooled region until it meets a scattering center. And therefore the average phonon travel amounts to $L_x/4$ assuming small thermostat regions. With equation 3.31 it is possible to specify an expression that estimates the thermal conductivity based on the simulation box length. For this the expression for the heat capacity in the classical limit (equation 3.27) and for the thermal conductivity (equation 3.9) for all phonons in the system given as $\kappa = 1/3 C_v v_g l$ are used to obtain

$$\frac{1}{\kappa_{eff}} = \frac{a^3}{4 k_B v_G} \left( \frac{1}{l_\infty} + \frac{4}{L_x} \right). \tag{3.32}$$

When the length of the cell $L_x$ approaches infinite, we should be able to obtain the thermal conductivity. This can be achieved by extrapolating a linear fit over several effective thermal conductivity values for several different cell lengths $L_x$ in the infinite size limit [19]. This necessity in addition with the fact that one obtains only the thermal conductivity in one direction of the simulation cell makes this method much more expensive than equilibrium molecular dynamics simulations.

### 3.3.2 Equilibrium Molecular Dynamics

It is also possible to obtain the thermal conductivity from an Equilibrium Molecular Dynamics (EMD) simulation by observing fluctuations in the heat

current. This is generally the preferred method for obtaining the thermal conductivity, as the entire thermal conductivity tensor can be calculated in a single simulation.
The method is based on the fluctuation dissipation theorem [45] that provides a relation between physical observables and their response function based on fluctuations in a balanced field. This method has widely been applied for many different transport properties [46]. It is again based on the basic empirically found expression relating a flux of an observable with its corresponding field, like Fourier's law (equation 3.1). For the thermal conductivity, such a relation is given by

$$\kappa_{ij} = \frac{V}{k_B T^2} \int_0^\infty \langle J_i(0) \cdot J_j(t) \rangle \, dt. \tag{3.33}$$

Here $V$ is the cell volume and $\langle \mathbf{J}(0) \cdot \mathbf{J}(t) \rangle$ is the heat current autocorrelation function (HCACF). This expression describes the time response of heat fluctuations in equilibrium. The correlation function decays more slowly for high values of the thermal conductivity. This means that the heat fluctuations inside the material are long lived, which can be due to a long phonon mean free path. In materials with low thermal conductivity, the phonon mean free path will be small and, therefore, the HCACF will decay quickly. The heat flux $\mathbf{J}$ can be obtained from the total energy of the atoms $E_i$, the atomic velocities $\mathbf{v}_i$ and the many-body stress tensor $\mathbf{S}_i$ from a molecular dynamics simulation.

$$\mathbf{J} = \frac{1}{V} \left[ \sum_i E_i \mathbf{v}_i - \sum_i \mathbf{S}_i \mathbf{v}_i \right] \tag{3.34}$$

Similar to NEMD, the Green-Kubo method suffers from finite size effects, when the simulation box is too small. But since no scattering centers due to thermostats arise utilizing this method, these are much less significant in equilibrium molecular dynamics simulations. In most cases it is not even necessary to calculate systems larger than the phonon mean free path [47] and box lengths of about 2 nm have been found to be sufficient. Nonetheless, very long simulation times are needed in order to properly converge the correlation functions.

## 3.4 Classical Force Fields

Molecular Dynamics simulations can become very expensive when applied to larger systems utilizing quantum mechanical methods like density functional theory (DFT) for calculating the forces. This is especially problematic for simulations to obtain the thermal conductivity that often require simulation times of several nanoseconds with time steps in the femtosecond range. Therefore, a lower level of theory is required to investigate many systems. Classical Force Fields are a commonly applied model to give an affordable and reasonably accurate description of the interatomic forces in large and complex systems like organics. They are typically defined as a potential energy expression. In this section the functional form of the force field utilized in this thesis will be presented and its parameterization procedure will be outlined.

### 3.4.1 The MOF-FF Force Field

The force field potential used in this work was chosen to be MOF-FF [48]. This is a flexible, first-principles derived force field specifically designed for metal-organic frameworks. MOF-FF is based on the MM3 [49] force field that has been developed for aliphatic hydrocarbons. Many modifications were made to the original in order to properly describe the inorganic components of MOFs and their interactions with the organic linkers. This section covers the individual contributions to the energy included in MOF-FF, while section 3.4.2 shows how the required parameters were obtained.
The potential energy $E_{pot}$ of the MOF-FF force field is defined in the following form:

$$\begin{aligned} E_{pot} = &\sum_{s} E_s^{str} + \sum_{b} \left( E_b^{bnd} + E_b^{str-str} + E_b^{str-bnd} \right) \\ &+ \sum_{t} E_t^{tor} + \sum_{o} E_o^{oop} + \sum_{n} \left( E_n^{coul} + E_n^{vdW} \right) \end{aligned} \tag{3.35}$$

with $E_{str}$ being the bond stretch potential between two atoms, $E_{bnd}$ the bending angle potential between three atoms, $E_{tor}$ the energy caused by the torsions between four atoms, $E_{oop}$ the out-of-plane bending potential between four atoms, $E_{coul}$ Coulomb's contribution due to the atomic charges and $E_{vdW}$ the van-der-Waals potential. The indices $s$, $b$, $t$ and $o$ represent all

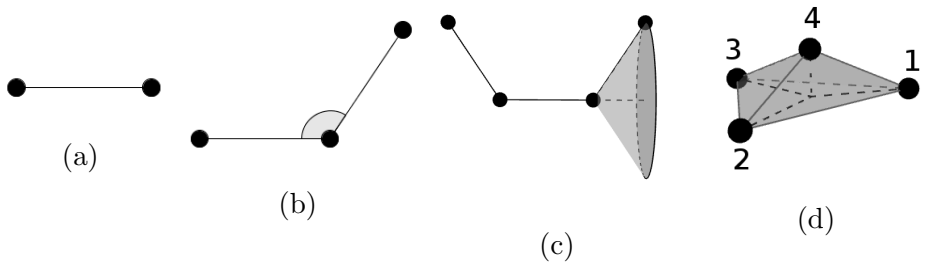


Figure 3.3: Overview of the geometrical interactions that have to be described by the force field. The bond stretches (a), the bending angles (b), the proper torsions (c) and the improper torsions, or out-of-plane bending angles (d).

occurrences of the respective interaction types and $n$ is an index representing all atomic pairs. These interactions are visualized in figure 3.3. $E_{str-str}$ and $E_{str-bnd}$ are stretch-stretch and stretch-bend contributions, which represent interactions between different bond stretches with each other or with a bending angle. These are typically referred to as cross-terms.
The bond stretches in the organic part of the MOFs are described by the quartic term originally used in the MM3 potential:

$$E_s^{str} = \frac{1}{2}k_s(r_s - r_s^{ref})^2 \left[1 - 2.55(r_s - r_s^{ref}) + \frac{7}{12}(2.55(r_s - r_s^{ref}))^2\right] \quad (3.36)$$

where $r_s$ is the bond length and $k_s$ and $r_s^{ref}$ are parameters. This term includes fixed anharmonicities that are derived to mimic a Morse potential as well as possible [49]. In case of the coordination covalent bonds that commonly occur in MOFs for bonds with the metal atoms, athe true Morse potential is used, which is beneficial for describing anharmonic effects.

$$E_s^{str} = \frac{1}{2\alpha}k_s\left[1 - \exp(-\alpha(r_s - r_s^{ref}))\right]^2 \quad (3.37)$$

This requires an additional parameter $\alpha$ that is calculated from the bond dissociation energy $E_{diss} = k_s/2\alpha^2$, that needs to be provided by external input like experiments and cannot be fitted from the harmonic reference data used in the parameterization procedure for MOF-FF, which will be outlined later.

The contributions from angle bending are considered with a polynomial of the sixth order:

$$E_b^{bnd} = \frac{1}{2}k_b(\theta_b - \theta_b^{ref})^2 \Big[1 - 0.014(\theta_b - \theta_b^{ref}) + 5.6 \cdot 10^{-5}(\theta_b - \theta_b^{ref})^2 \\ -7 \cdot 10^{-7}(\theta_b - \theta_b^{ref})^3 + 2.2 \cdot 10^{-8}(\theta_b - \theta_b^{ref})^4\Big] \tag{3.38}$$

with $\theta_b$ being the bond angle, $k_b$ a constant and $\theta_b^{ref}$ the reference angle. Torsions in the MOF-FF potentials are considered using the commonly applied Fourier series term up to fourth order.

$$E_t^{tor} = \sum_n \frac{V_t^n}{2}[1 + \cos(n\phi_t + \phi_t^n)] \tag{3.39}$$

Here $V_t^n$ is the force constant, $\phi_t$ the torsional angle and $\phi_t^n$ the phase shift. The out-of-plane bending angle $\theta_o$ obeys the Wilson-Decius (the atomic indices are labeled in figure 3.3d) definition

$$\sin\theta_o = \frac{r_{42} \cdot r_{43}}{\sin\varphi_1} r_{41}, \tag{3.40}$$

where $r_{41}$, $r_{42}$ and $r_{43}$ are the bond lengths in the four-body interaction and $\varphi_1$ is the angle between $r_{42}$ and $r_{43}$. The contributions from out-of-plane bending are included in the force field in the form of an harmonic term with a reference angle $\theta_0$:

$$E_o^{oop} = \frac{1}{2}k_o(\theta_o - \theta_0)^2 \tag{3.41}$$

Additional cross-terms are considered as three-body interactions in neighboring bonds. A stretch-stretch contribution as well as an asymmetric stretch-bend term are included in the force field.

$$E_b^{str-str} = k_{ss}(r_{b1} - r_{b1}^{ref})(r_{b2} - r_{b2}^{ref}) \tag{3.42}$$

$$E_b^{str-bnd} = (\theta_b - \theta_b^{ref})[k_{sb1}(r_{b1} - r_{b1}^{ref}) + k_{sb2}(r_{b2} - r_{b2}^{ref})] \tag{3.43}$$

Here $k_{ss}$, $k_{sb1}$ and $k_{sb2}$ are the additional force constants. The reference bond lengths and angles are the same as in the respective stretch or bending terms. Van der Waals interactions are modeled using a pairwise dispersion damped Buckingham potential. One of the major flaws in using the frequently used Lennard-Jones potential term is that the repulsive energy of the interaction is

overestimated for many systems. Buckingham potential terms solve this issue by including an exponential term providing a more accurate description in the repulsive regime. A traditional Buckingham term suffers from an artifact at very small distances where the potential shows a steep drop towards negative infinity. This can lead to instabilities during molecular dynamics simulations especially at high temperatures. This has been solved by dampening the dispersive interactions at close range. The final potential term is defined as

$$E_{ij}^{vdW} = \epsilon_{ij} \left\{ 1.85 \cdot 10^5 \exp\left(-12 \frac{d_{ij}}{d_{ij}^0}\right) - 2.25 \left(\frac{d_{ij}^0}{d_{ij}}\right)^6 \left[1 + 6 \left(\frac{0.25 d_{ij}^0}{d_{ij}}\right)^{14}\right]^{-1} \right\} \tag{3.44}$$

where $d_{ij}$ is the interatomic distance, $d_{ij}^0$ is the van der Waals minimum distance and $\epsilon_{ij}$ is the potential well depth. This term is only applied to pairwise interactions excluding nearest and next-nearest neighbors in the bonded structure.
Electrostatic interactions are included for atom pairs beyond the next-nearest neighbors in the form of spherical Gaussian charge distributions. They provide a significantly improved description compared to point charges in the inorganic part of the MOFs, where large differences in the atomic charges occur. The energy is given by

$$E_{ij}^{coul} = \frac{1}{4\pi\epsilon} q_i q_j \frac{\operatorname{erf}\left(\frac{d_{ij}}{\sigma_{ij}}\right)}{d_{ij}} \tag{3.45}$$

with $d_{ij}$ the interatomic distance, $q_i$ and $q_j$ the atomic point charges and $\sigma_{ij}$ the Gaussian charge distribution width calculated from its values of the individual atom types $\sigma_{ij} = \sqrt{\sigma_i^2 + \sigma_j^2}$. This interaction models a Gaussian radial distribution of the charges surrounding the atomic coordinates.

### 3.4.2 Parameterization of Force Fields

MOF-FF in its original form is a force field that sacrifices most of its transferability for accuracy. This implies that every single building block (the nodes and linkers) and every single connection between them in MOFs of

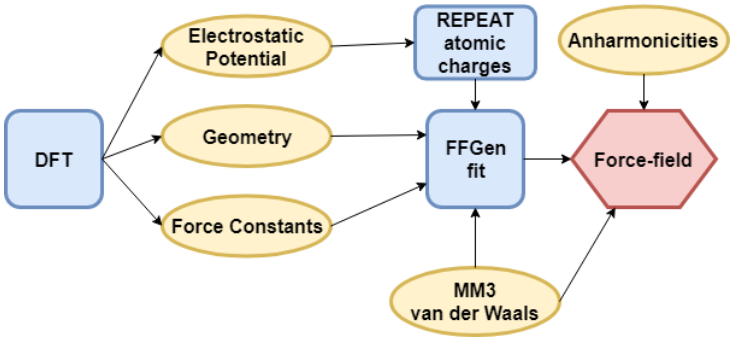


Figure 3.4: Flowchart for the general fitting procedure leading to the force field.

interest require their own specific set of parameters. As a consequence, only a limited amount of MOFs were parameterized in the original force field. Among the systems of interest in this thesis, this includes the $Zn_4O$ nodes, the Zn-paddlewheel nodes, phenyl, biphenyl and terphenyl based linkers for both types of MOFs, as well as the DABCO-linker for paddlewheel MOFs. When investigating the thermal properties of MOFs, we are also interested in systems that were not initially considered in MOF-FF. These require additional parameterization. In this section, a procedure for fitting force-field parameters will be presented that has also been used in a similar form to obtain the MOF-FF potential.
In the original MOF-FF parameterizations, non-periodic density-functional-theory (DFT) calculations were carried out for the individual building blocks and their connections to obtain the required reference data. This was done to provide at least transferability when exchanging individual building blocks with other ones that show the same connecting chemistry. But since the aim of this work is not to provide transferable force fields to be used in combination with the original MOF-FF, periodic DFT calculations were carried out using VASP [50]. The actual fit for the force field is carried out by a code called FFGen [51] that has been used to parameterize MOF-FF for Zeolitic Imidazolate Frameworks. This has been performed in cooperation with the Schmid group, that developed FFGen and MOF-FF. The general work-flow for a parameterization of this type of force-field is outlined in figure 3.4.

The DFT calculation directly provides the geometry and the electrostatic potential. In addition the force constant matrix is calculated from a set of converged single point DFT calculations. Due to the significant computa-

tional cost, the phonon calculations are only performed at Γ point. The harmonic nature of this reference data implies that the anharmonicities included in a non-fixed form, as in the Morse-potential terms have to be provided externally. The required dissociation energies are based on tabulated values originating from experimental data. Parameters for the van der Waals interactions are the same in the MM3 [49] force field.
Atomic charges are obtained from the electrostatic potential using the REPEAT (Repeating Electrostatic Potential Extracted ATomic) [52] method. Here the potential $\phi_q$ of a system is given by a set of $N_q$ point charges $q_j$.

$$\phi_q(\mathbf{r}) = \sum_j \frac{q_j}{|\mathbf{r}_q - \mathbf{r}_j|} \tag{3.46}$$

With $\mathbf{r}_q$ being the point of the electrostatic potential and $\mathbf{r}_j$ the position of the point charge. The objective is now to minimize the differences between the DFT obtained potential $\phi_{QM}$ that is provided as a set of values distributed on a grid and the point charges at atom positions. The function $F$ to be minimized in REPEAT is given by: [52]

$$\begin{aligned} F(q_j, \delta_\phi) = &\sum_{grid} (\phi_{QM}(\mathbf{r}_{grid}) - (\phi_q(\mathbf{r}_{grid}) + \delta_\phi))^2 + \\ &\lambda(\sum_j q_i - q_{tot}) + \sum_j w_j \left( e_j^0 + \chi_j q_j + \frac{1}{2} J_j^{00} q_j^2 \right) \end{aligned} \tag{3.47}$$

Here the first term contains an additional parameter $\delta_\phi$. This is necessary due to the periodicity of the atomic charges where equation (3.46) has to be expanded based on an Ewald summation procedure. The second term conserves the total charge of the system in the form of a Lagrange multiplier. The third term serves to avoid unphysical charges for atoms with few valid fitting grid points in their proximity. It is included with an additional set of Lagrange multipliers $w_j$ and with parameters $\chi_j$ and $J_j^{00}$, which represent the electronegativity and the self-Coulomb interaction.
All the parameters from the formulations outlined in section 3.4.1 now have to be fitted to the aforementioned reference data. For the MOFs of interest this amounts to a total of about 50-200 parameters that have to be determined based on all the geometrical configurations as well as the entire force constant matrix. For this, a proper objective function has to be defined. This function essentially consists out of a sum of mean-square deviations formed from all

the reference data.

$$Z_{MOF-FF} = Z_{str} + Z_{bnd} + Z_{oop} + Z_{tor} + Z_{FC} \tag{3.48}$$

Here $Z_{str}$, $Z_{bnd}$, $Z_{oop}$, $Z_{tor}$ and $Z_{FC}$ represent the sum of the mean-square deviations of the bond-stretches, in-plane bending, out-of-plane bending, torsions and the force constants.

$$Z_x = \frac{w_x}{M_x} \sum_n \omega_n (x_n - x_n^{ref})^2 \tag{3.49}$$

This is summed over all occurrences $n$ for each interaction type $x$. Individual weights $w_x$ are given for all of these contributions. These weights are necessary, because the objective function sums over distances, angles and forces without regard to using a uniform unit. Therefore, the weights have to be arbitrarily chosen in order to not disregard important contributions from the reference. Additionally each redundant internal coordinate allows a weight $\omega_n$ depending on the atomtypes. $M_x$ is a weight normalization defined as $M_x = \sum_n \omega_x$.
Minimizing the objective function (3.48) is not straightforward, as it is inherently a function with a large number of local minima and/or discontinuities. Many conventional fitting procedures will fail to find the global minimum. An algorithm had to be chosen that makes no prejudicial assumptions about the landscape of the function. The applied fitting procedure is a Covariance Matrix Adaptation Evolution Strategy (CMA-ES) [53]. This algorithm has been used successfully for the parameterization of force fields for MOFs [51,54]. It accomplishes the minimization of an objective function by adapting the covariance of the variables based on evolution paths of previous attempts. The evaluation of the objective function is executed in batches of a predefined size that form the generation necessary to procure the evolution paths. Initially, the algorithm roughly estimates the variables by a distribution around a guess value. The width of this distribution, the step-size $\sigma$, has to be specified in advance and will be procedurally reduced the closer the fitted parameters approach convergence. This distribution width is the same for all variables and care has to be taken that it is applicable to all parameters occurring in the objective function in order to ensure that variations of all of them carry significant enough impact. It has to be large enough, in combination with a sufficient population size, to provide a good coverage of the function's landscape in a single generation, and small enough to

not exceed the physically realistic boundaries with a majority of evaluations. These choices determine if and how fast the global optimum can be found. In general convergence of this approach is significantly slower than conventional minimization algorithms like conjugate gradient, but faster than commonly used genetic algorithms commonly applied to fit classical force fields [51].

# 4 Computational Details

This section serves to introduce the individual procedures applied to obtain the thermal conductivity by providing the workflow used in MD simulations. In addition to this, the parameterized force-fields, including their process of parameterization, are discussed in detail. For both MOF-FF, and the force fields obtained by FF-gen validation will be provided, by comparing the vibrational properties to DFT data. The computational details for obtaining the ab-initio reference data that were provided by Tomas Kamencek are outlined in appendix A. References for the software utilized will be provided and the chosen settings, as well as convergence of the simulations, will be discussed.

## 4.1 Parameterized Force Fields

This section will cover the details of the parameterization process and the validation of the obtained force fields based on reference data. Please note that the numerical values for the obtained parameters are attached in appendix B.

### 4.1.1 IRMOF-1 (Mg)

The parameterization of IRMOF-1 with magnesium was carried out inspired by the base MOF-FF for IRMOF-1 with zinc. DFT calculations provided the reference data, and were carried out using the Vienna Ab-initio Software Package (VASP) by Tomas Kamencek with the simulation parameters given in appendix A. The bond-stretches were mostly given by the quartic MM3 potential terms with fixed anharmonicity (see equation 3.36). Notable exceptions were the Mg-O bonds that were described by a Morse potential (given in equation 3.37). The necessary dissociation energy is based on experimental data [55], measured with spectroscopic methods for MgO at room temperature. It amounts to 85 kcal/mol. All the angles were considered with the mm3 definition based on a polynomial of sixth order (equation 3.38). Additional stretch-stretch and stretch-bending terms were included for certain bond-bond and bond-angle interactions. The reason why not all cross-terms were included, is that the energy minima in those contributions are frequently ill defined and require more manual intervention during the parameterization process. If one is not careful with the cross-term limits, it

is possible that the structure will be unstable during the actual MD simulations. Therefore, only those terms have been included that lead to a significant improvement in vibrational properties. These are the ones including carbon-carbon, carbon-hydrogen and magnesium-oxygen interactions. The equilibrium configurations of most torsions in IRMOF-1 occur are planar. In the organic part and the linker-node connections the dihedrals can be described by a second order Fourier term that has minima at 0°and 180°. This angle has been provided as initial data for the fit to reduce the total amount of fitted parameters. Proper torsions inside the metal oxide were not found to have any significant impact on geometrical and vibrational properties and have been neglected. The other included interactions satisfactorily describe the motions in the inorganic components. Improper torsions (out-of-plane bending) have been considered as given in equation 3.41 by a harmonic potential with a reference angle of 0°. The necessary charges were calculated using the REPEAT [52] method based on the electrostatic potential obtained by periodic DFT calculations (carried out by Tomas Kamencek using VASP) and are given in table 4.1 for the parameterized IRMOFs. The meaning of the indices used in the table is displayed in figure 4.1. The atomic charges in the inorganic node for both IRMOF-1 and IRMOF-130 are similar despite the very different linkers. With the previously given definition of the force-

Table 4.1: Atomic charges of IRMOF-1 (Mg) and IRMOF-130(Mg). Values are given in elementary charges.

| **System** | **Mg** | $\mathbf{O_{cen}}$ | $\mathbf{O_{out}}$ | $\mathbf{C_{C1O2}}$ | $\mathbf{C_{C3}}$ | $\mathbf{C_{C2H1}}$ | **H** |
|---|---|---|---|---|---|---|---|
| IRMOF-1 (Mg) | 1.543 | -1.822 | -0.704 | 0.601 | 0.148 | -0.188 | 0.155 |
| IRMOF-130 (Mg) | 1.480 | -1.828 | -0.644 | 0.606 | | | |

field for this system the parameterization procedure has been run in multiple stages. During this process several different configurations of weights have been investigated in order to obtain the best possible fit. The FFgen fit was converged after 3000 generations with a population size of 32. Figure 4.2 visualizes the comparison between fitted and DFT-obtained geometries and vibrational frequencies. It can be seen that the agreement for geometrical parameters is excellent and only shows negligible differences. The root mean square error for all of these parameters is below 0.01 Å or 0.01°. The vibrational frequencies show a larger error – a 7% average deviation from

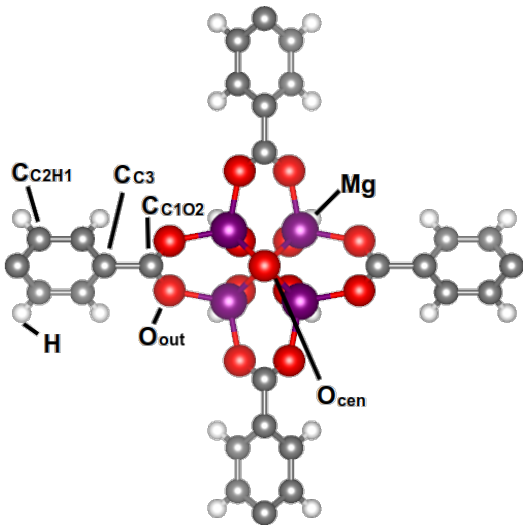


Figure 4.1: IRMOF-1 node and linkers with naming conventions of the atoms used for the unique atoms.

the reference values, but even there agreement is significantly better than in commonly used force fields for organic molecules [56]. It has to be noted that the relative error increases to 20% if one only looks at the first 200 $cm^{-1}$. Even though here the absolute error is significantly smaller than for the higher frequency modes with deviations of up to 10 $cm^{-1}$.

The frequencies of the normal modes are not the only quantities that are of importance to properly describe the interatomic forces for a system in motion. It is also important, that the vibrations for the different models match. In order to check this, the eigenvectors obtained from the diagonalization of the dynamical matrix in equation 3.17 have to be similar. The overlap between those vector can simply be obtained by comparing the sum over the dot products for each mode. But many modes are degenerate, with the same vibration occurring at the same frequency but in different directions. Aside of this, sometimes modes of similar energy occur in a slightly different ordering. Both of these facts make it helpful to assign the modes, that agree best for the optimized and reference structure based on their atomic displacements. For this, all dot products of all combinations of optical modes at $\Gamma$ point have been evaluated and subsequently sorted by minimizing a cost function

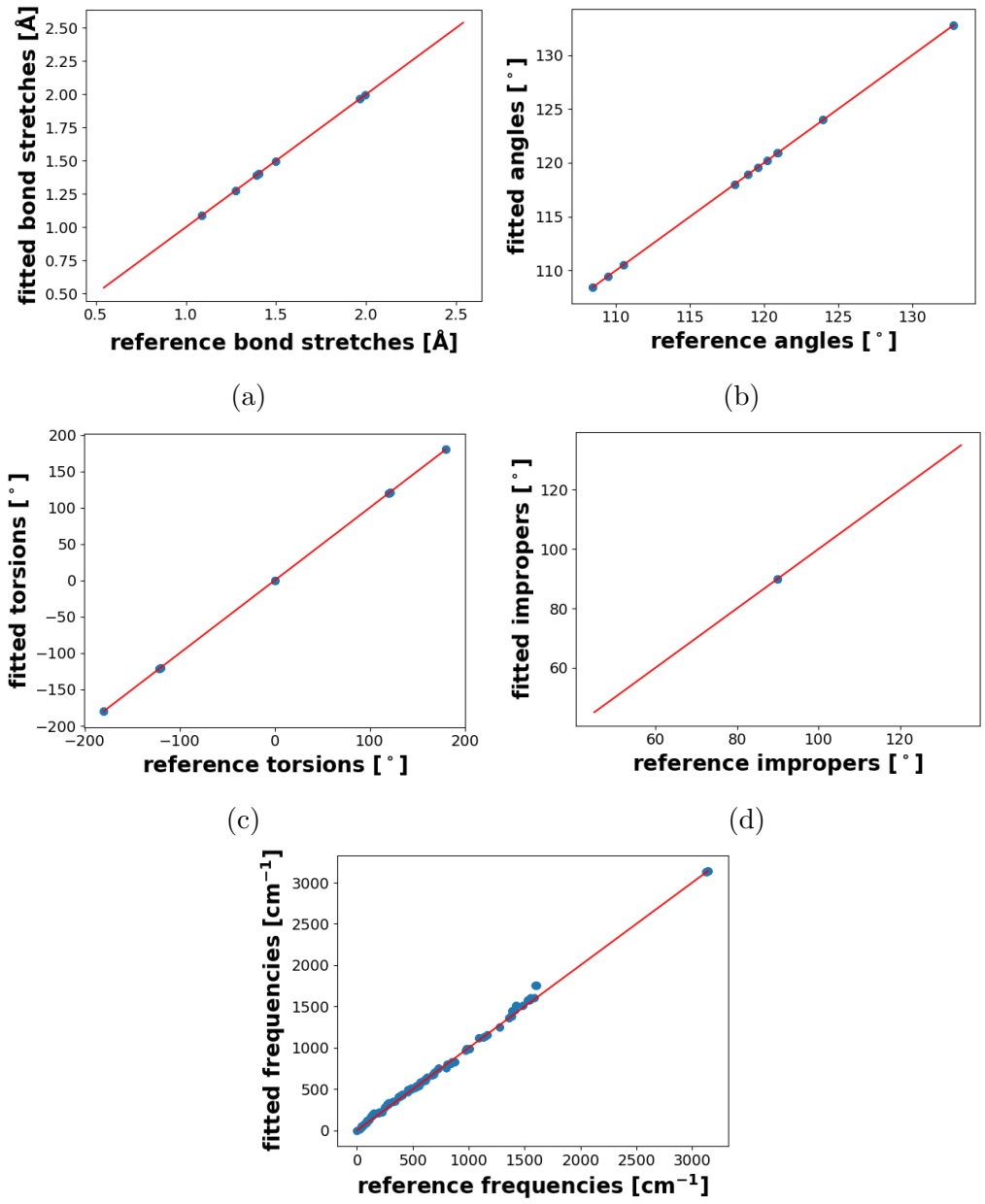


Figure 4.2: Comparison of fitted and reference bond lengths (a), angles (b), proper torsion angles (c), improper torsion angles (d) and vibrational frequencies (e) for IRMOF-1(Mg). The red line serves as a reference for optimal agreement.

$Z$ utilizing the Hungarian method for the assignment problem [57].

$$Z = \sum_i \sum_j C_{ij} X_{ij} \tag{4.1}$$

Here $C_{ij}$ are the eigenvector overlaps for the modes $i$ and $j$ while $X_{ij}$ is a logical assignment matrix, that has to be evaluated in the minimization process. Only one element of $X$ per row and column is allowed to be true, all others are false. This makes it possible to compare the overlap of eigenvectors between the same modes in the fitted force-field and the DFT reference. For IRMOF-1 (Mg) this is visualized as a histogram in figure 4.3. The root mean square error of the frequencies of matching modes amounts to 11 $cm^{-1}$ for the entire frequency range and 2.7 $cm^{-1}$ for frequencies up to 330 $cm^{-1}$. In the figure one can see, that the overlap is at least 0.4 for all modes while most range around 0.7. When considering only low frequency modes, the situation does not change significantly.

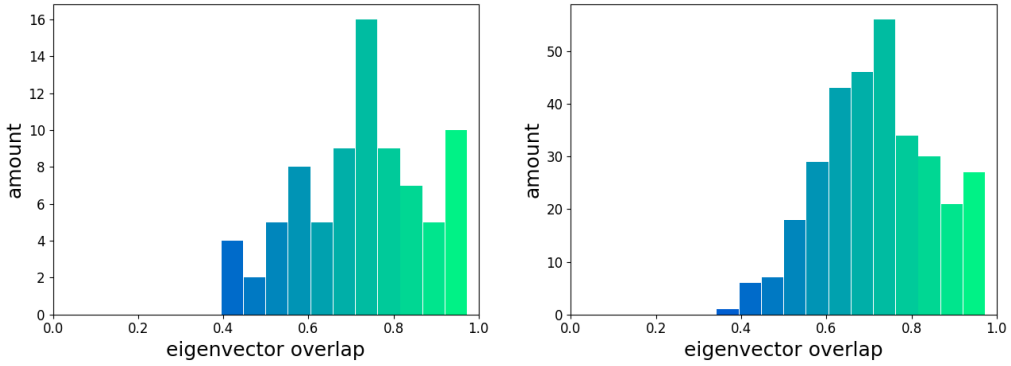


(a) (b)

Figure 4.3: Eigenvector overlap of the normal modes at Γ point for the fitted force field and the DFT reference in IRMOF-1 (Mg) for low frequency modes of up to 330 $cm^{-1}$ (a) and for the entire frequency range (b).

### 4.1.2 IRMOF-130 (Mg)

IRMOF-130, a typical $ZnO_4$ IRMOF with oxalic acid as its linker, is a hypothetical MOF that is of interest mostly due to its simplicity. The parameterization followed the same procedure as for the IRMOF-1 with one noteworthy difference. There were some additional torsional cross-terms included

to give a better description of the oxygen-carbon-carbon-oxygen interaction connecting the nodes. Poor vibrational properties were obtained with the conventional MOF-FF definition. The additional term serves to include an interaction between the outer bond stretches with the torsion itself and is called an end-bond-torsion term. It has been utilized in other force-fields for describing organic molecules, like the COMPASS force-field [56].

$$\begin{aligned} E_{ebt} = (r_{ij} - r_1)\left[A_1\cos(\phi) + A_2\cos(2\phi) + A_3\cos(3\phi)\right] + \\ (r_{kl} - r_3)\left[B_1\cos(\phi) + B_2\cos(2\phi) + B_3\cos(3\phi)\right] \end{aligned} \tag{4.2}$$

Here $r_{ij}$ and $r_{kl}$ are the bond lengths between the non-bonded atoms of the torsion, $r_1$ and $r_3$ are their reference values, $A_x$ and $B_x$ are force constants and $\phi$ is the torsional angle. The atomic charges can be seen in table 4.1. The fit is then performed based on data obtained with VASP and was converged after 10000 generations with a population size of 32. The comparisons of the geometrical and vibrational parameters can be seen in figure 4.4. Just as for IRMOF-1 the geometry fits exceptionally well compared to the reference. The vibrational frequencies show an average deviation of 12% which is still in an acceptable range but worse than the IRMOF-1 (Mg). Like previously, agreement is poorer in the lower frequency regime going up to a relative error of 30%, which is significantly worse than that of other MOFs investigated in this work. This is something that should be kept in mind for all further analysis, as the low lying modes are essential for many physical observables.

Like in the previous section, the eigenvector overlap of the normal modes at $\Gamma$ has been analyzed and visualized in figure 4.5. Here, the overlap is at least 0.5 for all modes both for low and high frequencies. There appears to be a larger amount of high energy modes with excellent agreement, but most of them range around 0.7. This still seems to be significantly better than in IRMOF-1 (Mg) which is also reflected by the root mean square error of matching modes with 6 $cm^{-1}$ for the full frequency range and 2 $cm^{-1}$ for up to 330 $cm^{-1}$ modes. Even though the side-by-side comparison of the frequencies themselves appeared to be relatively poor, the actual vibrations, after assigning the best fitting eigenvectors, show a reasonable agreement.

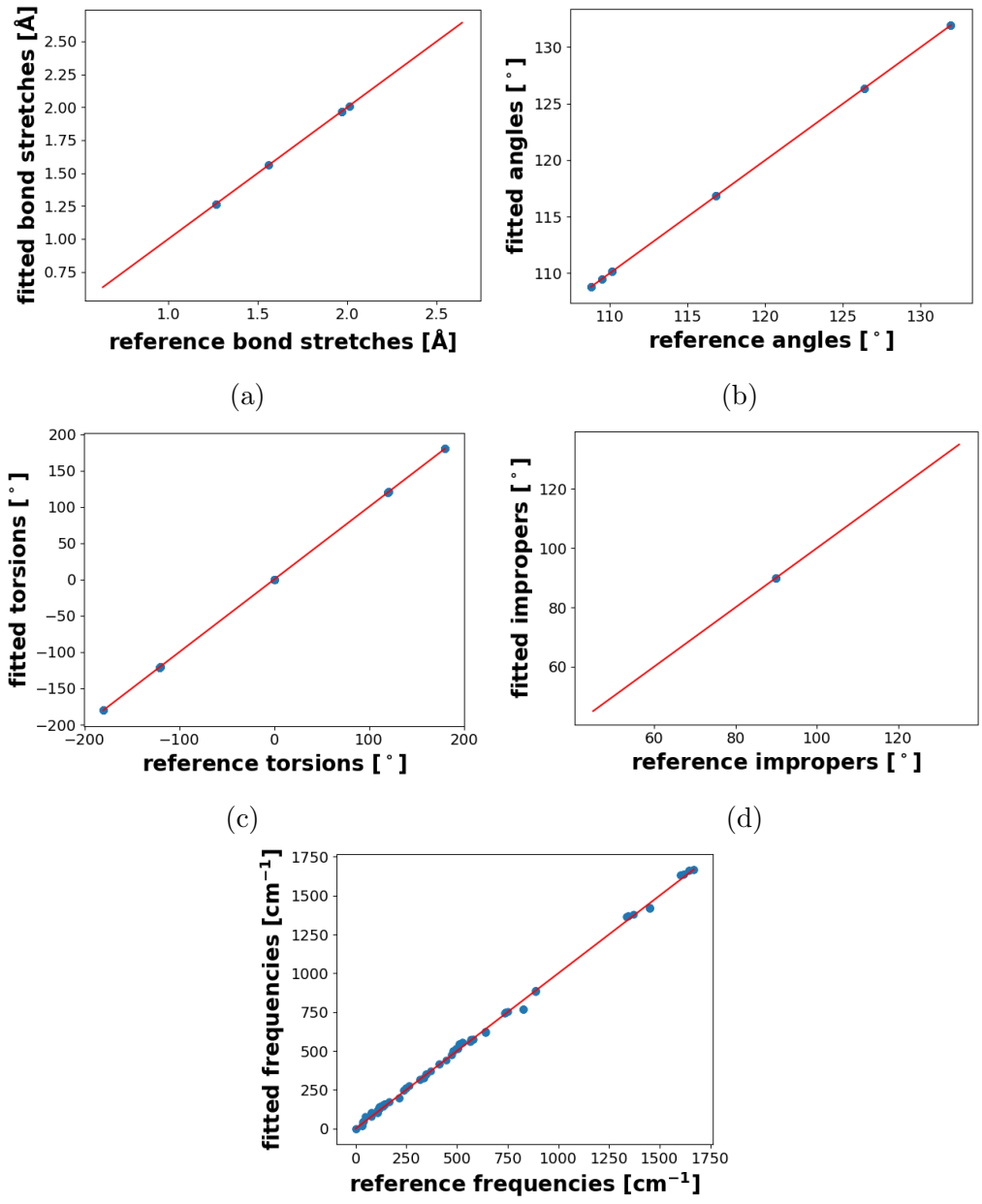


Figure 4.4: Comparison of fitted and reference bond lengths (a), angles (b), proper torsion angles (c), improper torsion angles (d) and vibrational frequencies (e) for IRMOF-130(Mg). The red line serves as a reference for optimal agreement.

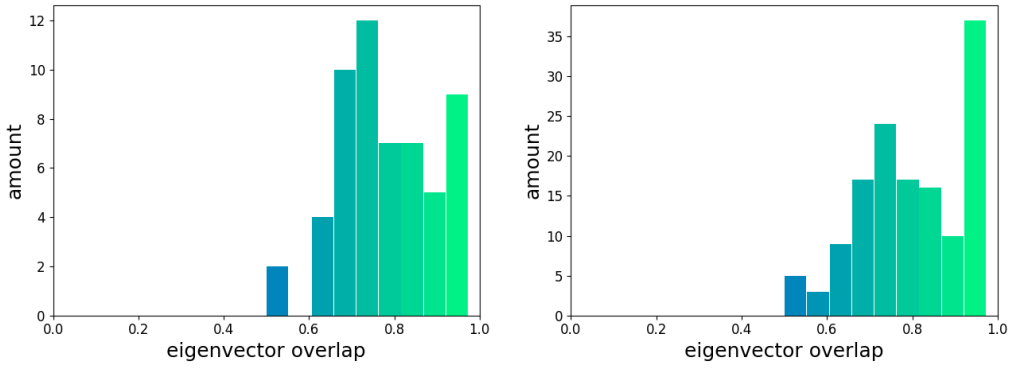


(a) (b)

Figure 4.5: Eigenvector overlap of the normal modes at the Γ point for the fitted force field and the DFT reference in IRMOF-130 (Mg) for low frequency modes of up to 330 $cm^{-1}$ (a) and for the entire frequency range (b).

### 4.1.3 MOF-74

As a completely different MOF, MOF-74 with zinc as a metal has also been parameterized as a force field based on periodic DFT calculations. The procedure employed, was the same as for the previously considered MOFs. The atomic charges were evaluated from the electrostatic potential with the REPEAT method and can be seen in table 4.2. Figure 4.6 shows a unit cell of MOF-74 and clarifies the given atom names. The difference between $O_{co2,1}$ and $O_{co2,2}$ is, that the first directly connects to only one zinc atom while the latter connects to two. Note that there are more atoms displayed than contained in the primitive cell in order to clarify the periodic boundaries.

Table 4.2: Atomic charges of MOF-74 (Zn). Values are given in elementary charges

| **Zn** | $\mathbf{O_{co2,1}}$ | $\mathbf{O_{co2,2}}$ | $\mathbf{O_{eth}}$ | $\mathbf{C_{C2O1}}$ | $\mathbf{C_{C1O2}}$ | $\mathbf{C_{C2H1}}$ | $\mathbf{C_{C3}}$ | **H** |
|---|---|---|---|---|---|---|---|---|
| 1.231 | -0.732 | -0.767 | -0.675 | 0.382 | 0.853 | -0.188 | -0.287 | 0.183 |

During parameterization, no torsional cross-terms were included and only a selected batch of str-str and str-bnd terms were considered. Details of which

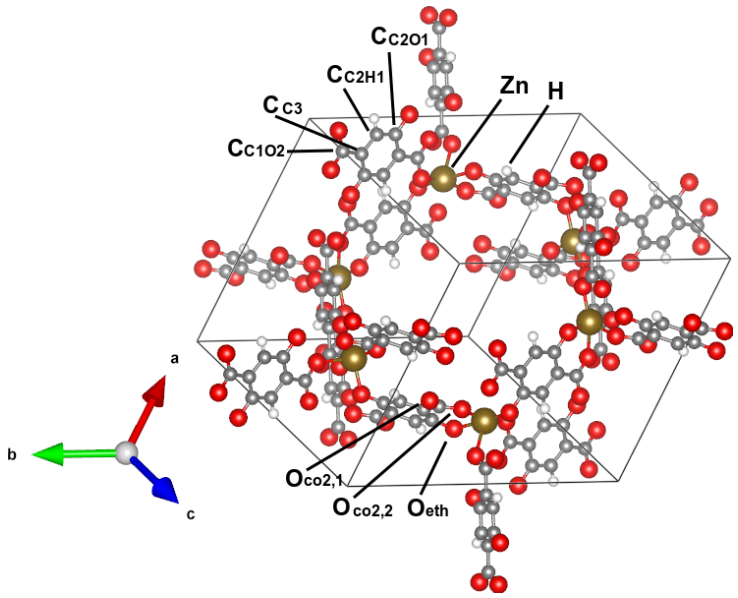


Figure 4.6: Atom labeling of MOF-74 (Zn) used in this work

terms were neglected can be found in the full overview of the force field in section B.3. Many proper torsions occurring in the inorganic building blocks have been set to zero due to the high complexity of the system and the much more rigid nature of MOF-74. This nature leads to torsional terms, especially in the inorganic helical "node-chain", being significantly less important. At this point, it should be noted that there are more than three times as many dihedrals and angles in MOF-74 than in IRMOF-1, even though the number of atoms is smaller by almost a factor of two. This led to a very large number of degrees of freedom, which resulted in some significant difficulties when performing the fits. It is possible that some of the parameters become unphysical after the fit leading to a destabilization of the structure during an MD simulation. This required a significant amount of manual intervention and defining of hard limits for many fitting parameters. This imposes a restriction on the degrees of freedom and might be responsible for the slightly worse agreement of vibrational frequencies.

The Zn-O bond have also been described by an anharmonic Morse potential with a bond dissociation energy of 50 kcal/mol. This was also the value used for the zinc based systems in MOF-FF. The FFgen fit was converged after 60000 generations of the CMA-ES algorithm with a population

size of 32. The comparisons of the geometrical and vibrational properties are depicted in figure 4.7. Like in previous fits, the geometrical parameters fit almost perfectly to the reference structure with a very small error of less than 0.01 Å or 0.01°. The frequencies up to 100 $cm^{-1}$ show an excellent agreement with an average deviation of less than 5 %. In the range from 100 to 500 $cm^{-1}$ the frequencies are overestimated significantly leading to a deviation of up to 17 %. In the entire frequency range the error amounts to 8 %. But since the most important contributions to the thermal conductivity are in the very low frequency regime, the larger error should be tolerable.

The eigenvector overlap has been calculated like in section 4.1.1 and is shown in figure 4.8. The agreement of the vibrations appears to be significantly poorer than what has been obtained for the other MOFs, with some modes only showing an overlap of 0.35. Especially the modes from 100 to 500 $cm^{-1}$ seem to be responsible for this disagreement. This also is shown by the deviation in this frequency region in figure 4.7. This is also reflected by the root mean square error of the matching frequencies, which amounts to 3.0 THz for the entire frequency range and 3.7 THz for up to 330 THz modes.

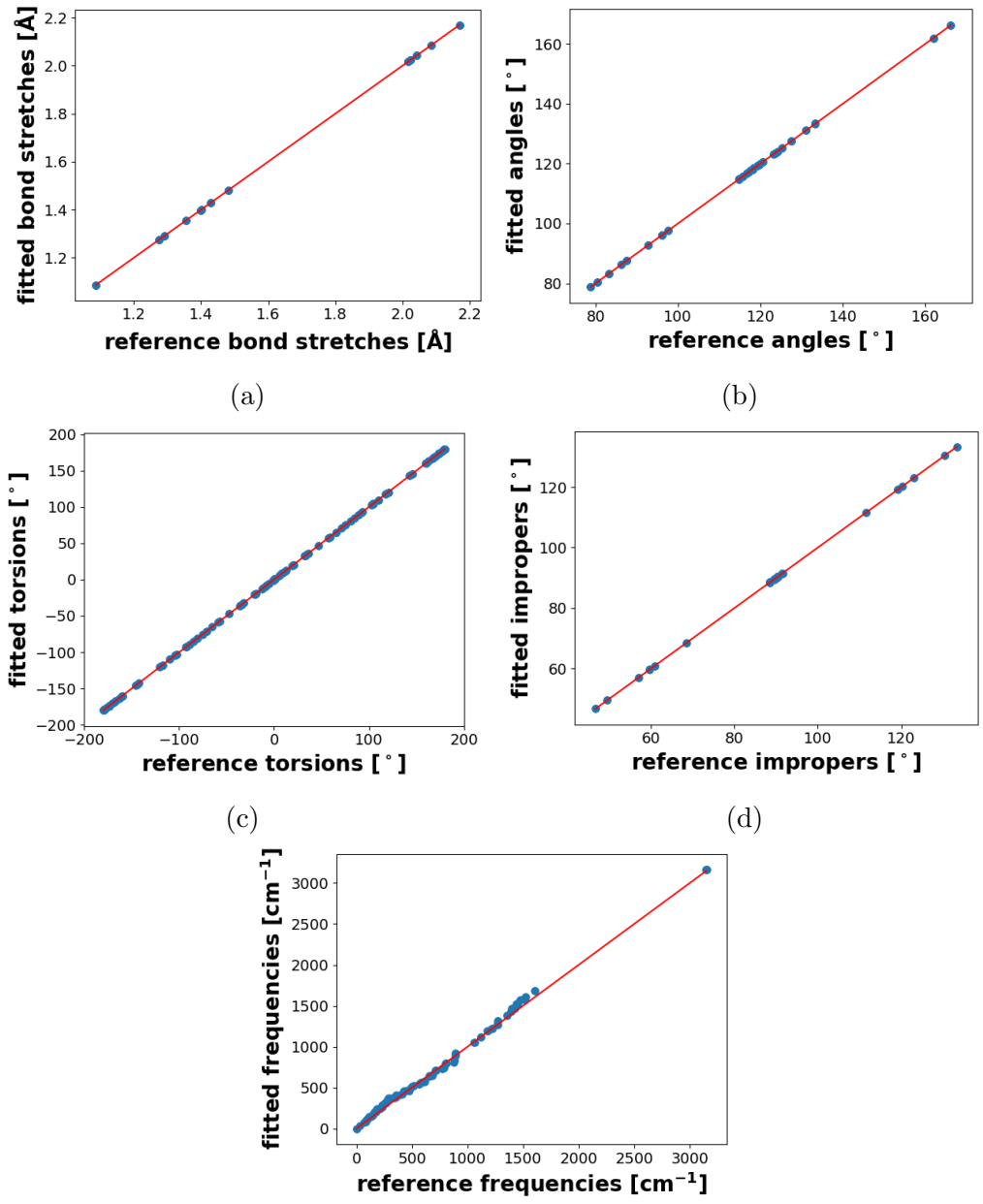


Figure 4.7: Comparison of fitted and reference bond lengths (a), angles (b), proper torsion angles (c), improper torsion angles (d) and vibrational frequencies (e) for MOF-74 (Zn). The red line serves as a reference for optimal agreement.

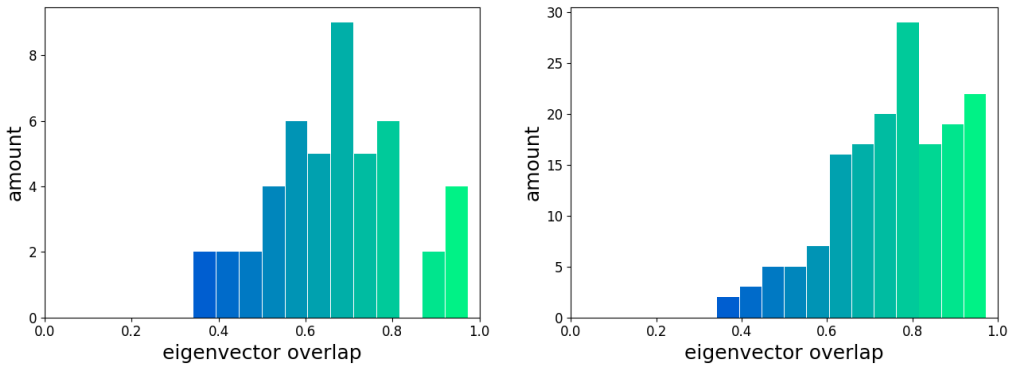


(a) (b)

Figure 4.8: Eigenvector overlap of the normal modes at Γ point for the fitted force field and the DFT reference in MOF-74 (Zn) for low frequency modes of up to 330 $cm^{-1}$ (a) and for the entire frequency range (b).

## 4.2 Lattice Dynamics

Lattice dynamics (LD) allows more sophisticated analysis of thermal properties in materials dominated by phonon transport. In literature, these calculations are typically carried out using first-principle methods, like DFT. This often requires relatively large supercells even for simple systems to converge properly. For highly complex chemical compounds carrying out LD simulations is next to impossible with current technology using density functional theory. But LD is not restricted to density-functional based methods, as the only physical quantity needed are interaction forces (see section 3.2) between the atoms, which can also be approximated by simpler methods. Therefore, phonon properties and the thermal conductivity can be obtained based on zero Kelvin simulations utilizing classical force-fields (FFs). The theoretical details used to obtain these data have been discussed in depth in section 3.2. This section will cover the simulation details to calculate phonons, with some comparisons of what has been obtained with methods of higher level of theory. With that, a justification for analyzing force-field obtained phonon properties should be given. IRMOF-1 (Zn) will be used as an example but calculations for all systems are analogous. The software used to carry out the calculations was phonopy [58] up to Force-Constants of the second order and phono3py [28] for calculations including three-body interactions and the evaluation of the Boltzmann transport equation.

First it was necessary to relax the geometry of the investigated systems. The primitive unit-cell was minimized with help of a conjugate gradient algorithm in three steps. First, only the internal positions were relaxed to the maximum achievable precision for the force-field. In the second step, the cell parameters anisotropically in addition to the atomic positions. After this the internal coordinates were relaxed again with fixed cell parameters. The minimum forces that are possible to obtain appeared to depend on the system. Those with specifically parameterized force fields based on periodic reference data achieved a higher precision compared to those obtained by non-periodic clusters. In case of IRMOF-1 the maximum remaining force amounted to $10^{-4}\mathrm{kJ}/(\mathrm{mol}\cdot\mathrm{\AA})$. It was possible to attain a lower value for the maximum force for all other systems. The primitive unit cell of IRMOF-1 consists of 106 atoms. It contains two complete inorganic nodes, and is depicted in figure 4.9. The crystal shows face-centered cubic (fcc) symmetry and the corresponding first Brillouin zone is depicted in figure 5.1.

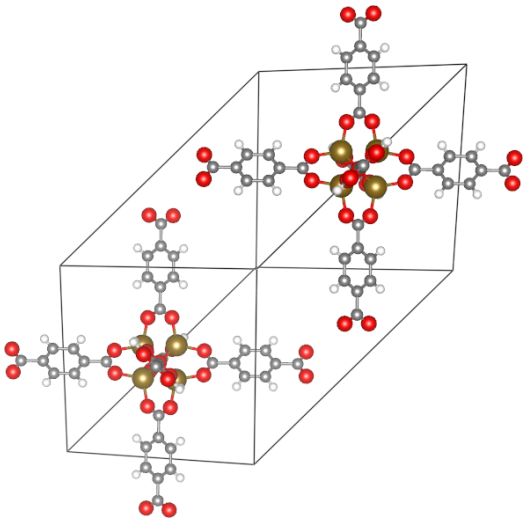

Figure 4.9: Primitive unit cell of IRMOF-1 forming an FCC lattice. The organic linkers have been expanded beyond the box boundary for clarification.

The phonon calculations were then carried out using the supercell approach. A 3x3x3 primitive supercell of IRMOF-1 was required to obtain convergence. This was reached once an increase in supercell size did not lead to any visible changes in the phonon band structure. In order to validate

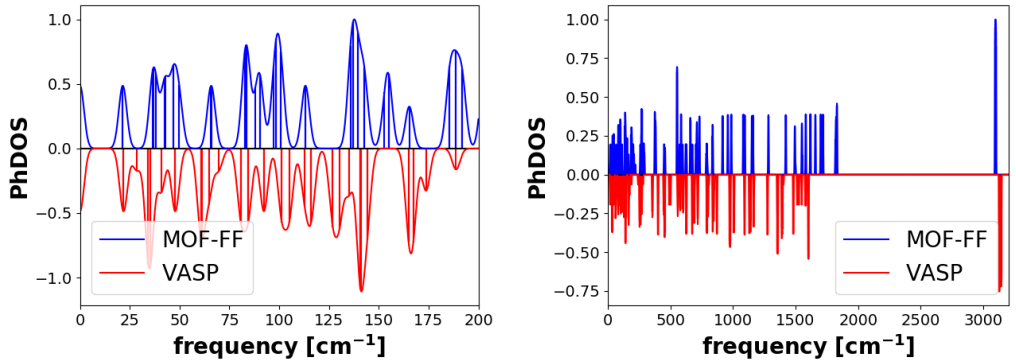


(a) low energy modes

(b) all modes

Figure 4.10: Comparison of density of states and vibrational frequencies at Γ point in IRMOF-1(Zn) between VASP and MOF-FF phonon calculations

the vibrational properties, figure 4.10 visualizes a comparison of the density of states at Γ point between DFT (VASP) and FF data. One can observe reasonable agreement between the curves, especially in the low frequency regime. Some of the high energy modes are significantly higher for the force field. These are mostly localized vibrations in the organic linker that show next to no contribution towards most physical properties, including thermal transport. In order to analyze the impact of individual phonon modes we also have to take phonons outside of the Γ point into account. For this obtaining DFT reference data with the supercell approach is not possible any more due to the size of these systems. Therefore, we compared the phonon dispersion bands with density-functional tight binding (DFTB) based data. These calculations have also been performed by Tomas Kamencek and some simulation details are outlined in appendix A. This is shown for the lowest 6 THz in figure 4.11. Here, it can be seen that the acoustic modes are in excellent agreement to each other. A lot of the optical modes can be found at different frequencies, but similar modes can typically found in close proximity. Also note that the Γ frequencies for DFTB also deviate from those obtained by DFT. This explains the different lowest lying optical mode in the band structure that does not appear in the DFT data in figure 4.10.

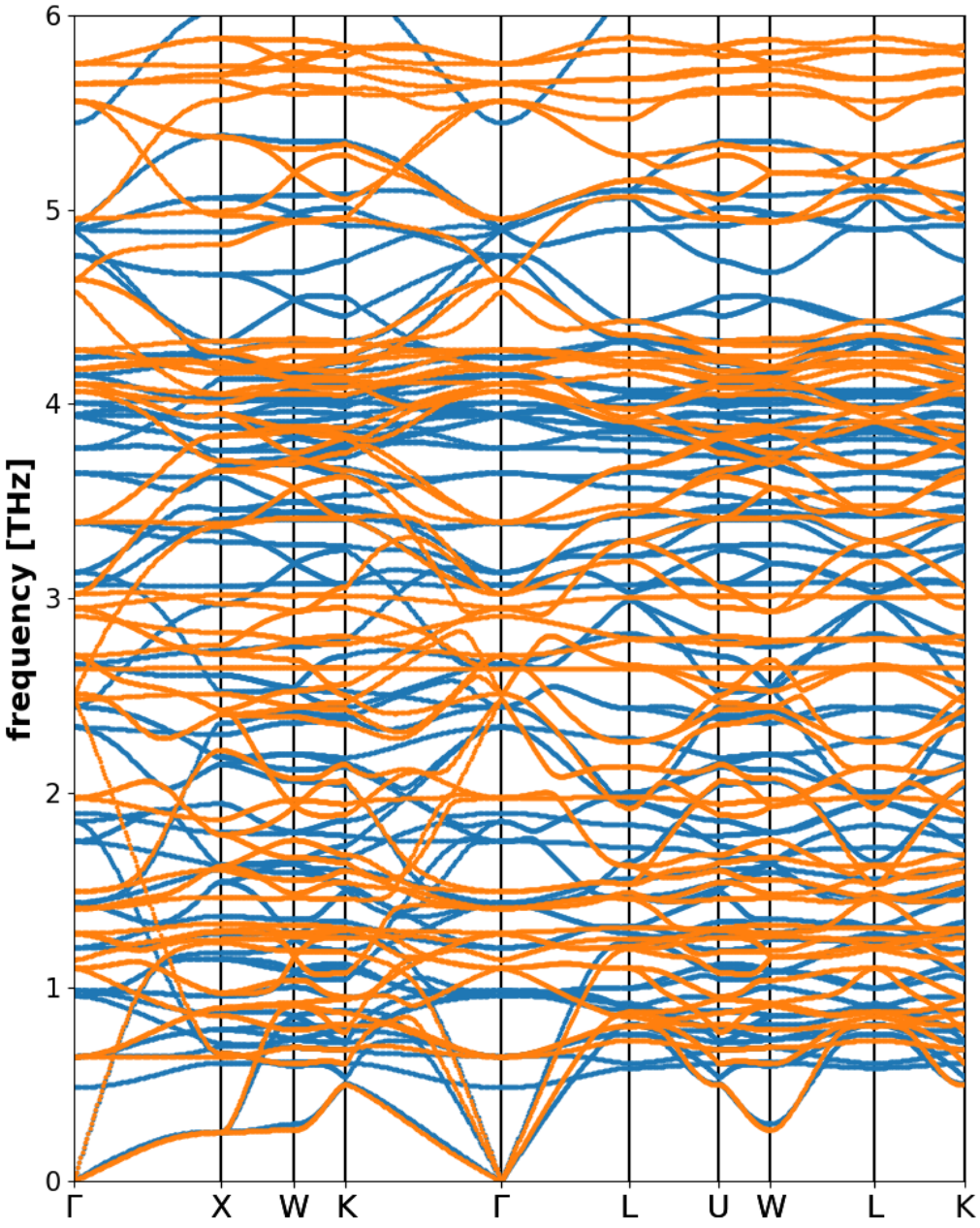


Figure 4.11: Comparison of phonon bands of IRMOF-1 (Zn) between MOF-FF (orange) and DFTB (blue) phonon calculations

## 4.3 Molecular Dynamics

For carrying out all the molecular dynamics simulations, the Large-scale Atomic/Molecular Massively Parallel Simulator (LAMMPS) [59] has been used. This section provides an overview of the general settings used for all further simulations and discusses some methodological issues when applying this method for MOFs.

All simulations have been carried out for time steps of 0.2 fs. Such small time scales are necessary to properly describe the interactions of hydrogen atoms in the organic building blocks. Commonly used guidelines for the choice of timestep in MD suggest that a higher timestep of about 1 fs should be sufficient to describe carbon-hydrogen stretches. This timestep has been tested, but was found to provide vastly incorrect results. For all runs, the Coulomb interactions have been calculated in real space for short-range and in k-space for long-range interactions. The cutoff separating real and reciprocal values was set to 12 Å. By applying a smoothening parameter beginning at 90% of the cutoff, it is ensured that the energy does not abruptly decay to zero. The same parameters have been used to define the van-der-Waals cutoff. Beyond the 12 Å, a particle-particle particle-mesh (pppm) solver [60] has been used to interpolate the charges from a mesh in reciprocal space. The precision of this approach is specified as the minimal allowed charge value of a point, which was set to $10^{-5}$ or lower. For all MD simulations, a standard velocity-Verlet integrator has been used.

In order to be certain that the MD simulations yield accurate results, it has to be verified that the simulation temperature is high enough to comply with the classical limit. The easiest criterion to verify this, is the heat capacity that should approach a converged value in the classical limit. Since the heat capacity is constant under these conditions, one has to use the temperature dependent values obtained from lattice dynamics. This is shown in figure 4.12a for IRMOF-1 (Zn). It can be seen that the heat capacity is not completely constant until several thousand Kelvin. The temperature range of interest is around 300 K where the heat capacity only reaches about 50% of its maximum value. This might seem very concerning, but typically the high temperature contributions arise from lighter atoms, like hydrogen in the case of IRMOF-1, that are of little relevance for heat transport. It has been observed previously [42] that proper thermal properties can be calculated for temperatures below the classical limit. It will also be shown later, when analyzing lattice dynamics results that mostly low frequency vibrations con-

tribute to the thermal conductivity, which are occupied already at very low temperatures. In order to visualize this, the heat capacity for IRMOF-1 has been calculated for many different cutoff frequencies. Then, for each of these calculations, the saturation temperature, where the heat capacity reaches 95 % of its maximum value for a certain cutoff, has been determined. These saturation temperatures are visualized in figure 4.12b. Again, the temperature range of interested is indicated with a shaded area. We see that the modes in the first 10 THz are already occupied when temperatures of 200 K are reached.

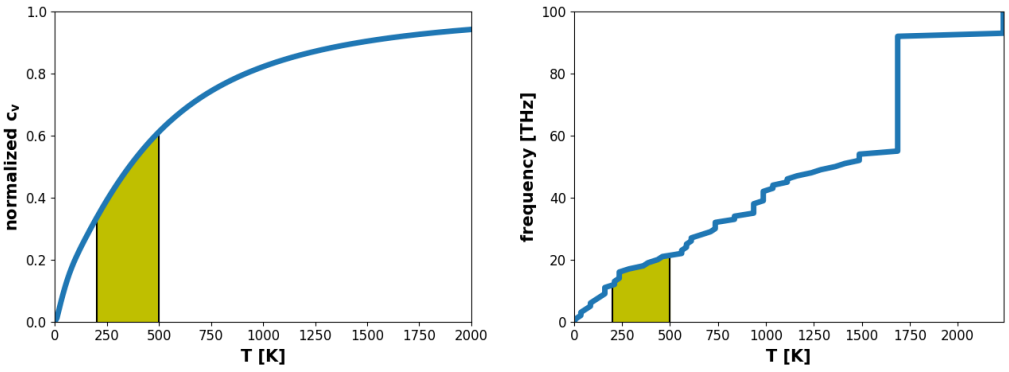


(a) (b)

Figure 4.12: (a) Temperature dependent heat capacity of IRMOF-1 on a 10x10x10 mesh. (b) cutoff frequencies and saturated temperatures where the heat capacity reaches 95% of its final value of IRMOF-1. The yellow area indicates the temperature range of interest.

In addition to making sure that the molecular dynamics simulations are valid, it is important to converge the individual simulations. Here the convergence criteria for each of them will be discussed. For simple thermalization in an NVE ensemble and the calculation of volumes in an NPT ensemble, the only criteria given are that the average temperature and pressure must approach a converged value, which should coincide with the previously specified target. This can happen quite fast – in a few ps – depending on the system. Using larger cells will lead to more stability and less noise in the observables, requiring less time to converge.
For the Green-Kubo simulations it is necessary to first get the system in a steady state at the equilibrium temperature and volume. Afterwards one

has to choose a sufficiently high correlation length for the autocorrelation function. The suitable value of this correlation length highly depends on the numerical value for the thermal conductivity. A high $\kappa$ will lead to a slower decay of the heat current requiring longer correlation lengths. The easiest way to check for convergence, especially for noisy heat-current autocorrelation functions (HCACF), is to observe if its integral (so, the thermal conductivity) reached saturation as can be seen in figure 4.13b for IRMOF-1. The HCACF itself can be very noisy for low thermal conductivity materials like MOFs. As an example, such a function is visualized in figure 4.13a. A common practice to improve results is to apply a noise filter by removing high frequency contributions from the Fourier transform of the HCACF [61]. But since Huang et al. [62] suggested that high frequency oscillations arise due to contributions of optical phonons, which cannot be neglected for MOFs, this approach has not been applied in this work. Another reason to refrain from this method is that only taking the low frequency limit of the Fourier transform assumes an exponential decay of the HCACF, which has been shown not to be the case in certain situations [19]. Instead, a simple average has been formed over a specified convergence region in the integral of the HCACF. This region is difficult to define, as noise can lead to artificial deviations from the converged value for longer correlation lengths [62]. Aside of the HCACF itself, the simulation time has to be sufficiently long in order to obtain an accurately statistical averaged HCACF. To check for this parameter the time evolution of the resulting thermal conductivity has been observed. This is shown in figure 4.14. When the thermal conductivity showed no significant changes for longer times anymore, the simulation was considered converged. This typically requires simulation times of 1 ns or more.

While finite size effects occurring with the Green-Kubo method are fairly insignificant, it is still important to observe them for MOFs. Previous investigations have shown that cells a few nm long are frequently sufficient to obtain proper thermal conductivity values without showing finite size effects [19, 47]. This is typically much shorter than the phonon mean free path in these materials. Also for MOFs previous publications have shown that only a small 2x2x2 conventional supercell for IRMOF-1, with lattice constants of 5.2 nm, is required to obtain converged results [22, 62]. In this work cells for IRMOF-1 up to 4x4x4 supercells have been calculated and no significant differences have been observed compared to 2x2x2 supercells.

In the case of the non-equilibrium molecular dynamics (NEMD) simulations reaching a steady state across the cell has to be ensured. A good indicator

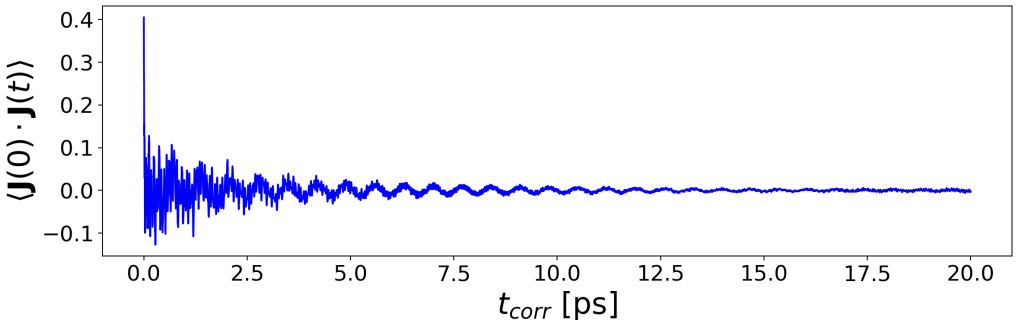


(a)

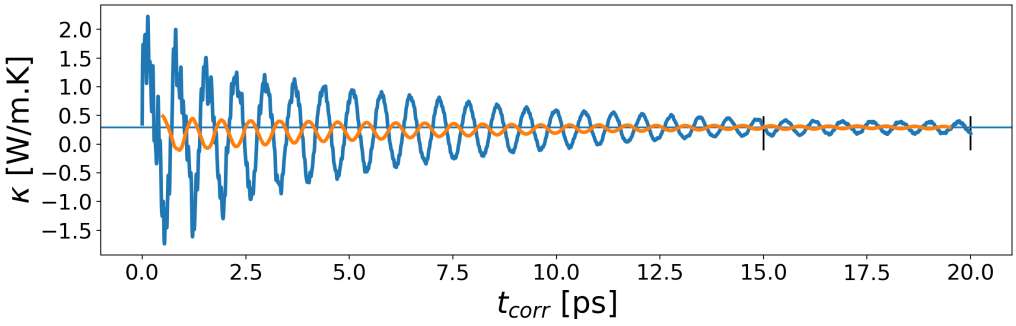


(b)

Figure 4.13: Heat-current autocorrelation function (a) and the thermal conductivity as a cumulative integral of the HCACF (b, blue) and a running average (b, orange) of a 2x2x2 IRMOF-1 supercell after 4 ns simulation time at 300 K.

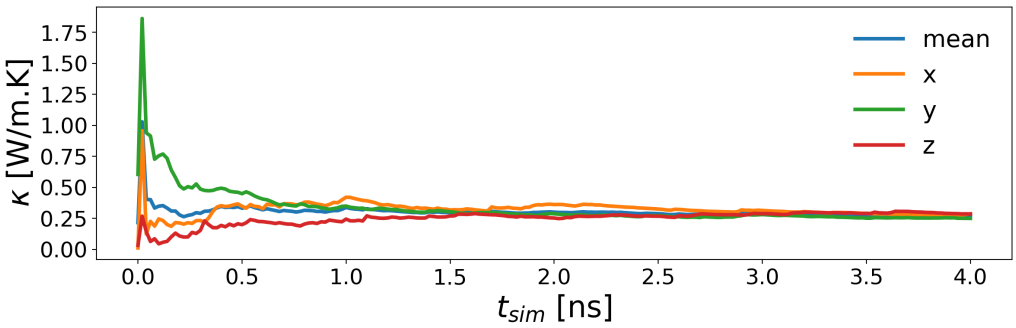


Figure 4.14: Time evolution of the thermal conductivity over the duration of a Green-Kubo simulation for a 2x2x2 supercell of IRMOF-1 at 300 K.

for this represents the heat flux injected and removed by the thermostats. The energy added and subtracted have to be equal as a condition for the steady state. At this point it should be noted, that if the used cell is too thin in cross-sectional directions, e.g. if one were to use a 8x1x1 cell instead of an 8x2x2, it is possible that the heat flux of both thermostats shows very large differences, even for long simulation times. This can be seen to a lesser extent in figure 4.15a where the heat fluxes of the thermostats are similar but not precisely the same after the molecular dynamics simulation ran for a long time. The difference of these heat fluxes is then considered as an error $\Delta J$ for the heat flux. When carrying out periodic NEMD simulations one will always obtain two temperature gradients in a single cell to either side of the thermostat. The difference in the temperature profile is also an indicator for reaching steady state and can also serve as an error $\Delta\nabla T$. A total error for the thermal conductivity using NEMD, as specified for results following in this thesis, arises then from Fourier's law:

$$\Delta\kappa = \frac{\Delta J}{\nabla T} + \frac{J\Delta\nabla T}{\nabla T^2} \tag{4.3}$$

The temperature profile and the heat fluxes of the thermostats are represented in figure 4.15 for the example of IRMOF-1. Steady state is reached faster the for larger cross-sections of the cell, but for most systems used, simulation times of 1 ns or more were required to achieve convergence. A larger crpss-section also reduces the error of the heat flux. In figure 4.15b one can see that there are large temperature drops close to the thermostat regions. They arise due to phonon scattering at the thermostat boundary [19]. The temperature gradient which will be used to calculate the thermal conductivity was obtained from a linear fit in the area sufficiently far away from these boundaries. The left limit was chosen from $2L_x/16$ to $6L_x/16$ and the right limit from $10L_x/16$ to $14L_x/16$. This allows a fitting across the linear regime even for the smallest cells used in this thesis. Longer simulation times aid to reduce the error of the temperature gradient.
Particularly serious for NEMD simulations are the finite size effects. To account for them, the infinite size extrapolation scheme as discussed in section 3.3.1 was used. The thermal conductivity was calculated for several different cell lengths and then fitted to the infinite size limit. Such a fit is visualized in figure 4.16 for 4x2x2, 6x2x2, 8x2x2 and 10x2x2 supercells. Care should be taken that the value is taken in the linear regime of the $1/\kappa$ to $1/l$ curve, as there can be deviations for very small cells. This did not appear to be a

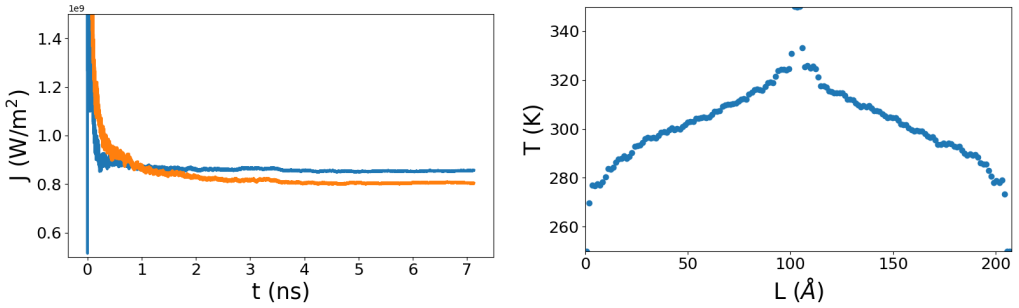


(a) (b)

Figure 4.15: Heat flux added and subtracted by the thermostats (a) and temperature profile averaged over time after the simulation reached steady state (b) for a NEMD simulation using a 8x2x2 supercell of IRMOF-1 over a time period of 7 ns at 300 K.

problem for the tested systems in this thesis, but it has been shown before that too small cell sizes can lead to non-linear behavior [63].

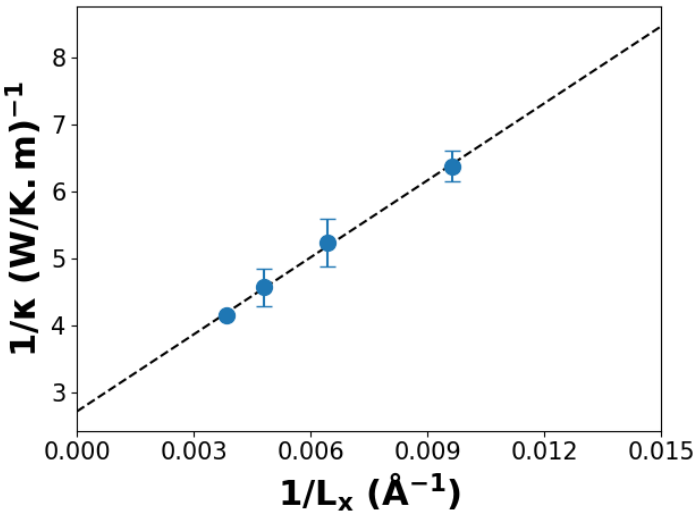


Figure 4.16: Extrapolation of the infinite size limit of NEMD simulations for the thermal conductivity of IRMOF-1 at 300 K. The cells used were 4x4x4, 6x2x2 and 8x2x2 with at least 1 ns of simulation times each.

# 5 Results and Discussion

This section serves to visualize and discuss the results for all systems obtained with lattice and molecular dynamics. Additional parameters used beyond what was described in section 4 will be included for each material. First, vibrational properties will be shown in order to provide a basis for further discussion. Then volumes and lattice parameters for the materials will be given and their thermal expansion will be discussed. Subsequently, the thermal conductivity values obtained from molecular dynamics will be shown and discussed. Finally, thermal conductivity results from lattice dynamics will be shown and a comparison between the various methods will be given.

## 5.1 Phonon band structures

Lattice dynamics calculations have been carried out using MOF-FF as a force calculator to analyze the thermal properties obtained with MD. In section 4.2 we covered the basics and gave a justification based on IRMOF-1 using available DFT and DFTB data. Here we will cover all the investigated systems to provide a basis for discussion in the following sections. The analysis of individual phonon modes is based on visually observing the vibrational motions that can be visualized by using the eigenvectors of the dynamical matrix.

At first the primitive cells of all systems had to be optimized and the resulting lattice parameters can be seen in table 5.1.

Table 5.1: Optimized lattice parameters for primitive cells of all systems investigated with lattice dynamics. All values are given in Å.

| **System** | **xx** | **yy** | **zz** | **xy** | **xz** | **yz** |
|---|---|---|---|---|---|---|
| IRMOF-1 (Zn) | 18.406 | 15.940 | 15.028 | 9.203 | 9.203 | 5.313 |
| IRMOF-1 (Mg) | 18.526 | 16.044 | 15.127 | 9.263 | 9.263 | 5.348 |
| IRMOF-10 (Zn) | 24.403 | 21.133 | 19.925 | 12.201 | 12.201 | 7.044 |
| IRMOF-130 (Mg) | 12.476 | 10.805 | 10.187 | 6.238 | 6.238 | 3.602 |
| MOF-508 | 11.002 | 11.002 | 14.115 | 0.000 | 0.000 | 0.000 |
| JAST-1 | 15.446 | 9.652 | 15.667 | 0.000 | 0.000 | 0.000 |
| MOF-74 | 15.250 | 13.478 | 6.414 | -7.136 | -7.136 | -11.853 |

### 5.1.1 IRMOFs

Here we will discuss differences among IRMOFs with different linkers or nodes that still maintain a FCC lattice. As a reference and to explain the labeling in the following band structures, figure 5.1 visualizes the first Brillouin zone for the face-centered cubic symmetry and the primitive unit cell of IRMOF-1. The other IRMOFs show the same type of cell, but with different linkers.
Figure 5.2 visualizes a comparison of the phonon dispersion bands up to 3 THz from IRMOF-1 and IRMOF-10 in order to analyze differences in linker length. The bands are based on force constants obtained with a 3x3x3 primitive supercell for both systems. It is immediately noticeable that for IRMOF-10 the acoustic modes occur at lower frequencies and that there are more lower lying optical modes. At such low energies, there are many vibrations similar for both systems, as the individual components move in relatively rigid units leading to their low frequencies. But those similar modes can be found at a lower frequency for IRMOF-10. Also more modes can be found in this region, because the bending and rotational motions of the phenyl rings in the biphenyl linker adds an additional degree of freedom. A clear difference are also the smaller slopes in the band structure for both the acoustic and optical modes. This, in turn, leads to a lower group velocities which lowers the thermal conductivity. But a direct comparison between different systems is difficult, as the cell is longer for IRMOF-10, leading to shorter reciprocal band paths, while the figures only visualize the reduced wave vectors along the high-symmetry lines.

Another possible variation is given by using different metals in the inorganic nodes. Figure 5.3 visualizes a comparison of the band structure for IRMOF-1 with magnesium and zinc. Phonons for the Mg-MOF were obtained using the parameterized force field discussed in section 4.1.1 for a 3x3x3 supercell. Here we can see that the acoustic modes for the magnesium MOF are of higher energies. Optical phonons can be found at lower or higher frequencies. When the mass of the metals is reduced, one would expect a higher frequency, as can be seen nicely for the acoustic modes. At the high symmetry points an increase of up to 0.3 THz can be seen, but in many regions of the Brillouin zone the differences are much smaller. In the low frequency region there is an error ranging from 0.1 to 0.3 THz due to the fitting process making it more difficult to make statements for the optical bands due to the small energy differences.

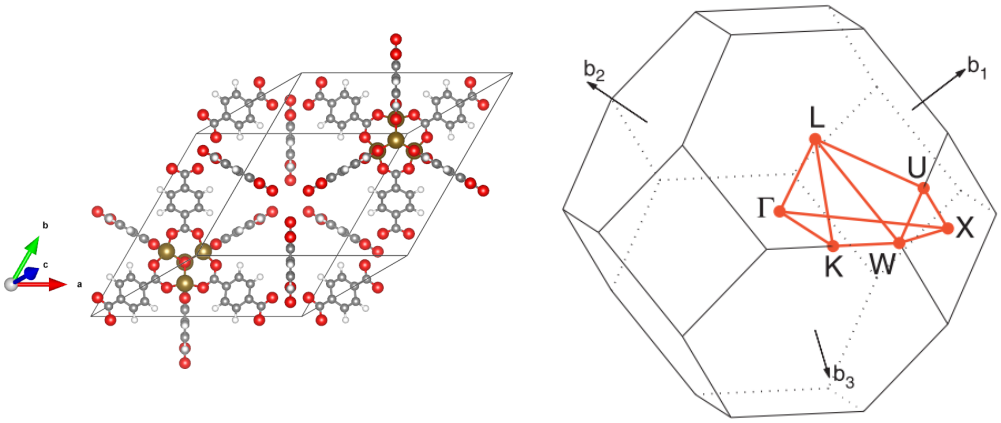


Figure 5.1: Primitive unit cell of IRMOF-1 and labeling of high symmetry points in the first Brillouin zone of an fcc lattice. Source: Setyawan et al. [64]

The third comparison should be with the use of our hypothetical IRMOF-130 with an oxalic acid linker. The calculation has been done with the parameterized force field discussed in section 4.1.2 for a 4x4x4 primitive supercell. The comparison of the dispersion bands with IRMOF-1(Mg) is shown in figure 5.4. At first glance one of the acoustic branches appears to have a much higher frequency for IRMOF-130. But on closer inspection one can see an avoided crossing for the acoustic band in IRMOF-1 in $\Gamma - X$ direction, which reaches up to 2.5 THz at the X high-symmetry-point. For IRMOF-130 this crossing is missing and one can see a somewhat larger frequency of 2.9 THz. When looking at the other high symmetry directions, we also observe the general trend of acoustic phonons showing higher energies. The simple linker in IRMOF-130 means, that there are much fewer optical modes in the low frequency regime, as the rotational motions and many bending modes of the aromatic rings are missing.

### 5.1.2 Paddlewheel MOFs

Phonon properties have also been analyzed for MOF-508 (bipyridine linker, figure 2.2b) and JAST-1 (DABCO linker, figure 2.2a) with zinc.
For MOF-508 the primitive cell is given as only one Zn-paddlewheel with its surrounding organic linkers. For the phonon calculation a 4x4x4 primitive supercell (3456 atoms) was used. The band structure for this system

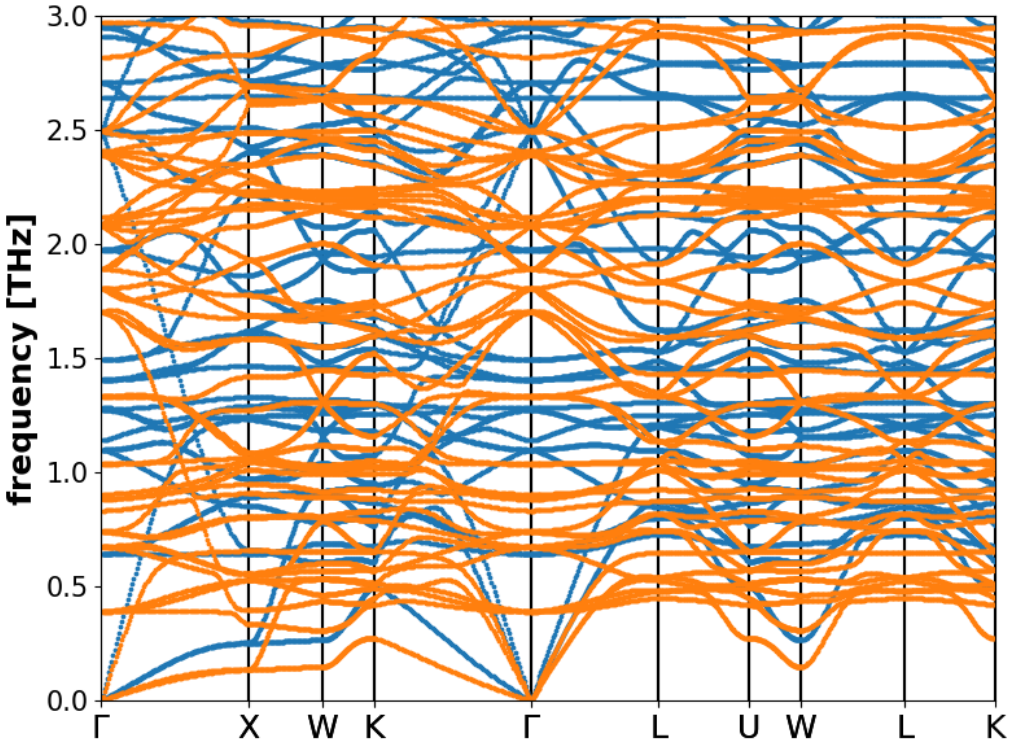


Figure 5.2: Comparison of low-energy phonon bands of IRMOF-1 (Zn) (blue) and IRMOF-10 (Zn) (orange)

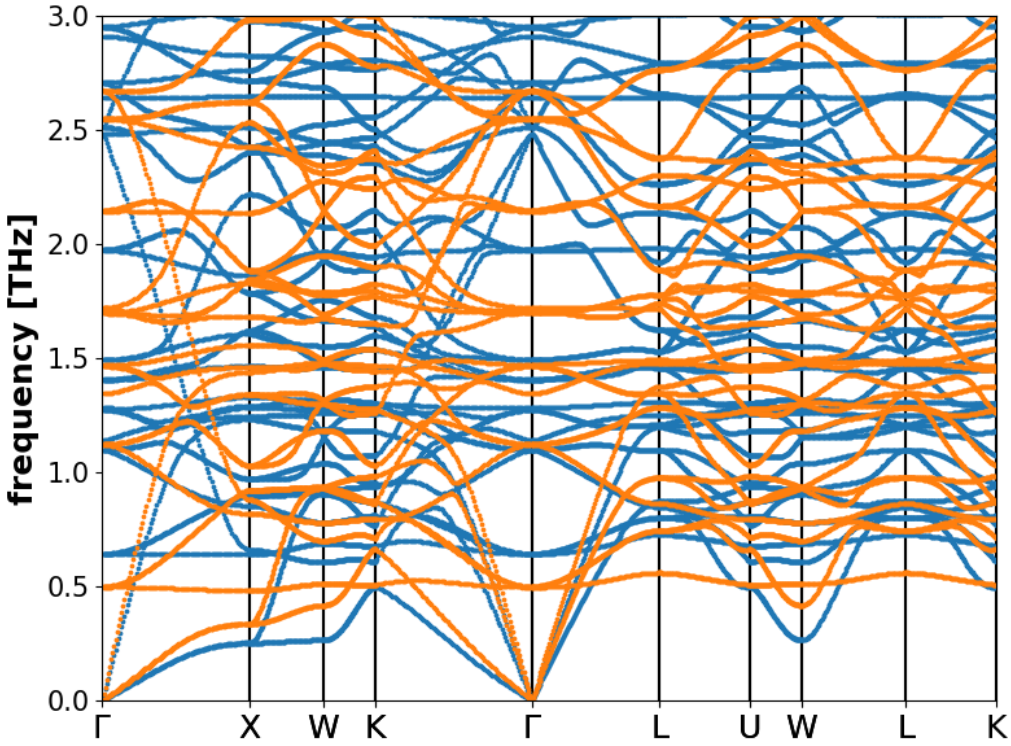


Figure 5.3: Comparison of low-energy phonon bands of IRMOF-1 (Zn) (blue) and IRMOF-1 (Mg) (orange)

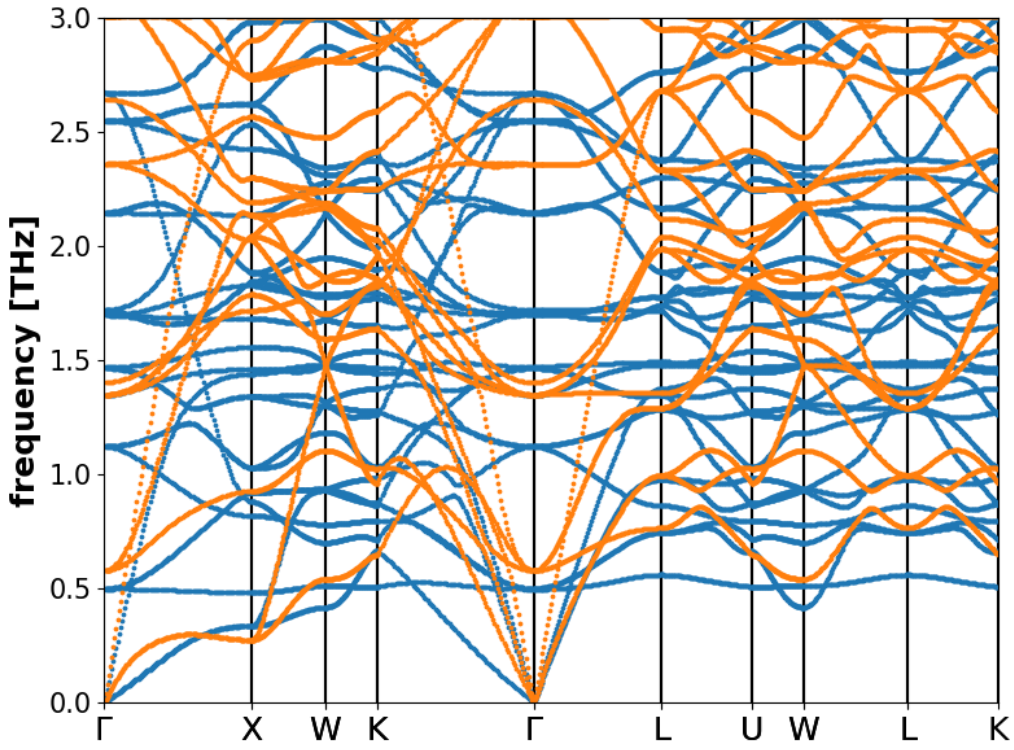


Figure 5.4: Comparison of low-energy phonon dispersion bands of IRMOF-1 (Mg) (blue) and IRMOF-130 (Mg) (orange)

is visualized in figure 5.5 and its corresponding primitive cell with the corresponding Brillouin zone in figure 5.6. The bands are given for a path for an orthorhombic lattice as the orientation of the bipyridine linkers prevent tetragonal symmetry. This appears to have very little impact on the low energy modes, as one can see in the symmetry of the band structure in Γ-X-S-Y-Γ and Z-U-R-T-Z. The Γ-X-S and Γ-Y-S bands would be equivalent in tetragonal symmetry, but show minor differences in MOF-508, especially at higher frequencies. The same is true for Z-U-R and Z-T-R. Noticeable is also the very flat and low lying band at about 0.4 THz. This is a rotation of the entire bipyridine linker while all nodes and other linkers remain idle. A similar mode can be seen at 1.5 THz where the rings in the bipyridine linker perform a mirror-inverted motion resulting in an even flatter band. There are also some isolated rotations of the therephthalic acid (TPH) linkers which can be found at 1.2 THz and are very flat. Additionally motions of the TPH linkers can be found isolated and in combination with vibrations including the bipyridines - those behave more like the motions that can be found in IRMOFs. Those generally show a much larger dispersion in the band structure.
For JAST-1 the geometry relaxation resulted in an off-center configuration of the phenylene based linkers leading to a larger primitive cell with two Zn-paddlewheels. The linkers were not angled completely planar in respect to the oxygen atoms connected to the inorganic node. The phonon calculation was carried out for a 4x4x4 primitive supercell (6912 atoms). The resulting bands can be seen in figure 5.7 with the primitive cell in figure 5.8. Again, one can see a number of symmetries in the phonon bands along some high-symmetry directions like for MOF-508 due to only small deviations from a tetragonal lattice. Similar to MOF-508 there are some very flat bands at 1 THz that represent rotations of the DABCO linkers. One can see an energy dip of the bands at the U-point. This is also related to the different orientation of the cell. The linkers in the x-y plane are oriented facing the corners of the orthorhombic cell instead of its faces. This means, that a phonon in Γ-U-direction in this geometrical configuration is more comparable to a phonon in Γ-X-direction in the geometry used for MOF-508. Due to the completely different nature of the nitrogen based linker there are no low lying bending modes that are otherwise prominent for the aromatic linkers.

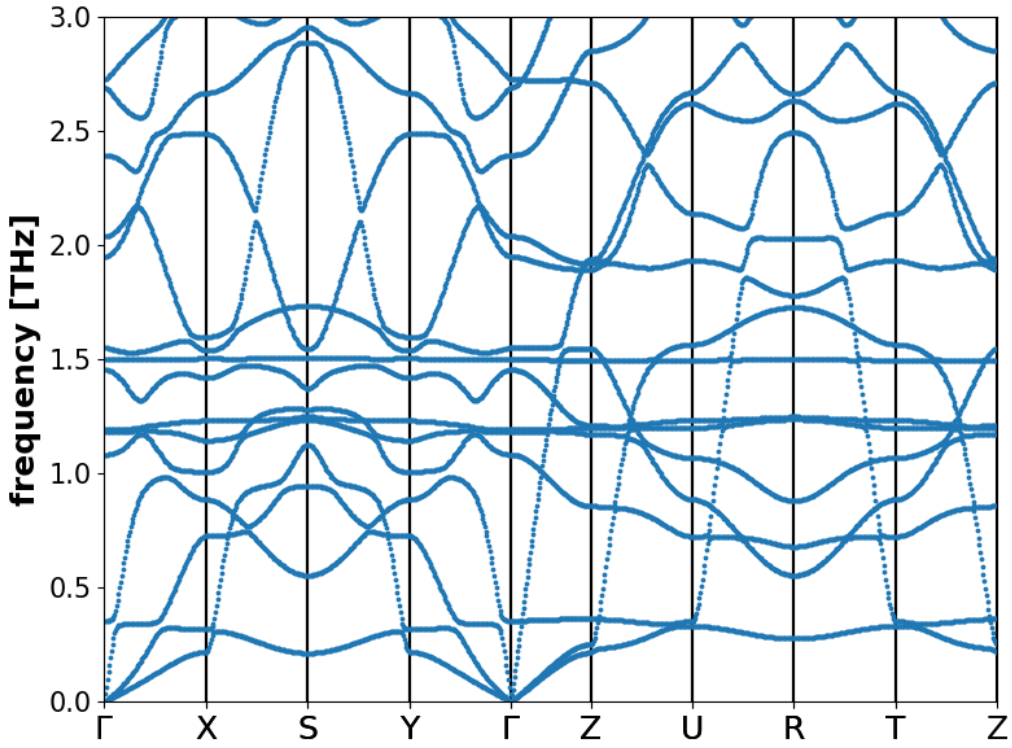


Figure 5.5: Low-energy phonon bands of MOF-508

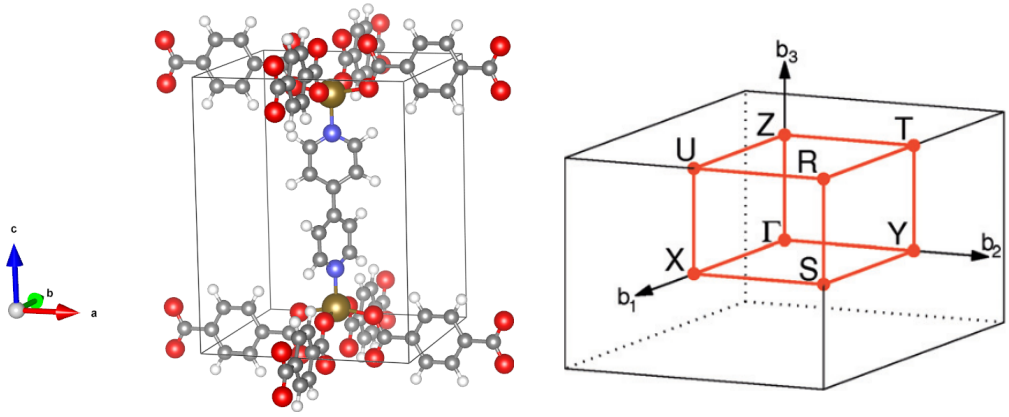


Figure 5.6: Primitive cell of MOF-508 with its corresponding Brillouin zone. Source: Setyawan et al. [64]

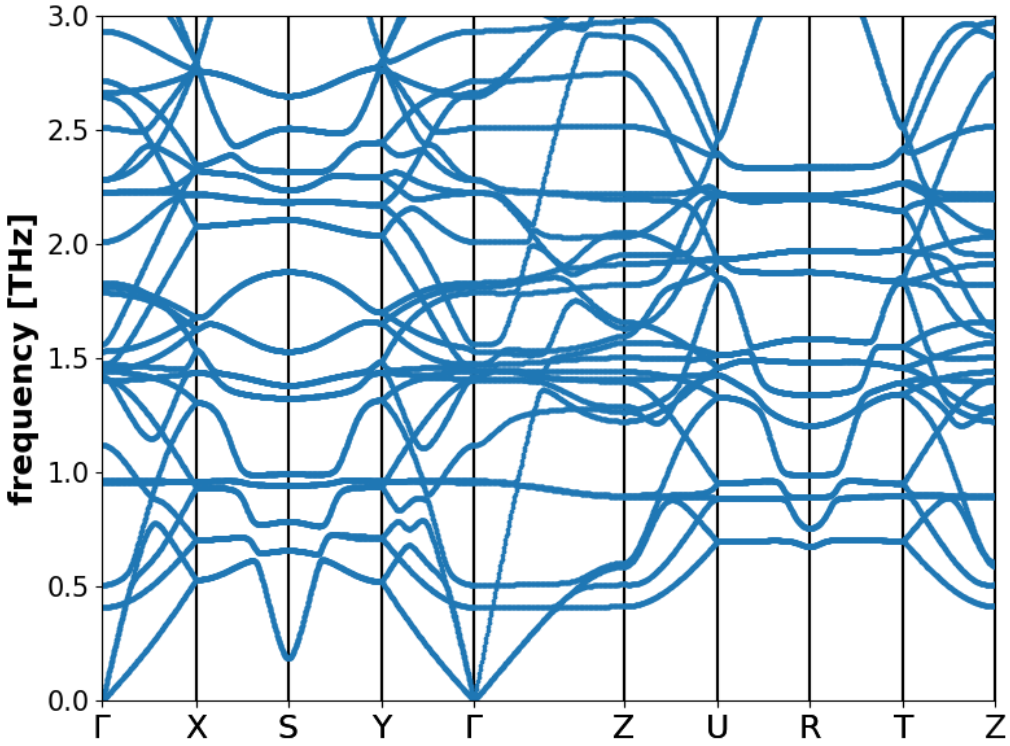


Figure 5.7: Low-energy phonon dispersion bands of JAST-1

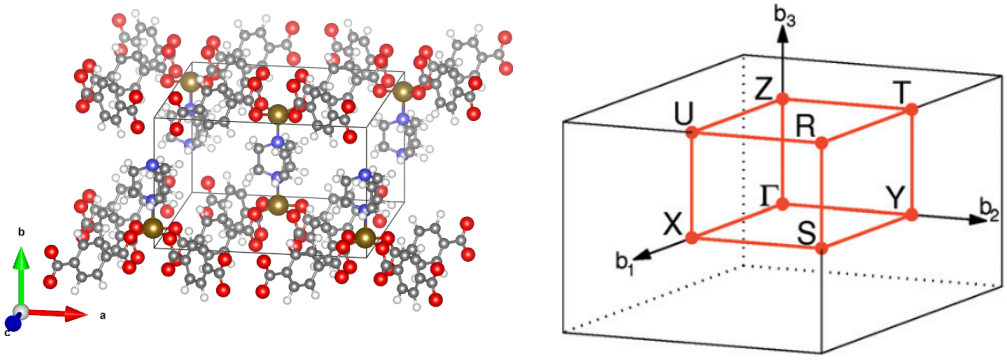


Figure 5.8: Primitive cell of JAST-1 with its corresponding Brillouin zone. Source: Setyawan et al. [64]

### 5.1.3 MOF-74

The last MOF to be considered was MOF-74 (see figure 2.3). The phonons have been calculated for a 3x3x3 primitive supercell (1458 atoms). The symmetries in MOF-74 conform to a dihedral lattice and the high symmetry points are labeled according to figure 5.10. The low frequency phonon bands are shown in figure 5.9. Note, that this band structure includes three times as high frequencies as the ones shown before. It almost seems like that the acoustic modes are separated from the optical modes like in many simpler materials. But this is somewhat misleading as several avoided crossings of the lowest optical with the acoustic bands can be seen. These acoustic modes seem to reach their highest value at about 4 THz for the high symmetry point Q. But the actual value is difficult to tell for certain, without evaluating the symmetries further, as the bands in this frequency region are very dense. In general, the bands show significantly more dispersion than in the other MOFs discussed before. Also there are no low frequency bands that are completely flat, as in the orthorhombic MOFs. This leads to significantly higher group velocities for low energy modes. Wit that, we would expect a significantly higher thermal conductivity for MOF-74 just based on the phonon dispersion bands. Of course, the thermal conductivity also depends on the phonon lifetimes for which the system's anharmonicities have to be investigated first.

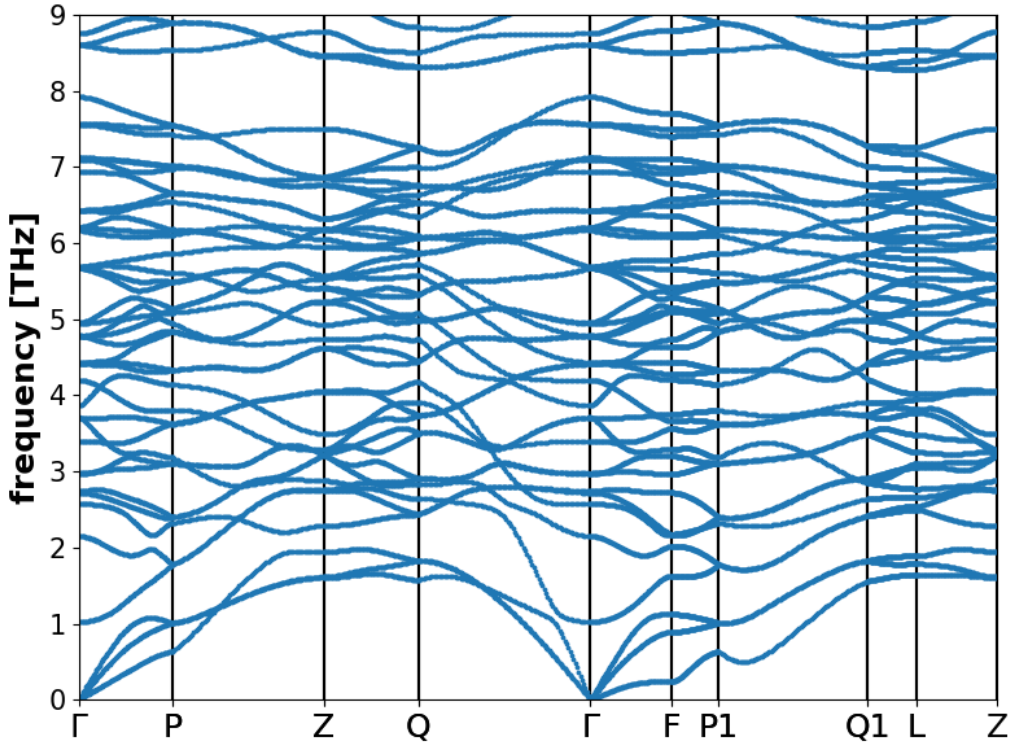


Figure 5.9: Low-energy phonon dispersion bands of MOF-74.

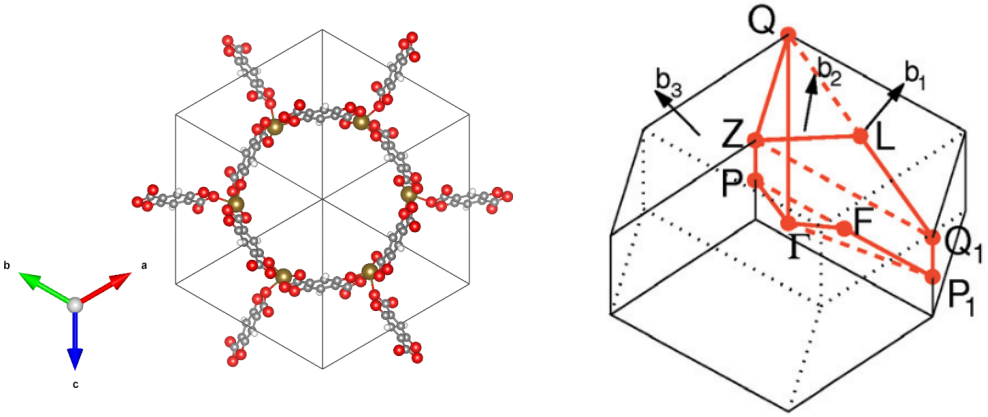


Figure 5.10: Primitive cell of MOF-74 with its corresponding Brillouin zone. Source: Setyawan et al. [64]

## 5.2 Volumes and thermal expansion

MD simulations are generally run at elevated temperatures. In order to thermalize a system (the process of assigning each atom proper velocities based on the total kinetic energy defined by a target temperature) it is normally sufficient to apply a thermostat in an NVT ensemble before the actual simulation run begins. But most materials undergo a thermal expansion process when heated, which would lead to cell vectors for a pressurized system when one merely uses the geometry obtained by a zero Kelvin relaxation. Therefore, in order to carry out accurate MD simulations, it is required to know the equilibrium volume at the temperature of interest. For this the cell parameters, as well as the volume, need to be allowed to change freely throughout the simulation in an NPT ensemble. As opposed to the thermalization, it is not sufficient to perform a brief MD run with a barostat at zero pressure and thermostat prior to the simulation. Since the observed cells are frequently relatively small (a few nm in each direction) applying a barostat will lead to massive pressure fluctuations which result in large variations of the cell parameters. Therefore, it is necessary to calculate the volume beforehand by statistically averaging over a sufficiently long MD simulation in the NPT ensemble. This then provides the cell parameters that will be used in further simulations.
For all investigated systems the equilibrium cell parameters at the temperatures of interest have been calculated. This section should give an overview of the thermal expansion that can be observed in investigated MOFs as a result. For most materials only the equilibrium volumes that are necessary for the subsequent thermal conductivity simulations were obtained. But for some systems the thermal expansion will be analyzed in more detail. This is relevant when investigating the thermal conductivity, as thermal expansion arises due to anharmonic effects.
The temperature dependent lattice parameters were obtained by first thermalizing a sufficiently large supercell in an NVT ensemble. The temperature is held constant by applying a Nose-Hoover chain thermostat. The investigated Metal-Organic frameworks reach equilibrium after a few ps of simulation time. For all systems an equilibration time of at least 10 ps was used to ensure a stable temperature.
After thermalization the simulation was run in an NPT ensemble where a Nose-Hoover chain barostat forces the pressure to be zero. The cell parameters were then permitted to change anisotropically during this time period.

The simulations were run in this stage for at least 100 ps and the resulting lattice parameters and volumes were recorded every 2 fs and subsequently averaged.
In figure 5.11 the thermal expansion of IRMOF-1 is visualized. The data has been obtained for a 2x2x2 supercell. The volume decreases linearly in the investigated temperature range from 100 K to 500 K. A linear fit leads to a negative linear thermal expansion coefficient of $\alpha = -8.3 \cdot 10^{-6}$ K$^{-1}$. This is in the range of predictions made by previous force fields that ranged from $-3$ to $-26.2 \cdot 10^{-6}$ K$^{-1}$ [65] but still significantly lower than the experimental data where results range from $-12$ to $-15.3 \cdot 10^{-6}$ K$^{-1}$ [66]. The reason for negative thermal expansion (NTE) has been investigated before and several responsible phonon modes have been identified. Mainly low frequency phonon modes are responsible for thermal expansion and some of those are visualized in figure 5.12. One mode contributing to NTE that is commonly mentioned in literature is a transverse motion of the rigid aromatic ring in IRMOF-1 [67, 68]. This motion is representative for the lowest lying optical mode in the phonon spectrum and is visualized in figure 5.12b. But it is not the only mode contributing significantly. Several other low lying rigid unit modes (RUMs) contribute towards the NTE based on their Gruneisen constants [68]. These RUMs are modes that do not distort their basic structural units (like tetrahedra, octahedra, etc.). This means that the modes can attain a low enough energy to be of significance as they correspond to a motion for a more simple geometry [69]. Additionally these modes can be NTE modes, which means that they lead to bond bending instead of longitudinal stretching, which would contribute to a positive thermal expansion. Most of the low lying modes in IRMOF-1 are either rigid rotations (see figure 5.12c) and rigid translations of node and linker without internal stretches of the individual atoms. Vibrations of the node typically do not impact thermal expansion much, as they cannot perform bending motions. Also, rotational vibrations of the organic linker are of little significance. In addition to this also the acoustic modes have been shown to be important for thermal expansion [68]. Here the bending of the linker-node structure in alternating layers is responsible for reducing the size of the unit cell. One acoustic mode at X-point is visualized in figure 5.12e. From here on we want to use these arguments as a basis for looking at the thermal expansion of MOFs, especially with different configurations of linkers.

Table 5.2 shows linear thermal expansion coefficients for different MOFs that were investigated in more detail. The values were obtained by perform-

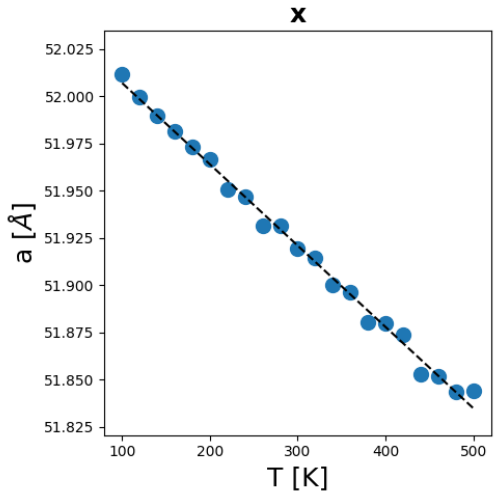


Figure 5.11: Thermal expansion of IRMOF-1 in x direction based on an NPT simulation

ing a linear fit over the lattice constants in a temperature range from 100 K to 500 K. The values for isoreticular MOFs have been averaged over all directions to minimize the error.

Table 5.2: Linear lattice thermal expansion coefficients for various MOFs in all Cartesian directions. For the anisotropic MOFs, the equal linkers are facing in y and z direction. All values given in $10^{-6}$ $K^{-1}$

| **System** | $\alpha_{\mathbf{x}}$ | $\alpha_{\mathbf{y}}$ | $\alpha_{\mathbf{z}}$ |
|---|---|---|---|
| IRMOF-1 (Zn) | -8.3 | -8.3 | -8.3 |
| IRMOF-10 (Zn) | -11.2 | -11.2 | -11.2 |
| IRMOF-16 (Zn) | -18.6 | -18.6 | -18.6 |
| IRMOF-1 (Mg) | -9.6 | -9.6 | -9.6 |
| IRMOF-130 (Mg) | -15.1 | -15.1 | -15.1 |
| MOF-10-1-1 (Zn) | -11.2 | -8.8 | -8.8 |
| MOF-508 (Zn) | +2.0 | -7.0 | -7.0 |
| JAST-1 (Zn) | +10.1 | -10.6 | -10.6 |
| MOF-74 (Zn) | +4.0 | 3.7 | 7.6 |

It can be seen that the isoreticular MOFs with the longer biphenyl- and

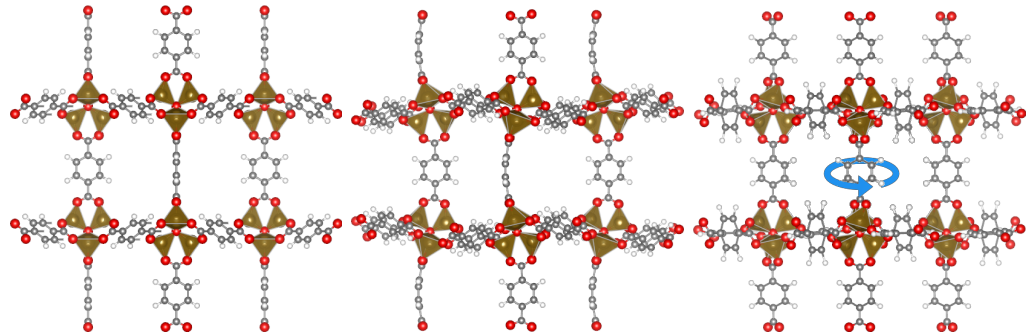

(a) Idle structure for reference

(b) Translations of the linkers at 0.64 THz

(c) Rotations of the linkers at 1.14 THz

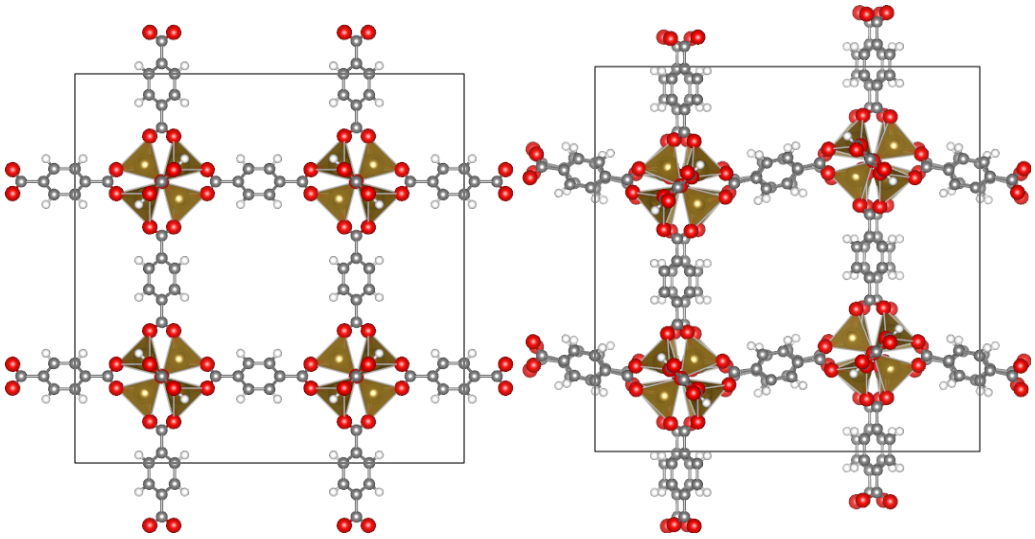

(d) Idle structure for reference

(e) Acoustic mode at X-high symmetry point showing the shearing motion of alternate layers.

Figure 5.12: Various vibrations occuring in IRMOF-1. (a) and (d) serve as a reference as a not displaced structure while (b) and(c) show the displaced cell along the normal modes at $\Gamma$. (d) visualizes one acoustic mode at $X$.

terphenyl-based linkers, IRMOF-10 and IRMOF-16, show a larger thermal contraction than IRMOF-1. By investigating the low frequency modes of IRMOF-10 one can observe very similar rigid translational motions of the organic and inorganic components as compared to IRMOF-1. The different organic linkers impact these vibrations in that there is an additional angle bending at the connecting bond between the phenyl rings. This implies that both aromatic rings represent a separate rigid unit. A reason for the higher NTE in IRMOF-10 is the fact that the contributing phonon modes, both the optical and the acoustic ones, are lying significantly below those of IRMOF-1 in the low frequency regime and, therefore, contract the cell more upon heating.
The NTE for Magnesium-IRMOF-1 is slightly higher than for IRMOF-1. This is very easy to explain by the fact that the lower mass of the Mg atoms decreases the energy of the phonon modes, which should be very similar due to an almost equal geometry. But this MOF provides a possible comparison to the IRMOF-130 with Mg where a significantly higher thermal contraction than for IRMOF-1 can be observed. At this point, it has to be noted that the agreement of the force-field and the reference DFT frequencies is somewhat poor for the most important optical phonon mode and it is very possible that the thermal expansion is overestimated. Still, when we compare the dispersion bands solely provided by the FF (see figure 5.3), we can see that the conditions for the higher thermal contraction, as was the case for IRMOF-10, do not apply for IRMOF-130. The acoustic modes are even somewhat higher and the lowest optical modes occur at a similar energy. In general there are a lot fewer low frequency modes for IRMOF-130 due to the simple linker. But a more thorough investigation would need to be carried out in order to tell for certain.

Another curious aspect of the thermal expansion in MOFs is given by the anisotropic paddlewheel MOFs like JAST-1 or MOF-508. Here, the lattice parameter in the direction of the nitrogen based linkers shows an increase while the other directions show a negative thermal expansion, reminiscent of IRMOF-1. In direction of the bipyridine linker in MOF-508 only a very low positive thermal expansion can be observed. For JAST-1 the thermal expansion in the direction of the DABCO linkers is significantly higher than for the bipyridine. In both cases the NTE coefficient in the direction of the terephthalic acid is similar to IRMOF-1. All of this leads to the conclusion that the organic linkers appear to be the most significant factor for negative thermal expansion, which is consistent with previous findings.

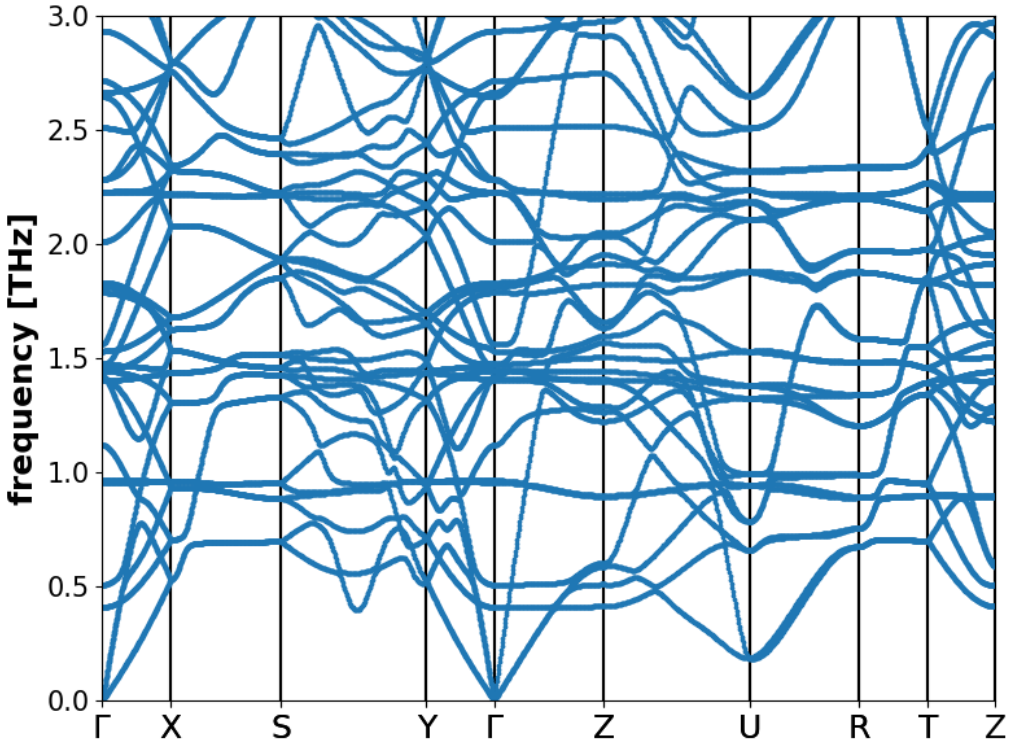


Figure 5.13: Thermal expansion coefficients of JAST-1 in the directions of the phenyl based linkers (x,z) and of the DABCO based linkers (z).

Table 5.3 gives an overview of all lattice parameters of the MOFs at 300 K relative to their 0 K values that are needed for the thermal conductivity simulations. In the following, the simulation details for each of the investigated materials will be elaborated. The values for the Zn-IRMOFs have been obtained using a 2x2x2 conventional supercell. All calculations have been made after a sufficiently long time to achieve neglectable statistical errors of less than $10^{-4}$Å. The lattice parameter for IRMOF-1 at 160 K of 25.991 Å compares reasonably well to experimental x-ray diffraction obtained data of 25.885 at 169 K [70]. The cells for IRMOF-1 with scaled masses have not been relaxed at 0 K, as a difference in the atomic masses should not change the minimum energy configuration. There also appears to be only a minimal difference for the lattice parameters with changed masses at elevated temperatures. IRMOF-1 with magnesium was calculated from a 3x3x3 cell and shows a somewhat higher lattice parameter than the version with zinc. This likely results from the different reference data for the parameterization process, as the lattice constant obtained from DFT amounted to 26.20 Å. This is different from the parameterization of IRMOF-130 (Zn) that has been parameterized without periodic boundary conditions. All values of the tetragonal $ZnO_4$ MOFs were also based on 2x2x2 conventional supercells and the resulting cell lengths are very similar to the values of their respective isoreticular frameworks. Lattice parameters for the paddlewheel MOFs MOF-508 and JAST-1 are given based on calculations carried out for a 4x4x4 primitive unit cell.
The temperature dependent lattice parameters of MOF-74 are considered separately, as it lacks the orthorhombic symmetry. For this material thermal expansion is positive in all directions. Table 5.4 shows the cell parameters for a few temperatures that were obtained from an NPT run of a 3x3x3 primitive supercell. The thermal expansion values obtained from a linear fit over this temperature range in Cartesian directions are shown in table 5.2. The tilt angle of the cell remained unchanged for the different temperatures. It can be seen that the thermal expansion is significantly higher in the direction of the node-chain. In x and y directions similar values are obtained. Considering the symmetry of MOF-74 those two directions should be equal, and the difference arises only due to inaccuracies of the simulation. Following the previous considerations for the origin of negative thermal expansion, the positive coefficient can easily be explained with the increased rigidity of the atoms. The aromatic linkers in x and y direction are attached to twice as many external atoms holding them in place. This hinders the organic linkers

Table 5.3: Equilibrium lattice parameters in Cartesian coordinates of the respective conventional cells for MOFs considered in this work.

| **System** | **0 K** | | | **300 K** | | |
|---|---|---|---|---|---|---|
| | **x**[Å] | **y**[Å] | **z**[Å] | **x**[Å] | **y**[Å] | **z**[Å] |
| IRMOF-1 (Zn) | 26.079 | 26.079 | 26.079 | 25.960 | 25.960 | 25.960 |
| Mg mass | | | | 25.959 | 25.959 | 25.959 |
| Ca mass | | | | 25.957 | 25.957 | 25.957 |
| Znx2 mass | | | | 25.956 | 25.956 | 25.956 |
| linker x 0.75 mass | | | | 25.958 | 25.958 | 25.958 |
| linker x 0.5 mass | | | | 25.956 | 25.956 | 25.956 |
| linker x 1.5 mass | | | | 26.961 | 26.961 | 26.961 |
| linker x 2.0 mass | | | | 26.961 | 26.961 | 26.961 |
| IRMOF-10 (Zn) | 34.511 | 34.511 | 34.511 | 34.388 | 34.388 | 34.388 |
| IRMOF-16 (Zn) | 42.997 | 42.997 | 42.997 | 42.762 | 42.762 | 42.762 |
| IRMOF-1 (Mg) | 26.193 | 26.193 | 26.193 | 26.111 | 26.111 | 26.111 |
| IRMOF-130 (Mg) | 17.644 | 17.644 | 17.644 | 17.560 | 17.560 | 17.560 |
| MOF-10-1-1 (Zn) | 34.637 | 26.028 | 26.028 | 34.421 | 25.951 | 25.950 |
| MOF-16-1-1 (Zn) | 42.982 | 26.079 | 26.079 | 42.829 | 25.925 | 25.925 |
| MOF-10-16-16 (Zn) | 34.517 | 42.982 | 42.982 | 34.316 | 42.732 | 42.732 |
| MOF-508 (Zn) | 14.0725 | 11.002 | 11.002 | 14.89 | 10.98 | 10.98 |
| JAST-1 (Zn) | 9.613 | 11.003 | 11.003 | 9.639 | 10.965 | 10.967 |

to perform the motions typical for NTE. In z direction, the absence of linkers and the rigidity of the structure means that not even the shearing motion caused by the acoustic modes leads to negative thermal expansion.

Table 5.4: Temperature dependent lattice parameters for a 3x3x3 MOF-74 supercell from NPT simulations. All length values are given in Å.

| T [K] | x | y | z | xy | xz | yz |
|---|---|---|---|---|---|---|
| 100 | 45.78 | 40.47 | 19.26 | -21.43 | -21.43 | -35.60 |
| 200 | 45.80 | 40.48 | 19.27 | -21.44 | -21.44 | -35.60 |
| 300 | 45.81 | 40.49 | 19.29 | -21.44 | -21.45 | -35.64 |
| 400 | 45.84 | 40.51 | 19.30 | -21.45 | -21.47 | -35.66 |

## 5.3 Thermal conductivity

In this section the results for the thermal conductivity in metal-organic frameworks will be discussed in detail. First IRMOF-1 (Zn) will be presented and compared to experimental data. Then, the impact of different internal mass ratios, metals and linkers in IRMOF-1 will be considered. The impact of linker length in $Zn_4O$ MOFs will be investigated by calculating the thermal conductivity for isotropic and anisotropic MOFs. Finally, MOF-508, JAST-1 and MOF-74 will be considered to provide some insights about different architectures.

### 5.3.1 IRMOF-1

The thermal conductivity for IRMOF-1 was calculated using equilibrium and non-equilibrium molecular dynamics methods. At 300 K the thermal conductivity was also calculated using up to 4x4x4 cells. The resulting value changed only within the error margins. Due to this, for other systems, a supercell of similar size was considered sufficient. For the NEMD calculations several cell lengths were used to account for finite size effects. For this 4x2x2, 6x2x2, 8x2x2 and 10x2x2 cells were used to extrapolate to the infinite size limit. The 2x2 supercell in the cross-sectional direction was found to be necessary in order to avoid thermal instabilities and to achieve steady state in a reasonable time-frame. The temperature difference compared to equilibrium for the hot and cold thermostat was set to ±50 K. Here also different temperature differences were tested ranging from ±25 K to ±100 K and the values for the thermal conductivity, disregarding finite size effects, were found to be within an error of ±10 %. In addition to this, no systematic behavior could be observed. This confirms the validity of Fourier's law and

implies that nonlinear response effects are negligible [19] in this temperature range. The resulting temperature dependent values are shown in figure 5.14. They are compared to the only available experimental data for an empty IRMOF-1 lattice [18]. Other investigations have been carried out for low density IRMOF-1 [71] or with additives [72], but not for the empty crystalline lattice. It can be seen that the results obtained from the Green-Kubo method appear to be consistently lower than those calculated with NEMD. At a temperature of 300 K the molecular dynamics results agree well with experiment. In the low temperature regime below 100 K the experiment shows the typical trend for the thermal conductivity that cannot be captured with classical molecular dynamics simulations, as these are due to low temperature effects that rely on a proper quantum-mechanical description. It can also be observed that the temperature dependence of the simulated and experimental data does not appear to match, but the error bars are large for both approaches and the differences in thermal conductivities are very low. In addition it is impossible to completely exclude the presence of defects or residue solvents in the experimental setup that might have affected the results. Without additional measurements it is difficult to conclude a major flaw with either method. Huang et al. [62] analyzed molecular dynamics results from the Green-Kubo method in more detail and identified contributions from optical modes as the cause of an increase in thermal conductivity. This assessment was based on filtering the high frequency contributions from the heat-current autocorrelation function [73]. In those simulations the temperature dependence also matched the experimental data. In any case, the temperature dependent thermal conductivity will not be a major topic in this work and most simulations from now on are carried out at a temperature of 300 K. With a value of 0.35 W/(m K) at 300 K the thermal conductivity for this material is extremely low. It has been previously reported that higher values can be achieved by the addition of expanded natural graphite [72] or interpenetration [74] and a reduction can result from gas inclusion [75]. But there are also studies that indicate an increase in thermal conductivity by loading with gas [22].

Something curious that has been observed when carrying out the NEMD simulations is visualized in figure 5.15. Here we can see the temperature profile between two thermostats showing multiple terraces. The steepest steps occur between the bond of the zinc and the oxygen atoms conntected to the organic component, while the temperature remains roughly constant across node and linker. This implies that the greatest bottleneck for thermal trans-

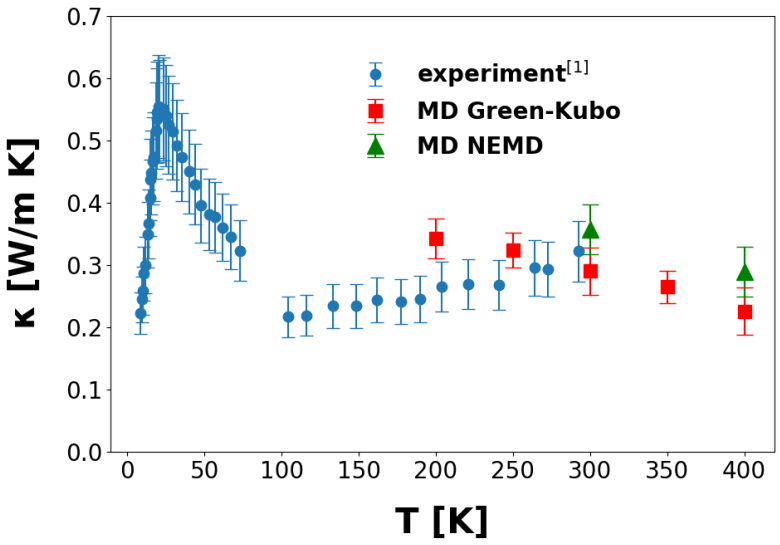


Figure 5.14: Temperature dependent thermal conductivity of IRMOF-1 based on equilibrium (Green-Kubo, GK) and non-equilibrium molecular dynamics (NEMD) simulations with MOF-FF

port in IRMOF-1 is the interface between organic and inorganic components. One of the possible reasons for this phenomenon could be the large mass mismatch between node and linker. This can lead to a lower vibrational overlap at the interface, which results in increased scattering in this area and in turn to a reduced thermal conductivity.

In order to analyze the impact of the mass mismatch between node and linker, thermal conductivity simulations were carried out for IRMOF-1 with the masses of the individual atoms changed to provide a different mass ratio. In these simulations, the force-field interactions remain unchanged. A similar investigation has been carried out in the past [22], where only the entire node and the entire linker were mass-scaled. This will be investigated in more detail, by not only scaling the nodes and linkers, but by also scaling the metal-atoms, which are much easier to replace in a realistic material. The results of this investigation can be seen in figure 5.16. All simulations have been carried out with NEMD using the same settings as for the base IRMOF-1 for 4x2x2, 6x2x2 and 8x2x2 supercells. In addition to the scaled Zn-IRMOF-1, also the thermal conductivity for the Mg-IRMOF-1 with different parameters

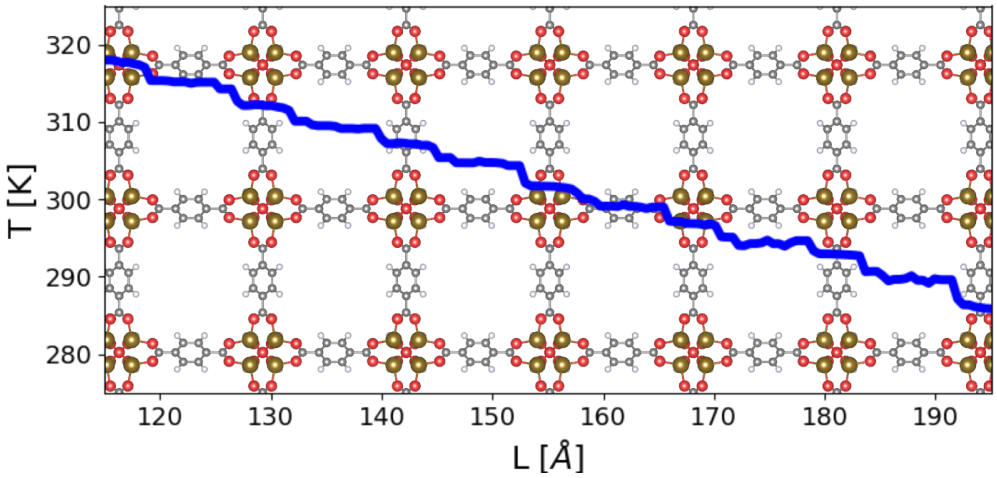


Figure 5.15: Temperature profile of IRMOF-1 (Zn) during a NEMD simulation in steady state for 300 K

are shown at the corresponding mass compared to Zn. This value has been obtained using the Green-Kubo method for a 2x2x2 supercell. It can be seen that the difference in thermal transport between both of these materials is mostly given by the metal mass. This is why further parameterization for IRMOF-1 with different metals that could chemically replace Zn like Ca have not been carried out. The other data point with a metal mass lower than Zn has the same mass as calcium. In addition to the simulated values an expected trend for the thermal conductivity depending on the masses is displayed. In the case of an ideal gas one would expect a proportionality of $\kappa \propto 1/\sqrt{m}$ when scaling the masses of all atoms in the system. This arises due to the heat capacity and mean free path being independent of the mass, making the atom velocities the only mass dependent factor. These are then given by

$$v \propto \sqrt{\frac{RT}{m}} \tag{5.1}$$

with $R$ the ideal gas constant. This assumption is, of course, a bit naive for a crystalline solid where one needs to consider all phonon modes in the system to obtain a true mass dependence. But since the phonon frequency is also related to the mass by $\omega \propto 1/\sqrt{m}$, all distribution functions included in the phonon lifetimes would have to be evaluated to obtain the true mass

dependence. This has not been performed, as the reference mass dependence given should only indicate a rough guide to the expectation.

Figure 5.16 also visualizes some clear trends based on the scaled masses. When the masses of the linkers (which is defined as the carbon and hydrogen atoms in this case) are adjusted, there does not appear to be a large difference in thermal conductivity within the error for both heavier and lighter masses. This is inconsistent with the assumed proportionality where one would expect a higher thermal conductivity for lower masses. The likely explanation for this phenomenon is, that with a reduction in linker mass one also increases the mass mismatch between the organic and inorganic component. This, in turn, reduces the thermal conductivity providing the opposite effect as the mass scaling. The inverse is true for increased linker masses. This can be seen even better for the metal scaling. Here, a twice as high thermal conductivity can be observed for masses equivalent to magnesium. This implies that also here the reduction of the mass mismatch by reducing the node mass should be an important contribution in increasing the thermal conductivity in addition to the natural increase due to lighter masses. Again, the inverse is true for higher metal masses.

Additionally, the mass of the entire node as defined by Han et al. [22], so all metal and oxygen atoms, have been scaled as a comparison. The masses were scaled to 65% of the original node mass and the thermal conductivity was calculated for 4x2x2, 6x2x2 and 8x2x2 cells to extrapolate the infinite size limit. A thermal conductivity of 0.57 W/(mK) was obtained as a result. The scaling of the metal atom under this condition is with 42.497 $m_a$ very close to the mass of calcium with 40.078 $m_a$. The resulting thermal conductivity is very similar to the value of 0.58 that was obtained for only scaling the metal mass to calcium. But in total, the mass for the full node scaled system should be significantly lower. This might indicate that internal mass differences between oxygen and metal also plays a more significant role. But the error for these values is still significant and in order to truly understand what difference the masses inside the node cause, further investigations would have to be carried out.

In order to see more clearly how the different mass differences affect the interface, it is of interest to investigate the step-terrace profiles for the mass-scaled systems. These step-like structures have been observed previously in superlattices of inorganic materials by Lin et al. [76]. In this study, efforts have been made to understand the thermal conductivity in GeSi superlattices with different periodic lengths. In order to do this, the contributions to the

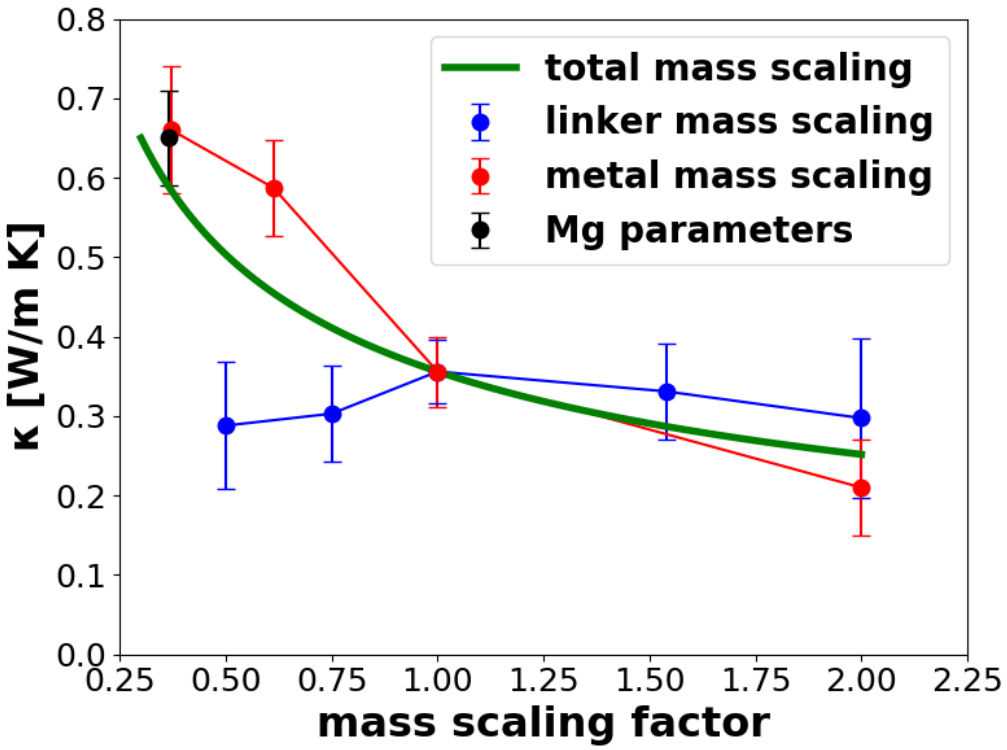


Figure 5.16: Thermal conductivity values for IRMOF-1 (Zn) with scaled masses for the metal atoms (red) and for entire carbon/hydrogen linkers (blue). Note that those have been obtained by applying the interatomic model for IRMOF-1 (Zn). The black data corresponds to IRMOF-1 parameterized for magnesium. The green curve indicates the expected temperature trend if one were to scale the mass of the entire system.

thermal conductivity for the individual components in the superlattice have been separated. Similarly, this work employs following simple expression to separate the contributions:

$$\frac{1}{\kappa} = \sum_i \frac{1}{\kappa_{node,i}} \frac{l_{node}}{L_{tot}} + \sum_i \frac{1}{\kappa_{linker,i}} \frac{l_{linker}}{L_{tot}} + \sum_j \frac{1}{\kappa_{int,j}} \frac{a_{int}}{L_{tot}} \tag{5.2}$$

Here $\kappa_{node}$, $\kappa_{linker}$ and $\kappa_{int}$ are the thermal conductivities occurring across the building block or the interface, $L_{tot}$ is the total length of the cell, $l_{node}$ and $l_{linker}$ are the lengths of the nodes and linkers and $a_{int}$ is defined as the distance between node and linker where no atoms are positioned. The partial thermal conductivities in the nodes and linkers have been obtained by linearly fitting the averaged kinetic energies of each individual building blocks leading to a temperature gradient. The values for the interfaces filled the gaps between the fits for linkers and nodes in the temperature profile. Care has been taken to exclude any components near the thermostats. This analysis was carried out for mass scaled IRMOF-1 (Zn) and the results are shown in figure 5.17. For all these simulations an 8x2x2 supercell was used in order to obtain the temperature profile. For the partial thermal conductivity values of nodes and linkers it is difficult to see clear trends with mass scaling. This is due to the relatively large error resulting from fitting very flat slopes. When looking at the thermal conductivity across the linker in figure 5.17e for different linker masses, one can make out a lower thermal transport for higher masses. This is consistent with the expectation that an increased mass of a system will lead to a lower thermal conductivity. Similarly, we should expect such a trend in figure 5.17a when varying the metal masses. But the difference in thermal conductivity is relatively low. Aside of the large error, this could also be attributed to the fact that the partial thermal conductivity across the nodes was recorded, not only across the nodes, but also including all the cross-linkers perpendicular to the direction of heat flow. Also the situation is different, in that only a small part of the building unit was scaled.

A much more clear statement can be made when looking at the interface conductivities in figure 5.17c and 5.17f. Here, reducing the metal masses and, therefore, reducing the mass mismatch leads to a higher thermal conductivity. Similarly, when increasing the linker mass, a clear increase in interface conductivity can be observed. This is consistent with previous assumptions and confirms, that the mass difference between node and linker plays a major role for thermal transport.

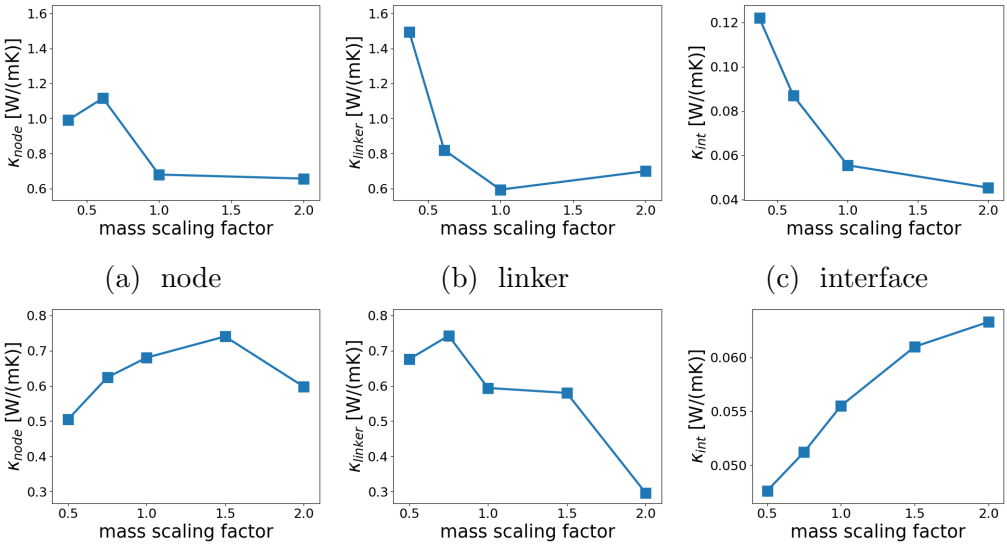


(a) node (b) linker (c) interface

(d) node (e) linker (f) interface

Figure 5.17: Partial thermal conductivities – split in nodes, linkers and interfaces – for IRMOF-1 (Zn) with scaled metal (a,b,c) and linker (d,e,f) masses.

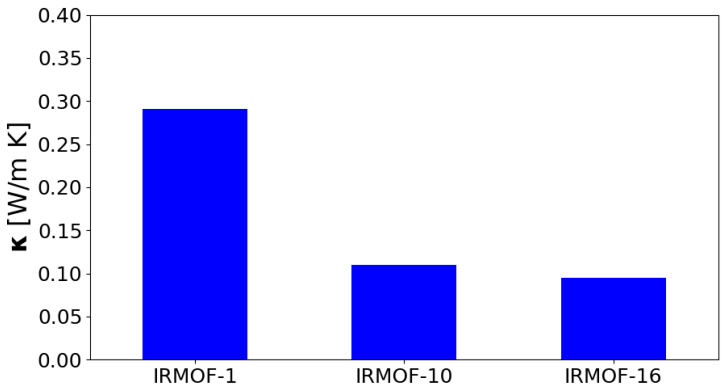


Figure 5.18: Thermal conductivity values for IRMOF-1 (Zn), IRMOF-10 (Zn, BPDC linker) and IRMOF-16 (Zn, TPDC linker) from Green-Kubo simulations of a 2x2x2 supercell.

### 5.3.2 $Zn_4O$ MOFs with different linkers

In order to analyze the impact of linker length, $Zn_4O$ IRMOFs with Biphenyl-4,4'-dicarboxylic acid (BPDC) and p-Terphenyl-4,4"-dicarboxylic acid (TPDC) linkers have been analyzed and compared to the regular terephthalic acid (TPH) linker based MOFs. These frameworks are commonly referred to as IRMOF-10 and IRMOF-16. The simulations were carried out using the Green-Kubo method with a 2x2x2 supercell of the conventional unit cell for each system. The resulting values for the thermal conductivity can be seen in figure 5.18. The values are lower by a factor of 2-3 than for the reference system. The interfaces between node and linker, which can be seen as a major barrier to thermal transport, as discussed in 5.3.1, are less frequent in these MOFs. So one might expect a higher thermal conductivity, but since the linker length has been expanded in all Cartesian directions, the linker-density in the cross-sectional area that can conduct heat is much lower. This is why a significantly lower thermal conductivity is unsurprising.
To analyze the actual impact of the length of the linkers, additional anisotropic MOFs have been studied. One of these structures is displayed in figure 5.19. This system has a BPDC linker in one direction and a TPH linker in the other two directions. The main focus should be on the MOF-BPDC-TPH-TPH and MOF-TPDC-TPH-TPH, where the molecule abbreviations indicate the linkers in different Cartesian directions. These systems have the same

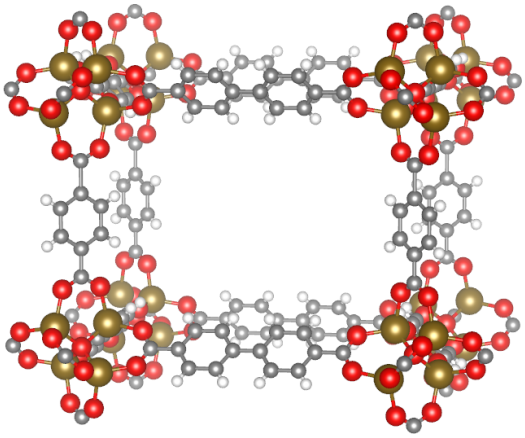

Figure 5.19: Example structure of an anisotropic MOF. This MOF-BPDC-TPH-TPH has a different linker in one direction of heat transport leading to an equal cross-sectional linker density as in IRMOF-1.

cross sectional linker density as IRMOF-1 in one direction. The thermal conductivity of these materials has then been calculated using the Green-Kubo method from 2x2x2 supercells. The results compared to their isoreticular counterparts can be seen in figure 5.20. The thermal conductivity of these MOFs in direction of the longer linkers is rather similar to IRMOF-1. This is somewhat surprising, as with the increased length of the organic component one would expect a higher thermal conductivity due to a lower density of node-linker interfaces.

NEMD simulations have been utilized to analyze the barriers of thermal transport in the MOF-BPDC-TPH-TPH and MOF-TPDC-TPH-TPH. Visually the temperature profile is very similar to what has been shown for IRMOF-1 in figure 4.15b. The temperature profile for the heat flow in a 8x2x2 supercell of MOF-BPDC-TPH-TPH in the direction of the BPDC linkers is shown in figure 5.21. In this profile the high thermal conductivity across the organic component becomes more evident while there appears to be a slightly larger thermal resistance across the inorganic node.

In a previous study [77], a simple model has been used to relate the pore size in MOFs with thermal conductivity. What was seen in this work, was a linear relationship between the thermal conductivity $\kappa$ and the inverse cross-sectional area of the pores. Using the data obtained for $Zn_4O$ MOFs, we

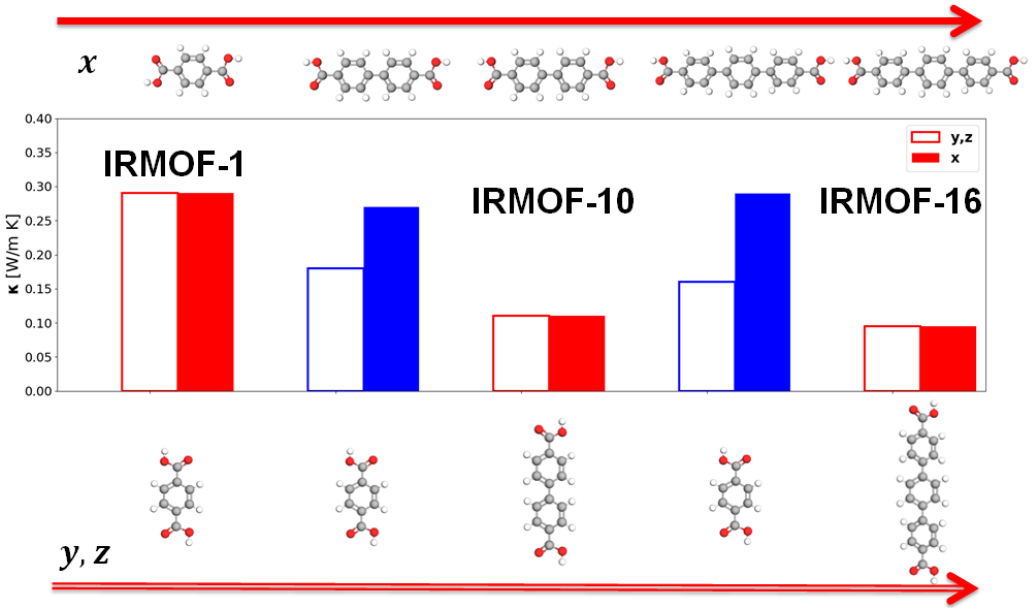


Figure 5.20: Anisotropic thermal conductivity values for MOF-BPDC-TPH-TPH and MOF-TPDC-TPH-TPH compared to the thermal conductivities of their isoreticular counterparts. Values have been obtained using the Green-Kubo method for a 2x2x2 supercell.

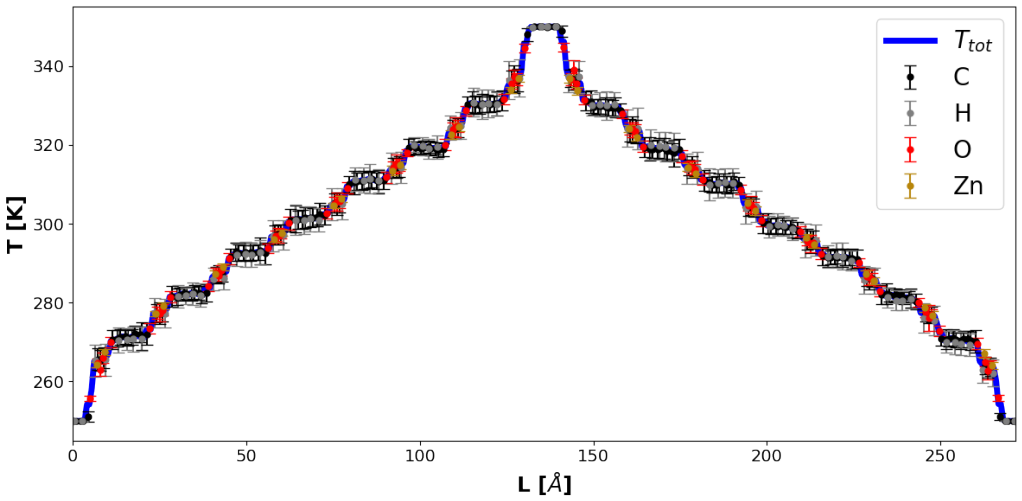


Figure 5.21: Temperature profile of a 8x2x2 supercell of MOF-BPDC-TPH-TPH during a NEMD simulation at 300 K in the direction of the long linkers. The errorbars show the spread of the atomic temperatures.

can now try to investigate this relationship with MOFs modeled on an atomistic level. Figure 5.22 relates the thermal conductivity to the cross-sectional area perpendicular to heat flow. Note that the anisotropic MOFs will show multiple values in the figure. It can be seen, that there does seem to be a certain degree of linear increase of the thermal conductivity with reduction of pore size. There are some outliers, but especially low values are difficult to judge due to their inherently large error arising from noisy autocorrelation functions in the Green-Kubo method.

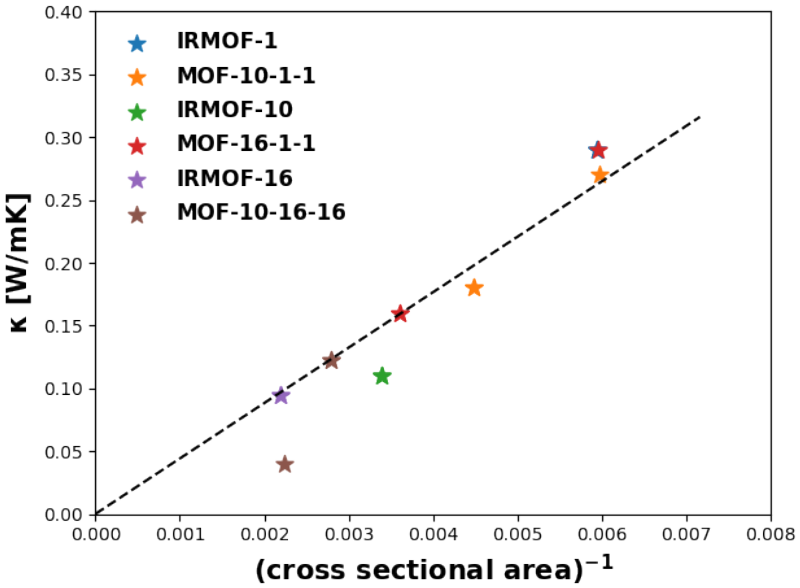


Figure 5.22: Thermal conductivity of various $Zn_4O$ MOFs related to the inverse cross-sectional area between the nodes perpendicular to heat flow. Values have been obtained using the Green-Kubo method. A linear fit that passes through zero has been included.

### 5.3.3 IRMOF-130 (Mg)

The thermal conductivity has also been calculated for IRMOF-130 (Mg), with oxalic acid as the linker. Both the Green-Kubo method and NEMD have been utilized to obtain the thermal conductivity. Due to the smaller primitive unit cell, a 4x4x4 supercell was used for Green-Kubo. This resulted in a thermal conductivity of 1.15 W/(mK) at 300 K. In case of NEMD 4x2x2 up to 16x2x2 supercells have been used to extrapolate the infinite size limit which leads to 1.34 W/(mK) at 300 K. Again, we can see a slightly larger value for NEMD, but both results are in the same order of magnitude. This is also approximately two times as high, as the value for IRMOF-1 (Mg). This MOF obviously shows a much higher cross-sectional linker density, which would lead to a higher expected thermal conductivity. Also, when looking at the temperature profile from the NEMD simulations in figure 5.23, the step-like structure is much less pronounced. The thermal conductivities across the steps between the linker oxygens and the node metal atoms result in an averaged value of 0.21 W/(mK), which is significantly higher than anything obtained during the mass-scalings in section 5.3.1, where the highest value reached 0.12 W/(mK). When loosely analyzing the low frequency phonon bands in figure 5.4, one can see, that the acoustic bands show a higher dispersion in some directions, which leads to a higher group velocity. In general, there appear to be a lot fewer low lying flat bands, which were mostly modes corresponding to torsional/translational motions of the organic linkers. For a more precise analysis of the phonons in IRMOF-130, as observed with the force field, see section 5.4.

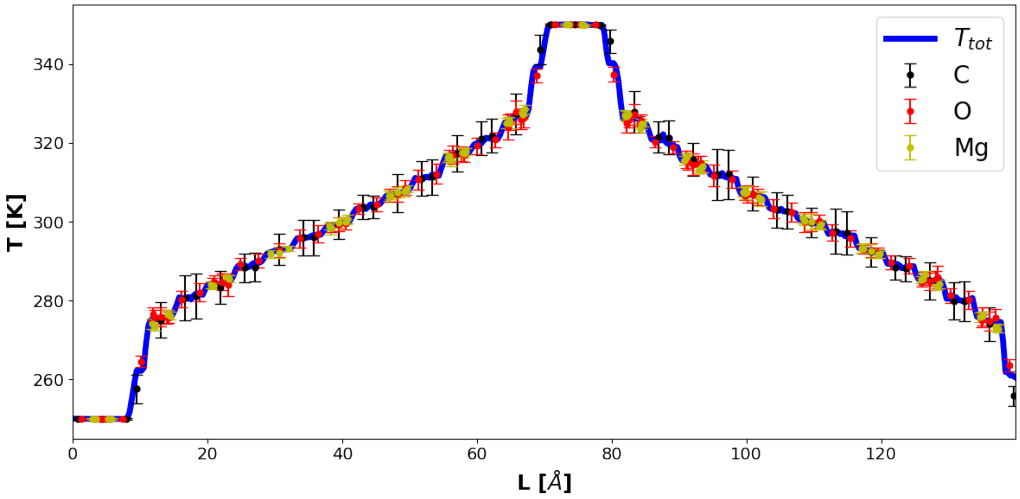


Figure 5.23: Temperature profile of a 8x2x2 supercell of IRMOF-130 (Mg) during a NEMD simulation at 300 K. The errorbars show the spread of the atomic temperatures.

### 5.3.4 MOFs with different architecture

In addition to the findings in section 5.3.2 it would be interesting to analyze how different kind of MOF structures and connecting chemistry lead to different trends than compared to the IRMOFs. The systems of interest are zinc based paddlewheel MOFs. They are chosen due to their tetragonal structure and their inherent anisotropy which allows a comparison to the previously observed hypothetical non-isoreticular MOFs. Another reason is the completely different connecting chemistry in one of the three main directions, allowing further analysis on the impact of the linker-node interfaces. In addition to this, the thermal conductivity of MOF-74 was studied in order to observe the impact of completely different architectures.

Thermal conductivity values at 300 K for MOF-508, JAST-1 and MOF-74 can be found in table 5.5. Figure 5.24 visualizes these values with the structure as a reference. The values were obtained using the Green-Kubo method for supercells as specified in the table. Especially interesting is that MOF-508 shows inconsistent anisotropic behavior compared to the MOFs studied in section 5.3.2. Here the higher thermal transport value can be found in

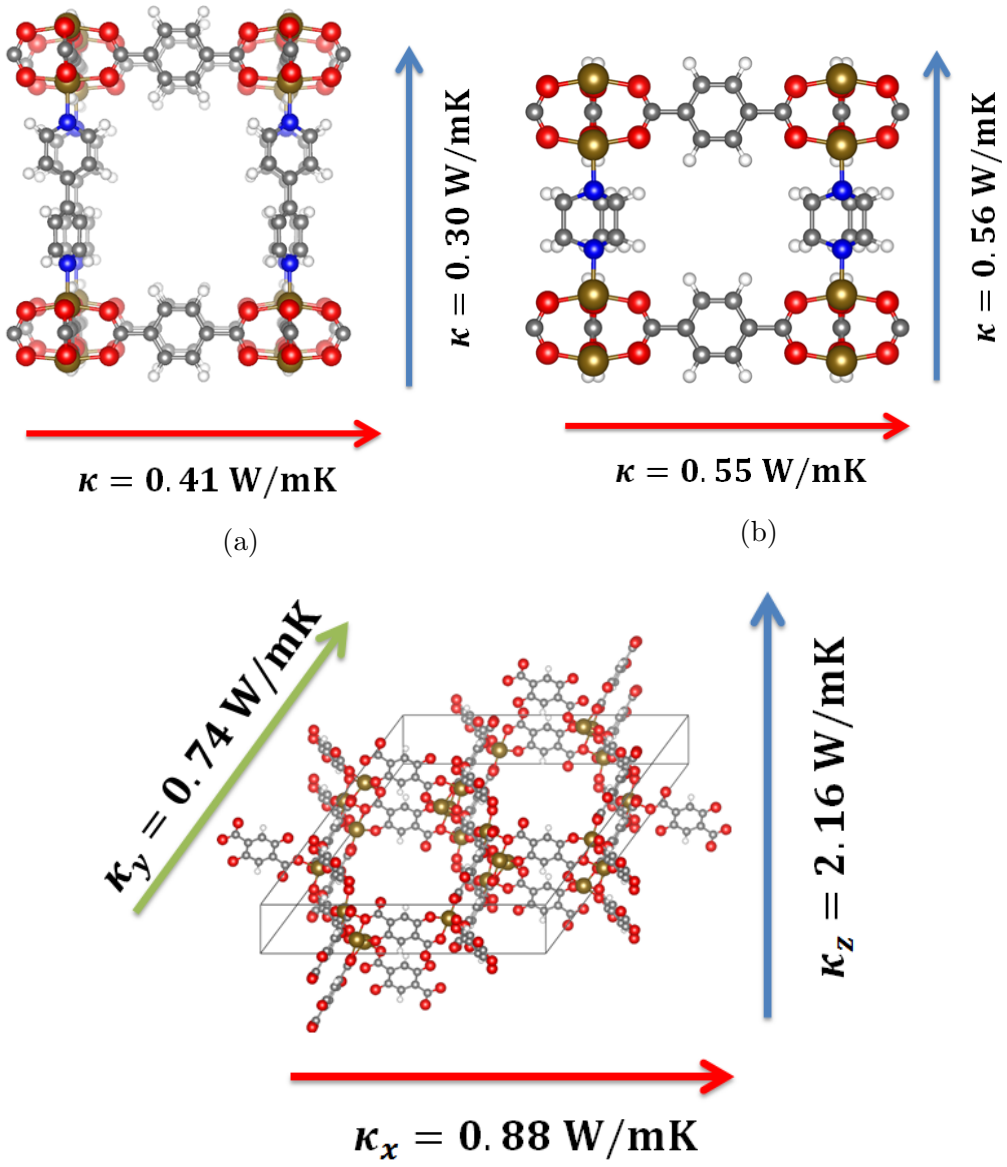


Figure 5.24: Anisotropic thermal conductivities for MOF-508 (a), JAST-1 (b) and MOF-74 (c) obtained with equilibrium molecular dynamics simulations. Here, red is oxygen, grey is carbon, white is hydrogen, blue is nitrogen and golden is zinc.

Table 5.5: Anisotropic thermal conductivity of MOF-508, JAST-1 and MOF-74 obtained with the Green-Kubo method. The pyridine and DABCO linkers as well as the node-chain in MOF-74 face the $z$ direction. Thermal conductivity values are given in W/(mK)

| **System** | $\kappa_{\mathbf{x}}$ | $\kappa_{\mathbf{y}}$ | $\kappa_{\mathbf{z}}$ | **supercell** |
|---|---|---|---|---|
| MOF-508 | 0.42 | 0.40 | 0.30 | 4x4x4 |
| JAST-1 | 0.59 | 0.53 | 0.56 | 4x4x4 |
| MOF-74 | 0.74 | 0.88 | 2.16 | 4x4x8 (conv) |

the direction of the shorter linkers with lower cross-sectional linker density. This indicates that the metal-nitrogen connection between node and linker provides a larger thermal resistivity than the one originating from the carboxylic acid connector. In the directions of the therepthalic acid linkers, the thermal conductivity is slightly higher than in IRMOF-1, even though the cross-sectional linker density is only slightly higher. This can be attributed to the lighter inorganic paddlewheel node reducing the mass difference with the organic linker.
JAST-1 shows almost isotropic thermal conductivity. The linker density is now higher in $x$ and $y$ directions leading to a larger value. In $z$ direction, the DABCO linker seems to provide a better linker-node interface than the bipyridine, leading to a significantly higher thermal conductivity while preserving linker density. This arises due to the different hybridization of the nitrogen atom for both of these linkers. When comparing the phonon bands in figures 5.7 and 5.5 a higher dispersion of the acoustic modes can be seen for JAST-1 in all high-symmetry directions. Since these modes are typically the main carriers of heat, the higher thermal conductivity is expected.
MOF-74 shows the largest thermal conductivity values of any MOF investigated in this work. Especially along the node-chain the thermal conductivity gets very high with 2.16 W/(mK). This is not very surprising, considering that there are no organic-inorganic interfaces in this direction and thermal transport essentially happens along zinc oxide nanowires. In the other directions the rigid nature of this MOF makes isolated motions of organic linkers difficult. This leads to more vibrations of all components in the material, which are more relevant for thermal transport. But it is difficult to compare the numerical value with other MOFs due to the completely different hexag-

onal structure. Further analysis for thermal transport in this system will be carried out with anharmonic lattice dynamics results in section 5.4.2.

## 5.4 Thermal properties based on Lattice Dynamics

In addition to the molecular dynamics approaches, the thermal conductivity has also been calculated using the Boltzmann transport equation, which is solved using the relaxation time approximation. The required lifetimes were obtained by calculating third order force constants with the finite difference approach. All calculations of displacements have been carried out with the parameterized force fields.

### 5.4.1 IRMOF-130

The phonons in IRMOF-130 have been converged with the supercell approach using a 3x3x3 supercell of the primitive unit cell. For the third order force constants, the same cell was used. It has been shown before that the third order force constants converge faster than the second order with respect to cell size. This is why no larger cells have been considered. The phonon lifetimes have been calculated for temperatures ranging from 50 to 1000 K on an 7x7x7 grid of wave vectors. The temperature dependent thermal conductivity resulting from this calculation can be seen in figure 5.25. At a temperature of 300 K the thermal conductivity amounts to 0.241 W/(mK). This is lower than the values obtained from MD methods by more than a factor of 4. The values obtained with DFTB using the BTE-RTA approach, that were carried out by Tomas Kamencek (see appendix A), are slightly higher than the force-field produced values, but still significantly smaller than the MD results. There are several possible reasons for this discrepancy, which will be discussed in detail in this section.

A possibility for the large mismatch are the anharmonicities. The lattice dynamics calculations only considered up to three-phonon processes. It is possible that higher order force constants are required to converge the thermal conductivity and has been observed in other materials before [87]. The molecular dynamics simulations would include all anharmonic effects in a single simulation. But including higher order anharmonicity terms should increase the number of scattering processes and in turn reduce the thermal conductivity. Therefore, this is unlikely to be the cause for the discrepancy between the methods. There also might be an issue with the anharmonicities included in the force field. But it is difficult to assess the accuracy of the anharmonicities due to a lack of reference data.
From the perspective of molecular dynamics simulations one problem could

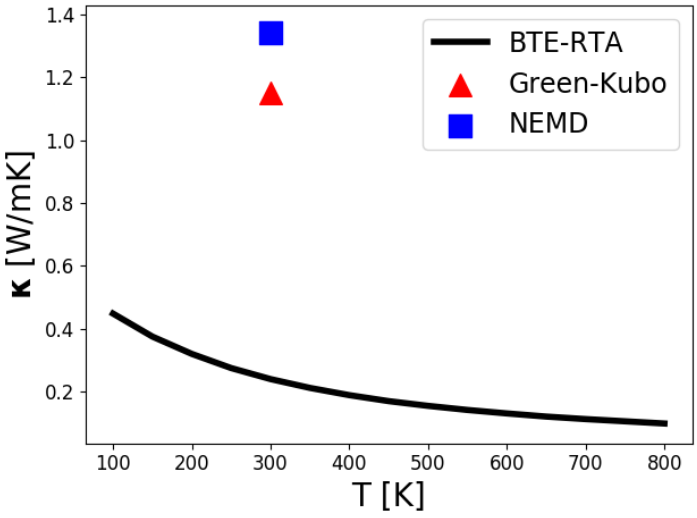


Figure 5.25: Thermal conductivity of IRMOF-130 calculated with the Boltzmann Transport equation using the relaxation time approximation (BTE-RTA) on an 7x7x7 q-mesh, the Green-Kubo method and Non-equilibrium molecular dynamics (NEMD).

be that the simulation was performed in the classical limit. But since mostly low frequency modes contribute significantly to the thermal conductivity this probably will not cause a discrepancy this large. Figure 5.26a shows the frequency dependent evolution of the thermal conductivity for IRMOF-130 at 300 K. And in figure 5.26b one can see the frequency dependent saturation temperature of the heat capacity. It can be seen that the thermal conductivity is already at its converged value when only considering the first 15-20 THz. And the contribution of these low frequencies up to 15 THz to the heat capacity is already saturated at the temperature range of interest. While there is still a small contribution that is not properly described in the classical limit yet, this contribution is relatively small. An interesting observation that can be made nonetheless is that higher lying optical modes have to carry a significant amount of heat in IRMOF-130. In the band structure in figure 5.4 one can see that the acoustic modes only reach up to about 3 THz. At this frequency the cumulative thermal conductivity has not even reached a fourth of its converged value. While it is not possible to find a proper reason for the poor agreement between the methods, the individual

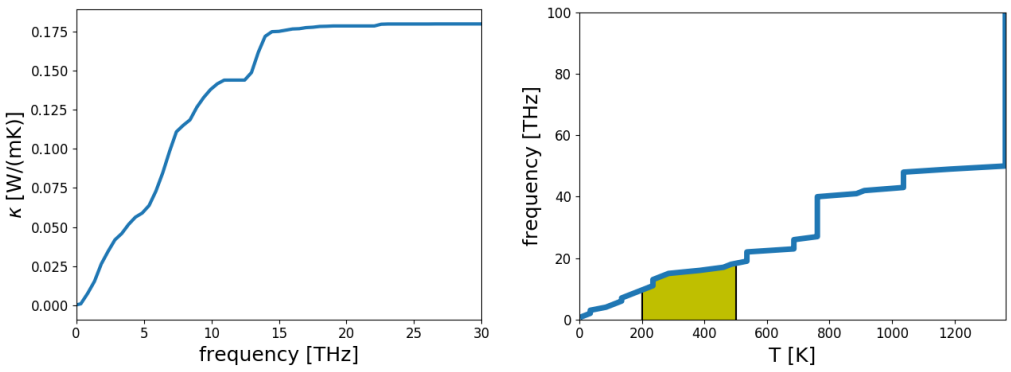


(a) (b)

Figure 5.26: (a) Cumulative thermal conductivity of IRMOF-130 depending on frequency based on the third order force constants and (b) temperatures at which the heat capacity reaches its saturated value when only considering modes up to a certain frequency. The yellow area indicates the temperature range for which molecular dynamics simulations have been performed.

components of the thermal conductivity of IRMOF-130 will still be investigated. In figure 5.27a the temperature dependent heat capacity is visualized, while figure 5.27b contains the group velocities of IRMOF-130 calculated on a 20x20x20 q-mesh. In the group velocities one can see an arch-like structure on many places. This arises due to the trend of the slope of individual phonon bands. It also becomes clear that the lowest frequencies show the highest group velocities but all frequencies up to 20 THz show significant contributions. Beyond this, the bands are relatively flat and show low group velocities, as expected for higher frequency localized vibrations.

The third component of the thermal conductivity, the phonon lifetimes, are visualized in figure 5.28. As opposed to the group velocities, some very high relaxation times can be seen in the high frequency region. But since the square of the group velocity enters the BTE, these flat bands still do not carry any significant contributions to the thermal conductivity. In the low frequency region up to 20 THz that actually does matter, no clear trends can be observed. The two discernible modes with large phonon lifetimes at about 3 THz are rotations of the oxalic acid linkers while the inorganic nodes remain stationary. But since these bands are relatively flat, they will also not contribute excessively to the thermal conductivity. As was discussed in

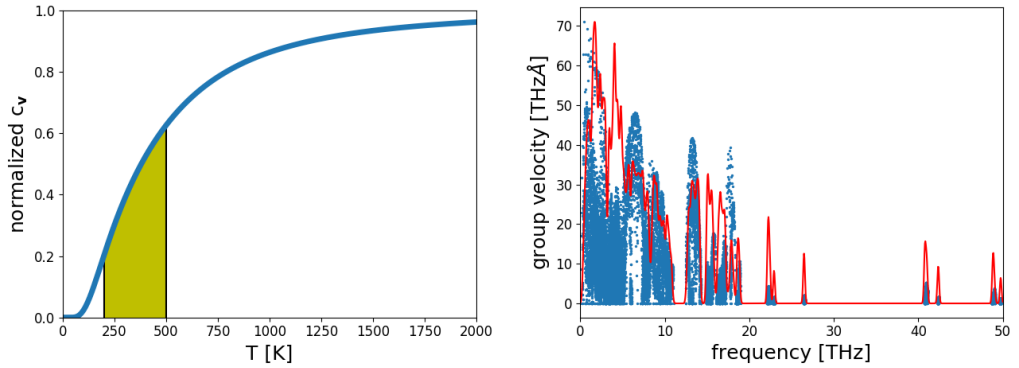


(a) (b)

Figure 5.27: (a) Heat capacity of IRMOF-130 (Mg); the temperature range of interest is indicated by the yellow area; and (b) Group velocities of IRMOF-130 sampled over a 20x20x20 q-mesh in the first Brillouin zone. The red curve represents a sum over normal distributions around all frequencies with a standard deviation of $\sigma = 0.1$ THz weighted with the respective group velocity. This group velocity density distribution is normalized to the maximum group velocity for visibility.

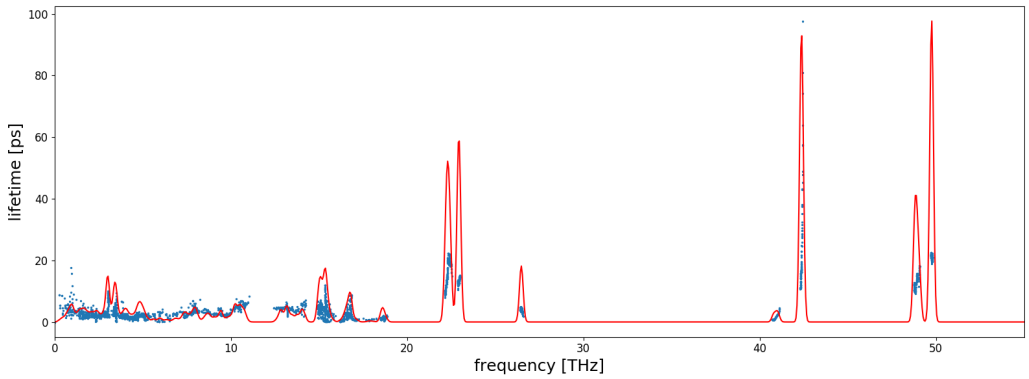


Figure 5.28: Phonon relaxation times of IRMOF-130 sampled on an 7x7x7 mesh in the first Brillouin Zone. The red curve represents a sum over normal distributions around all frequencies with a standard deviation of $\sigma = 0.1$ THz weighted with the respective lifetime. This group velocity density distribution is normalized to the maximum lifetime for visibility.

the previous sections, this method allows further analysis of the per-mode contribution to the thermal conductivity. This has been investigated for q-vectors on the 7x7x7 mesh that coincide with face-centered-cubic high-symmetry directions. The thermal conductivity for each mode $\kappa_{\mathbf{q}i,j}$ is defined as

$$\kappa_{tot,j} = \frac{1}{n} \sum_{\mathbf{q}} \sum_{i} \kappa_{\mathbf{q}i,j}, \tag{5.3}$$

where $n$ is the number of grid points, $i$ are the band indices and $j$ is the element index of the thermal conductivity tensor. These values have been visualized in figure 5.29 using the phonon band structure as a reference. It is easy to see that there are large differences in the contributions of each mode. Unsurprisingly, the high dispersion acoustic modes show the largest contributions. Most of the flat bands, that are typically isolated motions of the linkers or nodes, show very low thermal conductivity values. There is also a strongly contributing band ranging from 6 THz at $X$ to 7.8 THz at $\Gamma$. Its influence can be seen in figure 5.26a, where a steeper slope follows in this frequency range. The highest frequency mode significantly contributing to the thermal conductivity occurs in a range from 13 to 14 THz. Both of these motions have been visualized at $\Gamma$ point in figure 5.30. Both of them show a stretching motion of the organic linker relative to the inorganic nodes. It should be stated, that this latter group of modes is also fully included in molecular dynamics at the temperatures of interest, even though they might not be fully occupied in reality, as can be seen in figure 5.26b.

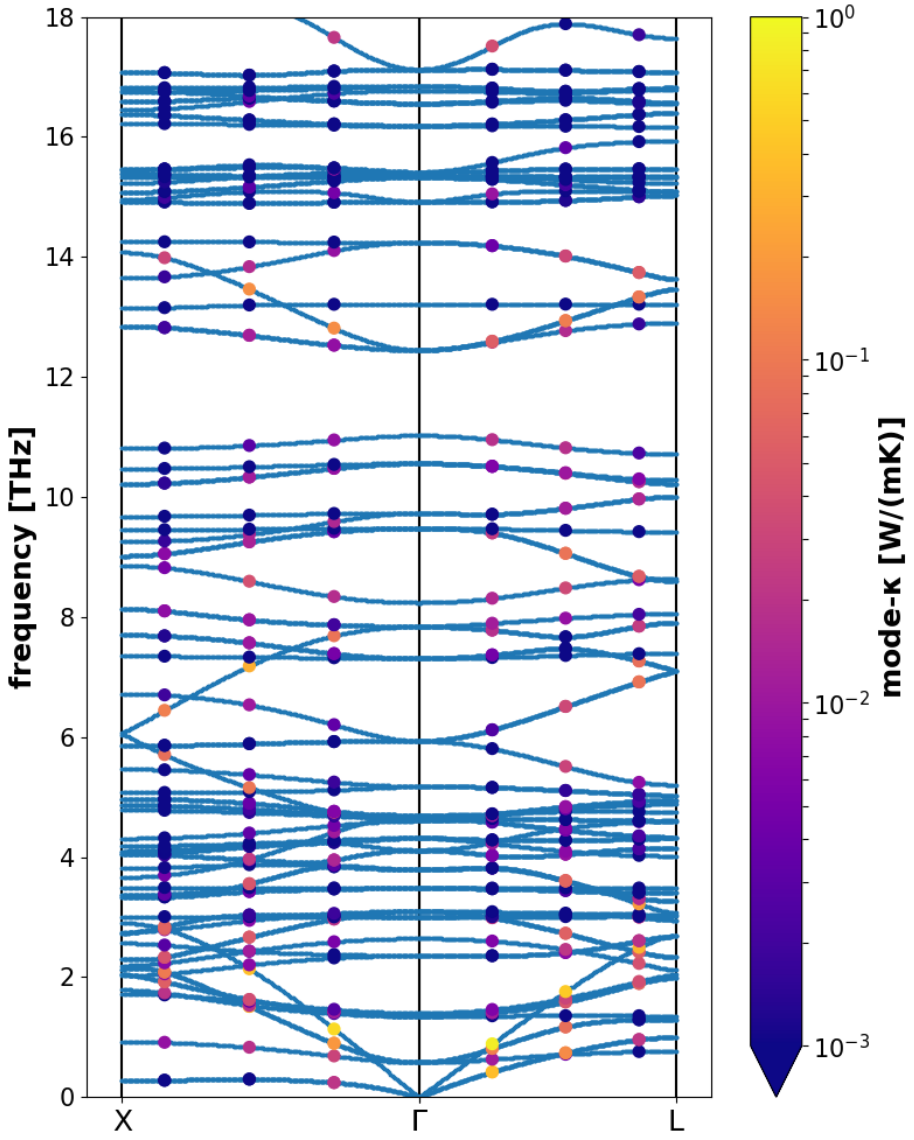


Figure 5.29: Per-mode thermal conductivities calculated for q-vectors in a 7x7x7 grid that coincide with the high symmetry lines in IRMOF-130 (Mg).

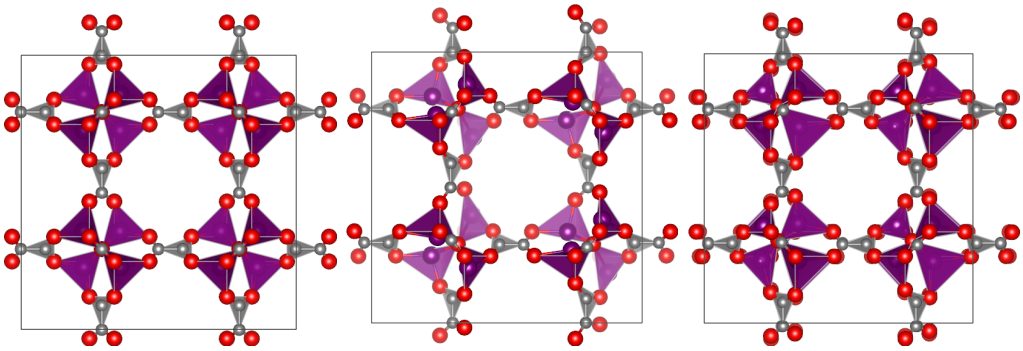

(a) Idle structure for reference (b) Γ point phonon at 7.84 THz (c) Γ point phonon at 12.44 THz

Figure 5.30: Γ point motions of the same symmetry of selected optical modes that carry significant contributions to the thermal conductivity in IRMOF-130 (Mg). The Γ point modes have been visualized instead of the corresponding off-Γ modes for easier interpretation.

### 5.4.2 MOF-74

The third order force constants have also been calculated for MOF-74 in order to investigate its thermal conductivity. Note, that this was carried out previously using density functional tight-binding by Wang et al. [88]. But only a relatively small supercell was used to converge the force constants. The thermal conductivity obtained in [88] was significantly lower than the results provided by MD outlined in section 5.3.4. The values amounted to 0.44 W/(mK) in plane of the hexagonal structure and to 0.68 W/(mK) in stacking direction at 300 K.
The same calculation, without a force cutoff and by using a 2x2x2 supercell was carried out with the DFT obtained force-field. Like for IRMOF-130 the thermal conductivity was evaluated on a 7x7x7 q-grid in the first Brillouin zone. Since none of the alternative ways to obtain the thermal conductivity mentioned in section 5.4.1 yielded any meaningful improvements, the BTE is only solved under the relaxation time approximation. Figure 5.31 shows the thermal conductivity of this system compared to the values obtained with molecular dynamics. In addition to this an alternative evaluation of the BTE with DFTB carried out by Tomas Kamencek, without cutoffs, has been included for reference. From this, at 300 K, the value for $\kappa_{xx}$ amounts to 1.39 W/(mK) and $\kappa_{zz}$ to 3.18 W/(mK). It is obvious that the values obtained

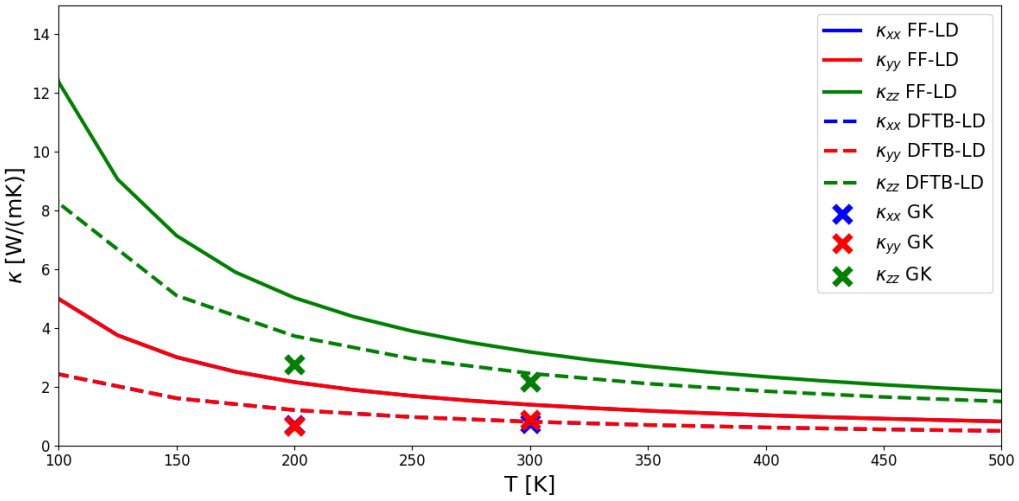


Figure 5.31: Thermal conductivity of MOF-74 (Zn) calculated with the Boltzmann Transport equation using the relaxation time approximation (BTE-RTA) on an 7x7x7 q-mesh and the Green-Kubo method.

with MD and the BTE are both significantly higher than those obtained by Wang et al. The force-field using the lattice dynamics approach appears to overestimate the thermal conductivity compared to the alternative DFTB results. But even those are much higher than what was predicted previously. At room temperature the Green-Kubo results are in pretty good agreement with the data in DFTB. At 200 K the thermal conductivity is significantly underestimated by MD. This discrepancy between MD and LD might arise due to many-phonon scattering effects reducing the thermal conductivity.
Now it is important to investigate the components of the thermal conductivity in more detail. One important objective is to understand why agreement between the methods is much better for MOF-74 than for IRMOF-130. Figure 5.32a shows the cumulative thermal conductivity over the entire frequency range. It can be clearly seen, that only the very low frequency region up to about 5 THz contains modes important for the thermal conductivity. This makes it fairly unlikely that the discrepancy between BTE-RTA and MD arises due to low temperature effects. Because as can be seen in the heat capacity saturation temperatures in figure 5.32b, these low energy modes should be included even at 200 K.

The phonon lifetimes are depicted in figure 5.33a and here a stark con-

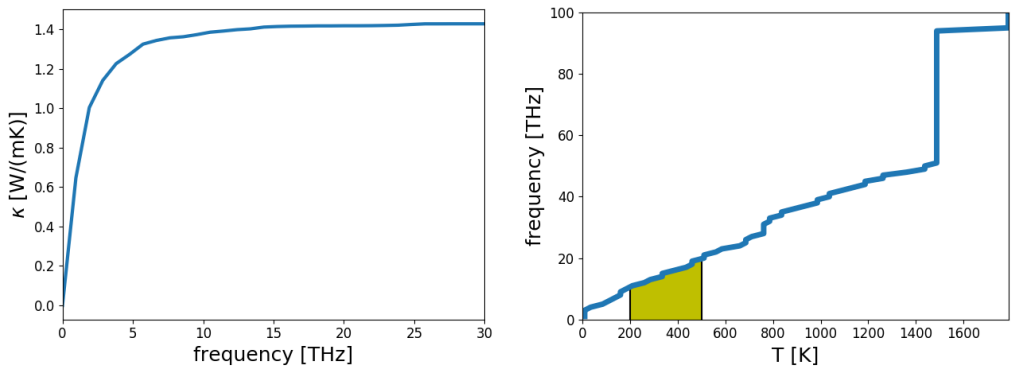


(a) (b)

Figure 5.32: (a) Cumulative thermal conductivity of MOF-74 (Zn) depending on frequency based on the third order force constants and (b) temperatures at which the heat capacity reaches its saturated value when only considering modes up to a certain frequency. The yellow area indicates the temperature range for which molecular dynamics simulations have been performed.

trast compared to IRMOF-130 can be seen. Here, only the lowest frequency modes show significant lifetimes. Numerically those are much higher, than any that could be observed in IRMOF-130. Some of them even reach 1000 ps and more. But these are low in number and do not show dominating contributions towards thermal transport. But since these were not shown in the DFTB results, it is very likely that this is responsible for the differences in thermal conductivity between the two levels of theory. This lifetime distribution implies that acoustic modes carry the vast majority of heat and that optical modes at higher frequencies are relatively unimportant. This situation can be observed for many inorganic materials. When looking at the group velocities in figure 5.33b we can also see that the lowest frequency modes carry the highest significance, but most modes up to about 20 THz could still contribute significantly given a high enough lifetime.

For MOF-74 the mode-thermal conductivity has also been evaluated along certain band paths and is shown in figure 5.34. Note, that $\Gamma - X$ is not a high symmetry line for this lattice explaining the lack of values in this directions. In general, this plot confirms that only the low frequency modes are important. But it also is clear that optical as well as acoustic modes con-

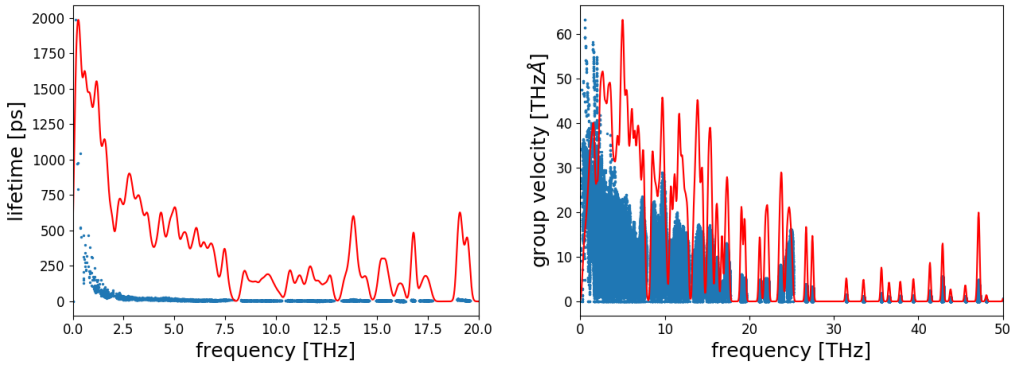


(a) (b)

Figure 5.33: (a) Phonon life times of MOF-74 (Zn) at 300 K sampled over a 7x7x7 mesh; and (b) Group velocities of MOF-74 (Zn) sampled over a 20x20x20 q-mesh in the first Brillouin zone. The red curve represents a sum over normal distributions around all frequencies with a standard deviation of $\sigma = 0.1$ THz weighted with the respective group velocity or lifetime. This density distribution is normalized to the maximum shown value for visibility.

tribute significantly in the low frequency range. These vibrations all include joint motions of both, linker and nodes. There are no isolated motions of the organic component in the low frequency region, which were those that did not contribute significantly in IRMOF-130. This leads to the continuous decay of the lifetimes with no remarkable outliers.

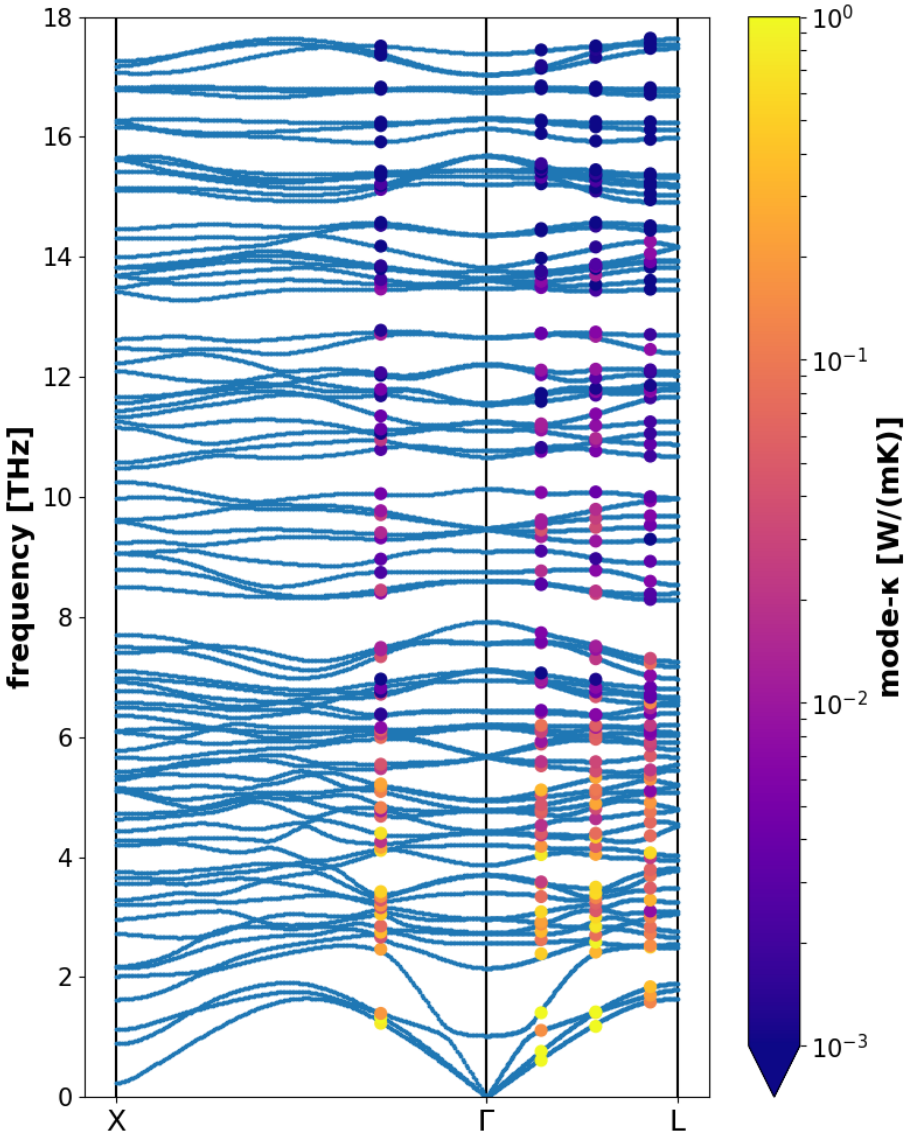


Figure 5.34: Per-mode thermal conductivities calculated for q-vectors in a 7x7x7 grid that coincide with band paths in MOF-74 (Zn).

# 6 Summary

Thermal transport properties in metal-organic frameworks (MOFs) have been investigated by means of molecular dynamics simulations utilizing classical force-fields. For this equilibrium- and non-equilibrium approaches were applied. Applications of MOFs are frequently reliant on heat dissipation, and these materials are known for their low thermal conductivity. This leads to heat transport playing a crucial role for the effectiveness of heat transport. The materials allow for easy modification and tailoring of properties to the desired applications. This is due to the modular nature of the organic and inorganic building units. This made it interesting to investigate the thermal conductivity in MOFs with a structure-to-property approach. Over the course of this investigation, additional classical force-fields had to be fit in order to carry out the simulations. Additionally, thermal expansion occurring in the analyzed materials has been discussed.
For the investigation over the course of this work, the impact of exchanging the node and linker was a major focus. Beginning with a well known material, IRMOF-1, also known as MOF-5, the thermal conductivity was explored. On one hand, the focus was to change the metals in the inorganic metal-oxide nodes. This was achieved by scaling the masses of the metals appropriately to emulate a different metal. For one of these, with magnesium as metal atom, specialized force-fields, based on DFT reference data, have been obtained to include other effects than the mass. In terms of thermal conductivity, no noteworthy differences have been observed. The different masses lead to a increase in thermal conductivity, by up to a factor of two, when the metals are lighter. For higher masses a lower value was obtained. Inversely, when the masses of the carbon and hydrogen atoms were scaled, the thermal conductivity barely changed. This would be similar to what would happen, when the aromatic linkers included functional groups. The reason for this behavior was investigated by observing temperature profiles obtained during non-equilibrium molecular dynamics simulations. Here a clear barrier of thermal transport between each node and linker could be observed. This leads to the assumption, that the large difference in masses between dissimilar components of the system might be the cause for low thermal transport. A large difference would imply, that the phonons on both sides show little overlap, leading to poor propagation and an increase in scattering processes. When this mass ratio was reduced, the barrier would grow weaker and vice versa. For the case of increased linker masses this should lead to a reduced

thermal resistivity across the interface. But since increasing masses of atoms inherently reduces thermal conductivity, this leads to a cancellation of both effects. For the heavier inorganic nodes, both of these considerations lead to an increase in thermal conductivity for lower masses, leading to an effect, much larger than initially anticipated. This hypothesis has mostly been confirmed by evaluating the thermal conductivity across the interface in NEMD simulations. It showed an increase for reduced metal masses and increased organic masses, while a reduction was obtained for higher metal masses and lower organic masses.

It was also of interest to investigate the impact of different lengths of organic linkers compared to IRMOF-1. For this biphenyl-dicarboxylic acid and terphenyl-dicarboxylic acid linkers replaced the terphthalic acid linkers of IRMOF-1, forming IRMOF-10 and IRMOF-16. This avoids the introduction of additional chemical connectors as much as possible, while still being realistic materials. A steep decrease in thermal conductivity for longer linkers could be observed. However, this is not due to linker length, but arises from the reduced density of linkers capable of carrying heat. This was shown by simulating anisotropic MOFs with the same linker density but a different linker length in one direction. The thermal conductivity in direction of the same cross-sectional linker density only varied within the error. In tandem with this, a previously proposed linear dependence of thermal transport on pore-size was observed. Based on the available data, the thermal conductivity decreased with increasing pore size in a linear manner, but the errors were relatively large.

An additional objective was to investigate phonon calculations via lattice dynamics utilizing force-fields. The primary purpose was to validate the lower level of theory by comparing the results to density-functional based data. But the phonons also provided insights on heat transport and thermal expansion of MOFs. Therefore, phonon bands have been obtained for almost all materials investigated in this work. Agreement of phonon frequency was analyzed based on IRMOF-1 (Zn) between a DFT reference and the MOF-FF force field. Also the DFT vibrational data for some materials, that were not originally included in MOF-FF, served as a reference for fitting additional force-fields. The comparisons indicated acceptable deviations in terms of vibrational frequencies. An additional IRMOF, the IRMOF-130 (Mg) with only oxalic acid as a linker, was included to provide a smaller system, where reference data for higher level of theory can be obtained. For this the thermal conductivity was not only evaluated using molecular dynamics, but

also lattice dynamics. This was achieved by calculating the third order force-constants to include scattering processes. Agreement of the resulting thermal conductivity obtained from lattice dynamics using density-functional tight binding (DFTB) was reasonable. But the thermal conductivity calculated from molecular dynamics simulations was higher by a factor of five. Possible reasons were discussed for this large discrepancy, but none of them could be identified to be the main cause.

In order to investigate different types of node-linker interfaces, MOFs with different architecture were chosen to complement the IRMOFs. The thermal conductivity of JAST-1 and MOF-508 was calculated using molecular dynamics. These are tetragonal MOFs and consist of a paddlewheel node and terephthalic acid linkers in two Cartesian directions, as well as an organic linker connecting to the metal atoms via a nitrogen atom, in the third direction. In case of JAST-1, this is a DABCO linker, and for MOF-508 a bipyridine linker. In direction of terephthalic acid linkers, the chemistry is relatively similar to the IRMOFs, and the resulting thermal conductivities, were only slightly higher than what would be expected for a MOF with this cross-sectional linker density. This was explained by the lighter mass of the paddlewheel nodes, reducing phonon mismatch. In direction of the metal-nitrogen bonds, the thermal conductivity differed strongly depending on chemistry. For JAST-1 it was similar to the terephthalic acid linkers, while MOF-508 showed a significantly reduced thermal conductivity for the same cross-sectional linker density.

Another material investigated was the MOF-74, a hexagonal MOF based on infinitely elongated strands of metal-oxide connected by aromatic linkers. This was done in order to investigate a completely different architecture. The thermal conductivity based on molecular dynamics was much higher in direction of the linker-strands than in any other MOF investigated. The very large differences between this materials and the other MOFs investigated in this work, made a direct comparison difficult. Therefore, the phonons were analyzed in more detail. The third order force-constants were calculated with lattice dynamics using the force field. Resulting thermal conductivity values agree reasonably well with the molecular dynamics results. Evaluation of the phonon relaxation times showed a very quick and steady decay in the low frequency region. No frequency modes beyond 10 THz appear to be important for thermal conductivity. This is due to the much more rigid nature of the material. The remaining discrepancy between molecular and lattice dynamics in this case could be explained by many-phonon scattering

processes arising due to anharmonicities.

Thermal expansion coefficients were calculated for most investigated MOFs. The $Zn_4O$ MOFs, which include all IRMOFs as well as their anisotropic counterparts, were determined to be negative. The paddlewheel MOFs investigated in this thesis, JAST-1 and MOF-508, showed a negative thermal expansion coefficient in hte directions of the therephthalic acid linkers and a positive thermal expansion coefficient in direction of the nitrogen based linkers. MOF-74 showed positive thermal expansion in all directions. Possible reasons for the unusual thermal contraction in these MOFs were discussed and there were strong indications of specific bending motions of the organic linkers being the main cause.

# References

[1] J. L. Rowsell and O. M. Yaghi, "Strategies for hydrogen storage in metal-organic frameworks," *Angewandte Chemie - International Edition*, vol. 44, no. 30, pp. 4670–4679, 2005.

[2] A. R. Millward and O. M. Yaghi, "Metal-organic frameworks with exceptionally high capacity for storage of carbon dioxide at room temperature," *Journal of the American Chemical Society*, vol. 127, no. 51, pp. 17998–17999, 2005.

[3] L. Zou and H. C. Zhou, "Hydrogen storage in metal-organic frameworks," *Nanostructured Materials for Next-Generation Energy Storage and Conversion: Hydrogen Production, Storage, and Utilization*, no. 5, pp. 143–170, 2017.

[4] J. R. Li, R. J. Kuppler, and H. C. Zhou, "Selective gas adsorption and separation in metal-organic frameworks," *Chemical Society Reviews*, vol. 38, no. 5, pp. 1477–1504, 2009.

[5] D. Britt, H. Furukawa, B. Wang, T. G. Glover, and O. M. Yaghi, "Highly efficient separation of carbon dioxide by a metal-organic framework replete with open metal sites," *Proceedings of the National Academy of Sciences*, vol. 106, no. 49, pp. 20637–20640, 2009.

[6] P. Horcajada, C. Serre, M. Vallet-Regí, M. Sebban, F. Taulelle, and G. Férey, "Metal-organic frameworks as efficient materials for drug delivery," *Angewandte Chemie - International Edition*, vol. 45, no. 36, pp. 5974–5978, 2006.

[7] J. Lee, O. K. Farha, J. Roberts, K. A. Scheidt, S. T. Nguyen, and J. T. Hupp, "Metal-organic framework materials as catalysts," *Chemical Society Reviews*, vol. 38, no. 5, pp. 1450–1459, 2009.

[8] L. Sun, B. Liao, D. Sheberla, D. Kraemer, J. Zhou, E. A. Stach, D. Zakharov, V. Stavila, A. A. Talin, Y. Ge, M. D. Allendorf, G. Chen, F. Léonard, and M. Dinc, "A Microporous and Naturally Nanostructured Thermoelectric Metal-Organic Framework with Ultralow Thermal Conductivity," *Joule*, vol. 1, no. 1, pp. 168–177, 2017.

[9] K. J. Erickson, F. Léonard, V. Stavila, M. E. Foster, C. D. Spataru, R. E. Jones, B. M. Foley, P. E. Hopkins, M. D. Allendorf, and A. A. Talin, "Thin film thermoelectric metal-organic framework with high seebeck coefficient and low thermal conductivity," *Advanced Materials*, vol. 27, no. 22, pp. 3453–3459, 2015.

[10] G. Wu, J. Huang, Y. Zang, J. He, and G. Xu, "Porous field-effect transistors based on a semiconductive metal-organic framework," *Journal of the American Chemical Society*, vol. 139, no. 4, pp. 1360–1363, 2017.

[11] D. Sheberla, L. Sun, M. A. Blood-Forsythe, S. Er, C. R. Wade, C. K. Brozek, A. Aspuru-Guzik, and M. Dinc, "High electrical conductivity in Ni3(2,3,6,7,10,11- hexaiminotriphenylene)2, a semiconducting metal-organic graphene analogue," *Journal of the American Chemical Society*, vol. 136, no. 25, pp. 8859–8862, 2014.

[12] D. W. Fu, W. Zhang, and R. G. Xiong, "The first metal-organic framework (MOF) of Imazethapyr and its SHG, piezoelectric and ferroelectric properties," *Dalton Transactions*, no. 30, pp. 3946–3948, 2008.

[13] W. Zhang and R. G. Xiong, "Ferroelectric metal-organic frameworks," *Chemical Reviews*, vol. 112, no. 2, pp. 1163–1195, 2012.

[14] M. Kurmoo, "Magnetic metal-organic frameworks," *Chemical Society Reviews*, vol. 38, no. 5, pp. 1353–1379, 2009.

[15] X. Zhang, Y. Zhou, B. Cui, M. Zhao, and F. Liu, "Theoretical Discovery of a Superconducting Two-Dimensional Metal-Organic Framework," *Nano Letters*, vol. 17, no. 10, pp. 6166–6170, 2017.

[16] J. Zhang, T. S. Fisher, P. V. Ramachandran, J. P. Gore, and I. Mudawar, "A Review of Heat Transfer Issues in Hydrogen Storage Technologies," *Journal of Heat Transfer*, vol. 127, no. 12, p. 1391, 2005.

[17] H. G. T. Nguyen, N. M. Schweitzer, C. Y. Chang, T. L. Drake, M. C. So, P. C. Stair, O. K. Farha, J. T. Hupp, and S. T. Nguyen, "Vanadium-node-functionalized UiO-66: A thermally stable MOF-supported catalyst for the gas-phase oxidative dehydrogenation of cyclohexene," *ACS Catalysis*, vol. 4, no. 8, pp. 2496–2500, 2014.

[18] B. L. Huang, Z. Ni, A. Millward, A. J. H. McGaughey, C. Uher, M. Kaviany, and O. Yaghi, "Thermal conductivity of a metal-organic framework (MOF-5): Part II. Measurement," *International Journal of Heat and Mass Transfer*, vol. 50, no. 3-4, pp. 405–411, 2007.

[19] P. K. Schelling, S. R. Phillpot, and P. Keblinski, "Comparison of atomic-level simulation methods for computing thermal conductivity," *Physical Review B - Condensed Matter and Materials Physics*, vol. 65, no. 14, pp. 1–12, 2002.

[20] K. Momma and F. Izumi, "*VESTA3* for three-dimensional visualization of crystal, volumetric and morphology data," *Journal of Applied Crystallography*, vol. 44, pp. 1272–1276, Dec 2011.

[21] Y. C. L. Z. V. F. CHAEMCHUEN Somboon, ZHOU Kui, "Alkali-metal tuning of adsorption sites in metal organic frameworks mof-5 for carbon dioxide/methane separation at ambient conditions," *Chinese Journal of Applied Chemistry*, vol. 32, no. 5, p. 552, 2015.

[22] L. Han, M. Budge, and P. Alex Greaney, "Relationship between thermal conductivity and framework architecture in MOF-5," *Computational Materials Science*, vol. 94, no. C, pp. 292–297, 2014.

[23] W. Y. Gao, W. Yan, R. Cai, K. Williams, A. Salas, L. Wojtas, X. Shi, and S. Ma, "A pillared metal-organic framework incorporated with 1,2,3-triazole moieties exhibiting remarkable enhancement of CO 2 uptake," *Chemical Communications*, vol. 48, no. 71, pp. 8898–8900, 2012.

[24] S. Horike, S. Shimomura, and S. Kitagawa, "Soft porous crystals," *Nature Chemistry*, vol. 1, no. 9, pp. 695–704, 2009.

[25] G. A. Slack, "Nonmetallic crystals with high thermal conductivity," *J. Phys. Chem. Solids*, vol. 34, pp. 321–335, 1973.

[26] A. A. Talin, A. C. Ford, M. E. Foster, V. Stavila, F. El Gabaly, F. Léonard, M. D. Allendorf, A. Centrone, P. Haney, R. A. Kinney, V. Szalai, and H. P. Yoon, "Tunable electrical conductivity in metal-organic framework thin-film devices," *Science*, vol. 343, no. 6166, pp. 66–69, 2014.

[27] H. Ibach and H. Lüth, *Festkörperphysik: Einführung in die Grundlagen*. Springer-Lehrbuch, Springer Berlin Heidelberg, 2009.

[28] A. Togo, L. Chaput, and I. Tanaka, "Distributions of phonon lifetimes in Brillouin zones," *Physical Review B - Condensed Matter and Materials Physics*, vol. 91, no. 9, 2015.

[29] A. Maradudin and A. Fein, "Scattering of Neutrons by an Anharnmnic," *Physical Review*, vol. 128, no. 6, p. 2589, 1962.

[30] A. H. MacDonald, S. H. Vosko, and C. P. T., "Extensions of the tetrahedron method for evaluating spectral properties of solids," *Journal of Physics C: Solid State Physics*, vol. 12, no. 15, pp. 2991–3002, 1979.

[31] P. Procacci, G. F. Signorini, and R. G. Della Valle, "Efficient calculation of high-order self-energy corrections to phonon linewidths: Application to $\alpha$-nitrogen," *Phys. Rev. B*, vol. 47, pp. 11124–11133, May 1993.

[32] T. Feng, L. Lindsay, and X. Ruan, "Four-phonon scattering significantly reduces intrinsic thermal conductivity of solids," *Physical Review B*, vol. 96, no. 16, pp. 1–6, 2017.

[33] J. E. Turney, E. S. Landry, A. J. H. McGaughey, and C. H. Amon, "Predicting phonon properties and thermal conductivity from anharmonic lattice dynamics calculations and molecular dynamics simulations," *Physical Review B - Condensed Matter and Materials Physics*, vol. 79, no. 6, pp. 1–12, 2009.

[34] A. Carreras, A. Togo, and I. Tanaka, "DynaPhoPy: A code for extracting phonon quasiparticles from molecular dynamics simulations," *Computer Physics Communications*, vol. 221, pp. 221–234, 2017.

[35] M. Tuckerman, B. B. J., and M. G. J., "Reversible multiple time scale molecular dynamics," *The Journal of Chemical Physics*, vol. 97, no. 3, pp. 1990–2001, 1992.

[36] M. E. Tuckerman, J. Alejandre, R. López-Rendón, A. L. Jochim, and G. J. Martyna, "A Liouville-operator derived measure-preserving integrator for molecular dynamics simulations in the isothermal-isobaric ensemble," *Journal of Physics A: Mathematical and General*, vol. 39, no. 19, pp. 5629–5651, 2006.

[37] W. G. Hoover, "Canonical dynamics: Equilibrium phase-space distributions," *Phys. Rev. A*, vol. 31, pp. 1695–1697, Mar 1985.

[38] D. J. Evans and B. L. Holian, "The Nose-Hoover thermostat," *The Journal of Chemical Physics*, vol. 83, no. 8, pp. 4069–4074, 1985.

[39] G. J. Martyna, M. L. Klein, and M. Tuckerman, "Nosé-Hoover chains: The canonical ensemble via continuous dynamics," *The Journal of Chemical Physics*, vol. 97, no. 4, pp. 2635–2643, 1992.

[40] O. N. Bedoya-Martínez, J. L. Barrat, and D. Rodney, "Computation of the thermal conductivity using methods based on classical and quantum molecular dynamics," *Physical Review B - Condensed Matter and Materials Physics*, vol. 89, no. 1, pp. 1–7, 2014.

[41] M. Ceriotti, G. Bussi, and M. Parrinello, "Nuclear quantum effects in solids using a colored-noise thermostat," *Physical Review Letters*, vol. 103, no. 3, pp. 1–4, 2009.

[42] P. Jund and R. Jullien, "Molecular-dynamics calculation of the thermal conductivity of vitreous silica," *Physical Review B - Condensed Matter and Materials Physics*, vol. 59, no. 21, pp. 13707–13711, 1999.

[43] F. Müller-Plathe, "A simple nonequilibrium molecular dynamics method for calculating the thermal conductivity," *The Journal of Chemical Physics*, vol. 106, no. 14, pp. 6082–6085, 1997.

[44] C. Pastorino, T. Kreer, M. Müller, and K. Binder, "Comparison of dissipative particle dynamics and Langevin thermostats for out-of-equilibrium simulations of polymeric systems," *Physical Review E - Statistical, Nonlinear, and Soft Matter Physics*, vol. 76, no. 2, pp. 1–10, 2007.

[45] R. Kubo, "The fluctuation-dissipation theorem," *Rep. Prog. Phys.*, vol. 29, pp. 255–283, 1966.

[46] R. Zwanzig, "TIME-CORRELATION FUNCTIONS AND TRANSPORT COEFFICIENTS IN STATISTICAL MECHANICSl National Bureau of Standards, Washington,," *Annu. Rev. Phys. Chem.*, vol. 16, pp. 67–102, 1964.

[47] J. Che, T. Çain, W. Deng, and W. A. Goddard, "Thermal conductivity of diamond and related materials from molecular dynamics simulations," *Journal of Chemical Physics*, vol. 113, no. 16, pp. 6888–6900, 2000.

[48] S. Bureekaew, S. Amirjalayer, M. Tafipolsky, C. Spickermann, T. K. Roy, and R. Schmid, "MOF-FF - A flexible first-principles derived force field for metal-organic frameworks," *Physica Status Solidi (B) Basic Research*, vol. 250, no. 6, pp. 1128–1141, 2013.

[49] N. L. Allinger, Y. H. Yuh, and J. H. Lii, "Molecular Mechanics. The MM3 Force Field for Hydrocarbons. 1," *Journal of the American Chemical Society*, vol. 111, no. 23, pp. 8551–8566, 1989.

[50] G. Kresse and J. Furthmüller, "Efficient iterative schemes for ab initio total-energy calculations using a plane-wave basis set," *Physical Review B - Condensed Matter and Materials Physics*, vol. 54, no. 16, pp. 11169–11186, 1996.

[51] J. P. Dürholt, G. Fraux, F. X. Coudert, and R. Schmid, "Ab Initio Derived Force Fields for Zeolitic Imidazolate Frameworks: MOF-FF for ZIFs," *Journal of Chemical Theory and Computation*, vol. 15, no. 4, pp. 2420–2432, 2019.

[52] C. Campañá, B. Mussard, and T. K. Woo, "Electrostatic potential derived atomic charges for periodic systems using a modified error functional," *Journal of Chemical Theory and Computation*, vol. 5, no. 10, pp. 2866–2878, 2009.

[53] N. Hansen, *The CMA Evolution Strategy: A Comparing Review*, pp. 75–102. Berlin, Heidelberg: Springer Berlin Heidelberg, 2006.

[54] C. J. Tainter and G. C. Schatz, "Reactive Force Field Modeling of Zinc Oxide Nanoparticle Formation," *Journal of Physical Chemistry C*, vol. 120, no. 5, pp. 2950–2961, 2016.

[55] Y.-R. Luo, *Comprehensive Handbook of Chemical Bond Energies*. CRC Press, 2007.

[56] H. Sun, "COMPASS: An ab Initio Force-Field Optimized for Condensed-Phase ApplicationsOverview with Details on Alkane and Benzene Compounds," *The Journal of Physical Chemistry B*, vol. 102, no. 38, pp. 7338–7364, 2002.

[57] H. W. Kuhn, "The hungarian method for the assignment problem," *Naval Research Logistics Quarterly*, vol. 2, no. 12, pp. 83–97, 1955.

[58] A. Togo and I. Tanaka, "First principles phonon calculations in materials science," *Scripta Materialia*, vol. 108, pp. 1–5, 2015.

[59] Steve Plimton, "Fast Parallel Algorithms for Short-Range Molecular Dynamics," *Journal of Computational Physics*, vol. 117, no. 1, pp. 1–19, 1995.

[60] R. Hockney, *Computer Simulation Using Particles*. CRC Press, 1988.

[61] L. D. S. Oliveira and P. A. Greaney, "Method to manage integration error in the Green-Kubo method," *Physical Review E*, vol. 95, no. 2, pp. 1–11, 2017.

[62] B. L. Huang, A. J. McGaughey, and M. Kaviany, "Thermal conductivity of metal-organic framework 5 (MOF-5): Part I. Molecular dynamics simulations," *International Journal of Heat and Mass Transfer*, vol. 50, no. 3-4, pp. 393–404, 2007.

[63] D. P. Sellan, E. S. Landry, J. E. Turney, A. J. H. McGaughey, and C. H. Amon, "Size effects in molecular dynamics thermal conductivity predictions," *Phys. Rev. B*, vol. 81, p. 214305, Jun 2010.

[64] W. Setyawan and S. Curtarolo, "High-throughput electronic band structure calculations: Challenges and tools," *Computational Materials Science*, vol. 49, no. 2, pp. 299–312, 2010.

[65] P. G. Boyd, S. M. Moosavi, M. Witman, and B. Smit, "Force-Field Prediction of Materials Properties in Metal-Organic Frameworks," *Journal of Physical Chemistry Letters*, vol. 8, no. 2, pp. 357–363, 2017.

[66] N. Lock, M. Christensen, Y. Wu, V. K. Peterson, M. K. Thomsen, R. O. Piltz, A. J. Ramirez-Cuesta, G. J. McIntyre, K. Norén, R. Kutteh, C. J. Kepert, G. J. Kearley, and B. B. Iversen, "Scrutinizing negative thermal expansion in MOF-5 by scattering techniques and ab initio calculations," *Journal of the Chemical Society. Dalton Transactions*, vol. 42, no. 2, pp. 1996–2007, 2013.

[67] W. Zhou, H. Wu, T. Yildirim, J. R. Simpson, and A. R. Walker, "Origin of the exceptional negative thermal expansion in metal-organic framework-5 Zn4 O (1,4-benzenedicarboxylate)3," *Physical Review B - Condensed Matter and Materials Physics*, vol. 78, no. 5, pp. 1–5, 2008.

[68] L. H. Rimmer, M. T. Dove, A. L. Goodwin, and D. C. Palmer, "Acoustic phonons and negative thermal expansion in MOF-5," *Physical Chemistry Chemical Physics*, vol. 16, no. 39, pp. 21144–21152, 2014.

[69] K. D. Hammonds, M. T. Dove, A. P. Giddy, V. Heine, and B. Winkler, "Rigid-unit phonon modes and structural phase transitions in framework silicates," *American Mineralogist*, vol. 81, no. 9-10, pp. 1057–1079, 1996.

[70] O. M. Yaghi, M. O'Keeffe, M. Eddaoudi, and H. Li, "Design and synthesis of an exceptionally stable and highly," *Nature*, vol. 402, no. November, pp. 276–279, 1999.

[71] J. Purewal, D. Liu, A. Sudik, M. Veenstra, J. Yang, S. Maurer, U. Müller, and D. J. Siegel, "Improved hydrogen storage and thermal conductivity in high-density MOF-5 composites," *Journal of Physical Chemistry C*, vol. 116, no. 38, pp. 20199–20212, 2012.

[72] D. Liu, J. J. Purewal, J. Yang, A. Sudik, S. Maurer, U. Mueller, J. Ni, and D. J. Siegel, "MOF-5 composites exhibiting improved thermal conductivity," *International Journal of Hydrogen Energy*, vol. 37, no. 7, pp. 6109–6117, 2012.

[73] A. J. McGaughey and M. Kaviany, "Thermal conductivity decomposition and analysis using molecular dynamics simulations Part II. Complex silica structures," *International Journal of Heat and Mass Transfer*, vol. 47, no. 8-9, pp. 1799–1816, 2004.

[74] K. B. Sezginel, P. A. Asinger, H. Babaei, and C. E. Wilmer, "Thermal Transport in Interpenetrated Metal-Organic Frameworks," *Chemistry of Materials*, vol. 30, no. 7, pp. 2281–2286, 2018.

[75] H. Babaei and C. E. Wilmer, "Mechanisms of Heat Transfer in Porous Crystals Containing Adsorbed Gases: Applications to Metal-Organic Frameworks," *Physical Review Letters*, vol. 116, no. 2, pp. 1–6, 2016.

[76] K. H. Lin and A. Strachan, "Thermal transport in SiGe superlattice thin films and nanowires: Effects of specimen and periodic lengths," *Physical Review B - Condensed Matter and Materials Physics*, vol. 87, no. 11, pp. 1–9, 2013.

[77] H. Babaei, A. J. McGaughey, and C. E. Wilmer, "Effect of pore size and shape on the thermal conductivity of metal-organic frameworks," *Chemical Science*, vol. 8, no. 1, pp. 583–589, 2016.

[78] M. Omini and A. Sparavigna, "Beyond the isotropic-model approximation in the theory of thermal conductivity," *Phys. Rev. B*, vol. 53, pp. 9064–9073, Apr 1996.

[79] D. A. Broido, A. Ward, and N. Mingo, "Lattice thermal conductivity of silicon from empirical interatomic potentials," *Physical Review B - Condensed Matter and Materials Physics*, vol. 72, no. 1, pp. 1–8, 2005.

[80] L. Chaput, "Direct solution to the linearized phonon boltzmann equation," *Physical Review Letters*, vol. 110, no. 26, pp. 1–5, 2013.

[81] A. Weathers, J. Carrete, J. P. Degrave, J. M. Higgins, A. L. Moore, J. Kim, N. Mingo, S. Jin, and L. Shi, "Glass-like thermal conductivity in nanostructures of a complex anisotropic crystal," *Physical Review B*, vol. 96, no. 21, pp. 1–7, 2017.

[82] W. Li and N. Mingo, "Ultralow lattice thermal conductivity of the fully filled skutterudite YbFe<inf>4</inf>Sb<inf>12</inf> due to the flat avoided-crossing filler modes," *Physical Review B - Condensed Matter and Materials Physics*, vol. 91, no. 14, pp. 1–6, 2015.

[83] X. Chen, A. Weathers, J. Carrete, S. Mukhopadhyay, O. Delaire, D. A. Stewart, N. Mingo, S. N. Girard, J. Ma, D. L. Abernathy, J. Yan, R. Sheshka, D. P. Sellan, F. Meng, S. Jin, J. Zhou, and L. Shi, "Twisting phonons in complex crystals with quasi-one-dimensional substructures," *Nature Communications*, vol. 6, 2015.

[84] W. Lee, H. Li, A. B. Wong, D. Zhang, M. Lai, Y. Yu, Q. Kong, E. Lin, J. J. Urban, J. C. Grossman, and P. Yang, "Ultralow thermal conductivity in all-inorganic halide perovskites," *Proceedings of the National Academy of Sciences*, vol. 114, no. 33, pp. 8693–8697, 2017.

[85] S. Mukhopadhyay, A. A. Puretzky, M. A. McGuire, L. Lindsay, B. C. Sales, and D. S. Parker, " Two-channel model for ultralow thermal conductivity of crystalline Tl 3 VSe 4 ," *Science*, vol. 360, no. 6396, pp. 1455–1458, 2018.

[86] M. Simoncelli, N. Marzari, and F. Mauri, "Unified theory of thermal transport in crystals and disordered solids," *Nature Physics*, 2019.

[87] M. Puligheddu, Y. Xia, M. Chan, and G. Galli, "Computational prediction of lattice thermal conductivity-a comparison of molecular dynamics and Boltzmann transport approaches," 2019.

[88] X. Wang, R. Guo, D. Xu, J. Chung, M. Kaviany, and B. Huang, "Anisotropic Lattice Thermal Conductivity and Suppressed Acoustic Phonons in MOF-74 from First Principles," *Journal of Physical Chemistry C*, vol. 119, no. 46, pp. 26000–26008, 2015.

[89] T. Kamencek, N. Bedoya-martínez, and E. Zojer, "Understanding Phonon Properties in Isoreticular Metal- Organic Frameworks from First Principles," *arXiv:1907.02508 [cond-mat.mtrl-sci]*, 2019.

[90] B. Aradi, B. Hourahine, and T. Frauenheim, "DFTB+, a sparse matrix-based implementation of the DFTB method," *Journal of Physical Chemistry A*, vol. 111, no. 26, pp. 5678–5684, 2007.

[91] S. Grimme, J. Antony, S. Ehrlich, and H. Krieg, "A consistent and accurate ab initio parametrization of density functional dispersion correction (DFT-D) for the 94 elements H-Pu," *Journal of Chemical Physics*, vol. 132, no. 15, 2010.

# List of Figures

# List of Tables

# A Reference data

This section should give an overview of the methods used to obtain the DFT and DFTB reference data used for parameterization of force fields and as validation for existing force fields.

The DFT and DFTB calculations were carried out by Tomas Kamencek, similarly to what is described in [89]. The programs used were the Vienna ab-initio software package (VASP) [50] and DFTB+ [90]. DFT was employed for primitive unit cells of IRMOF-1 (Zn), IRMOF-1(Mg), IRMOF-130 (Mg) and MOF-74 (Zn) using the PBE functional and utilizing the projector-augmented wave method. The k-mesh was converged until a total energy difference of less than 1 meV was achieved. A tight SCF convergence criterion of $10^{-8}$ eV was chosen. Relaxations were performed until the maximum forces in the system reached 0.5 meV/Å. No van der Waals correction was deemed necessary for the IRMOFs. For MOF-74 the D3 correction method [91] was applied.

For DFTB the 3ob:freq-1-2 Slater-Koster files were used to properly describe vibrational properties. The k-mesh for each system was chosen with the same criteria, as in DFT. The SCC convergence criterion was set to $10^{-10}$ elementary charges and the maximum forces during relaxation were set to $10^{-5}$ meV/Å. DFTB was used to evaluate phonon band structures and the third order force constants for IRMOF-130 and MOF-74.

# B Force-field parameters

Here the parameterized force-fields used in this work are shown in the form of tables. For atomic charges see section 4.1 and for van-der-Waals parameters the MM3 force-field.

## B.1 IRMOF-1 (Mg)

Table B.1: Bond parameters for connected atoms in IRMOF-1 (Mg). $r_s$ ... Reference bond length, $k_s$ ... force constant, $E_{diss}$ ... Bond dissociation energy for Morse potentials.

| **Bond** | $\mathbf{r_s}$[Å] | $\mathbf{k_s}$[mdyn/Å] | $\mathbf{E_{diss}}$[kcal/mol] |
|---|---|---|---|
| Mg-$O_{cen}$ | 2.01036169 | 1.15286343 | 85.0 |
| Mg-$O_{out}$ | 1.99417052 | 1.79296394 | 85.0 |
| $C_{C1O2}$-$O_{out}$ | 1.28675619 | 7.74846928 | |
| $C_{C1O2}$-$C_{C3}$ | 1.48511909 | 4.56714248 | |
| $C_{C2H1}$-$C_{C3}$ | 1.41518966 | 5.82475434 | |
| $C_{C2H1}$-$C_{C2H1}$ | 1.41064962 | 5.96623482 | |
| $C_{C2H1}$-H | 1.09829203 | 5.02135354 | |

Table B.2: Angle bending parameters for connected atoms in IRMOF-1 (Mg). $\theta_b$ ... Reference angle, $k_b$ ... force constant.

| **Angle** | $\theta_\mathbf{b}[^\circ]$ | $\mathbf{k_b}$**[mdyn/(radÅ)]** |
|---|---|---|
| Mg-$O_{cen}$-Mg | 110.50567581 | 1.12998636 |
| $O_{out}$-Mg-$O_{cen}$ | 99.64152095 | 1.79296394 |
| $O_{out}$-Mg-$O_{out}$ | 119.29104787 | 0.31220519 |
| $C_{C1O2}$-$O_{out}$-Mg | 147.29199688 | 0.07237911 |
| $C_{C2H1}$-$C_{C2H1}$-$C_{C3}$ | 112.06192132 | 1.40627103 |
| $C_{C2H1}$-$C_{C3}$-$C_{C2H1}$ | 108.28474697 | 1.51252861 |
| $C_{C1O2}$-$C_{C3}$-$C_{C2H1}$ | 111.18049223 | 1.17134274 |
| $C_{C3}$-$C_{C2H1}$-H | 111.54321086 | 0.59966987 |
| $C_{C2H1}$-$C_{C2H1}$-H | 114.91286252 | 0.57914588 |
| $C_{C3}$-$C_{C1O2}$-$O_{out}$ | 117.29187353 | 0.78310379 |
| $O_{out}$-$C_{C1O2}$-$O_{out}$ | 127.83452571 | 1.12360472 |

Table B.3: Stretch-stretch and stretch-bend parameters for the angles in IRMOF-1 (Mg). $k_{sb1}$ and $k_{sb2}$ ... Force constants for the stretch-bend terms, $k_{ss}$ ... force constants for the stretch-stretch terms. The terms from missing angles are 0.

| **Angle** | $\mathbf{k_{sb1}}$**[mdyn/(radÅ)]** | $\mathbf{k_{sb2}}$**[mdyn/(radÅ)]** | $\mathbf{k_{ss}}$**[mdyn/(Å)]** |
|---|---|---|---|
| Mg-$O_{cen}$-Mg | 0.57627914 | 0.57609350 | 0.00000000 |
| $O_{out}$-Mg-$O_{cen}$ | -0.06340321 | 0.20220109 | 0.01238360 |
| $C_{C2H1}$-$C_{C2H1}$-$C_{C3}$ | 0.42845698 | 0.38533807 | 0.61884682 |
| $C_{C2H1}$-$C_{C3}$-$C_{C2H1}$ | 0.33214504 | 0.33215837 | 0.58646530 |
| $C_{C3}$-$C_{C2H1}$-H | 0.14640386 | 0.20182070 | 0.04431180 |
| $C_{C2H1}$-$C_{C2H1}$-H | 0.19867862 | 0.16166101 | 0.05463335 |

Table B.4: Dihedral parameters for IRMOF-1 (Mg). $V_1$, $V_2$ and $V_3$ ... parameters. The terms from missing dihedrals are 0.

| **Dihedral** | $\mathbf{V_1}$**[kcal/mol]** | $\mathbf{V_2}$**[kcal/mol]** | $\mathbf{V_3}$**[kcal/mol]** |
|---|---|---|---|
| $C_{C3}$-$C_{C2H1}$-$C_{C2H1}$-$C_{C3}$ | 0.00000000 | 13.49268313 | 0.00000000 |
| $O_{out}$-$C_{C1O2}$-$O_{out}$-Mg | 0.00000000 | 1.36629066 | 0.00000000 |
| $C_{C3}$-$C_{C1O2}$-$O_{out}$-Mg | 0.00000000 | 7.61023423 | 0.00000000 |
| $C_{C3}$-$C_{C2H1}$-$C_{C2H1}$-H | 0.00000000 | 6.79045908 | 0.00000000 |
| $O_{out}$-$C_{C1O2}$-$C_{C3}$-$C_{C2H1}$ | 0.00000000 | 2.13421217 | 0.00000000 |
| $C_{C2H1}$-$C_{C2H1}$-$C_{C3}$-$C_{C2H1}$ | 0.00000000 | 8.77269646 | 0.00000000 |
| H-$C_{C2H1}$-$C_{C2H1}$-H | 0.00000000 | 4.33887262 | 0.00000000 |
| H-$C_{C2H1}$-$C_{C3}$-$C_{C2H1}$ | 0.00000000 | 7.67004885 | 0.00000000 |

Table B.5: Out-of-plane angle bending parameters (improper torsions) for IRMOF-1 (Mg). $k_o$ ... force constant.

| **Improper torsion** | $\mathbf{k_o}$**[mdyn/(radÅ)]** |
|---|---|
| $C_{C1O2}$-$C_{C3}$-$O_{out}$-$O_{out}$ | 0.14835983 |
| $C_{C2H1}$-$C_{C2H1}$-$C_{C3}$-H | 0.05196597 |
| $C_{C3}$-$C_{C1O2}$-$C_{C2H1}$-$C_{C2H1}$ | 0.10189007 |

## B.2 IRMOF-130 (Mg)

Table B.6: Bond parameters for connected atoms in IRMOF-130 (Mg). $r_s$ ... Reference bond length, $k_s$ ... force constant, $E_{diss}$ ... Bond dissociation energy for Morse potentials.

| **Bond** | $\mathbf{r_s}$[Å] | $\mathbf{k_s}$[mdyn/Å] | $\mathbf{E_{diss}}$[kcal/mol] |
|---|---|---|---|
| Mg-$O_{cen}$ | 1.99445588 | 1.24207899 | 85.0 |
| Mg-$O_{out}$ | 1.88582422 | 1.93133858 | 85.0 |
| $C_{C1O2}$-$O_{out}$ | 1.29764291 | 7.42726309 | |
| $C_{C1O2}$-$C_{C1O2}$ | 1.57936705 | 2.86336307 | |

Table B.7: Angle bending parameters for connected atoms in IRMOF-130 (Mg). $\theta_b$ ... Reference angle, $k_b$ ... Force constant.

| **Angle** | $\theta_\mathbf{b}$[°] | $\mathbf{k_b}$[mdyn/(radÅ)] |
|---|---|---|
| Mg-$O_{cen}$-Mg | 132.79175545 | 0.14776141 |
| $O_{out}$-Mg-$O_{cen}$ | 106.75401570 | 0.00000009 |
| $O_{out}$-Mg-$O_{out}$ | 97.90228444 | 0.37011506 |
| $C_{C1O2}$-$O_{out}$-Mg | 191.26400031 | 0.00774540 |
| $C_{C1O2}$-$C_{C1O2}$-$O_{out}$ | 105.76300318 | 1.59667765 |
| $O_{out}$-$C_{C1O2}$-$O_{out}$ | 118.75348997 | 1.78129974 |

Table B.8: Stretch-stretch and stretch-bend parameters for the angles in IRMOF-130 (Mg). $k_{sb1}$ and $k_{sb2}$ ... Force constants for the stretch-bend terms, $k_{ss}$ ... force constants for the stretch-stretch terms. The terms from missing angles are 0.

| **Angle** | $\mathbf{k_{sb1}}$**[mdyn/(radÅ)]** | $\mathbf{k_{sb2}}$**[mdyn/(radÅ)]** | $\mathbf{k_{ss}}$**[mdyn/(Å)]** |
|---|---|---|---|
| Mg-$O_{cen}$-Mg | 0.13691557 | 0.13691926 | 0.13486124 |
| $O_{out}$-Mg-$O_{cen}$ | 0.04451345 | 0.04824827 | -0.00289273 |
| $O_{out}$-Mg-$O_{out}$ | 0.09002539 | 0.09006589 | 0.06748314 |
| $C_{C1O2}$-$O_{out}$-Mg | 0.00419795 | 0.18071148 | 0.16113295 |
| $C_{C1O2}$-$C_{C1O2}$-$O_{out}$ | 0.28119052 | 0.53551591 | 0.41058151 |
| $O_{out}$-$C_{C1O2}$-$O_{out}$ | 0.55967775 | 0.55964721 | 1.27970281 |

Table B.9: Dihedral parameters for IRMOF-130 (Mg). $V_1$, $V_2$ and $V_3$ ... force constants. The terms from missing dihedrals are 0.

| **Dihedral** | $\mathbf{V_1}$**[kcal/mol]** | $\mathbf{V_2}$**[kcal/mol]** | $\mathbf{V_3}$**[kcal/mol]** |
|---|---|---|---|
| $O_{out}$-$C_{C1O2}$-$C_{C1O2}$-$O_{out}$ | 0.00000000 | -0.64117613 | 0.00000000 |
| $C_{C1O2}$-$C_{C1O2}$-$O_{out}$-Mg | 0.00000000 | 0.21142793 | 0.00000000 |

Table B.10: End-bond-torsion parameters for dihedrals in IRMOF-130 (Mg). $A_2$ and $B_2$ ... parameters. The terms from missing dihedrals and all missing terms are 0.

| **Dihedral** | $\mathbf{A_2}$**[kcal/(molÅ)]** | $\mathbf{B_2}$**[kcal/(molÅ)]** |
|---|---|---|
| $O_{out}$-$C_{C1O2}$-$C_{C1O2}$-$O_{out}$ | 8.22007371 | 8.22007371 |
| $C_{C1O2}$-$C_{C1O2}$-$O_{out}$-Mg | -4.41418973 | -2.21661577 |

Table B.11: Out-of-plane angle bending parameters (improper torsions) for IRMOF-130 (Mg). $k_o$ ... force constant.

| **Improper torsion** | $\mathbf{k_o}$**[mdyn/(radÅ)]** |
|---|---|
| $C_{C1O2}$-$C_{C1O2}$-$O_{out}$-$O_{out}$ | 0.22431476 |

## B.3 MOF-74 (Zn)

Table B.12: Bond parameters for connected atoms in MOF-74 (Zn). $r_s$ ... Reference bond length, $k_s$ ... force constant, $E_{diss}$ ... Bond dissociation energy for Morse potentials.

| **Bond** | $\mathbf{r_s}$[Å] | $\mathbf{k_s}$[mdyn/Å] | $\mathbf{E_{diss}}$[kcal/mol] |
|---|---|---|---|
| $C_{c2h1}$-$C_{c2o1}$ | 1.3775 | 7.1595 | |
| $O_{co2,1}$-Zn | 2.8610 | 0.2763 | 50.0000 |
| $C_{c2h1}$-$C_{c3}$ | 1.3954 | 6.4078 | |
| $O_{co2,2}$-Zn | 2.1599 | 0.7221 | 50.0000 |
| $C_{c2o1}$-$C_{c3}$ | 1.3894 | 6.5921 | |
| $C_{c2o1}$-$O_{eth}$ | 1.3377 | 6.3550 | |
| $C_{c1o2}$-$O_{co2,1}$ | 1.2716 | 8.3498 | |
| $O_{eth}$-Zn | 1.9236 | 2.0695 | 50.0000 |
| $C_{c1o2}$-$O_{co2,2}$ | 1.3154 | 6.3771 | |
| $C_{c2h1}$-H | 1.0880 | 5.3917 | |
| $C_{c1o2}$-$C_{c3}$ | 1.4972 | 3.7384 | |

Table B.13: Angle bending parameters for connected atoms in MOF-74 (Zn). $\theta_b$ ... Reference angle, $k_b$ ... Force constant.

| **Angle** | $\theta_\mathbf{b}[^\circ]$ | $\mathbf{k_b}[\mathbf{mdyn/(radÅ)}]$ |
|---|---|---|
| $C_{c2o1}$-$O_{eth}$-Zn | 174.3465 | 0.0082 |
| $C_{c1o2}$-$O_{co2,1}$-Zn | 123.4995 | 0.4385 |
| Zn-$O_{co2,2}$-Zn | 87.0004 | 0.0028 |
| $O_{co2,1}$-Zn-$O_{eth}$ | 87.6515 | 0.0087 |
| $O_{co2,2}$-Zn-$O_{eth}$ | 100.1621 | 0.2633 |
| $O_{co2,2}$-Zn-$O_{co2,2}$ | 74.9249 | 1.1250 |
| $C_{c3}$-$C_{c2o1}$-$O_{eth}$ | 123.8706 | 0.7325 |
| Zn-$O_{eth}$-Zn | 92.2765 | 0.0000 |
| $C_{c2o1}$-$C_{c2h1}$-H | 109.1652 | 0.6036 |
| $C_{c2h1}$-$C_{c2o1}$-$O_{eth}$ | 118.8209 | 1.0640 |
| $C_{c2h1}$-$C_{c3}$-$C_{c2o1}$ | 123.1528 | 0.3927 |
| $C_{c2h1}$-$C_{c2o1}$-$C_{c3}$ | 134.8132 | 0.2811 |
| $C_{c2o1}$-$C_{c2h1}$-$C_{c3}$ | 123.4399 | 0.9547 |
| $O_{eth}$-Zn-$O_{eth}$ | 159.6772 | 0.0002 |
| $C_{c3}$-$C_{c2h1}$-H | 108.2754 | 0.6605 |
| $O_{co2,1}$-Zn-$O_{co2,2}$ | 69.6984 | 0.0191 |
| $O_{co2,1}$-$C_{c1o2}$-$O_{co2,2}$ | 124.1020 | 0.9313 |
| $C_{c3}$-$C_{c1o2}$-$O_{co2,2}$ | 119.4340 | 0.9587 |
| $C_{c1o2}$-$C_{c3}$-$C_{c2h1}$ | 110.6332 | 1.0055 |
| $C_{c3}$-$C_{c1o2}$-$O_{co2,1}$ | 107.6835 | 1.1007 |
| $C_{c1o2}$-$O_{co2,2}$-Zn | 138.4175 | 0.1827 |
| $C_{c1o2}$-$C_{c3}$-$C_{c2o1}$ | 122.7555 | 1.0184 |

Table B.14: Stretch-stretch and stretch-bend parameters for the angles in MOF-74 (Zn). $k_{sb1}$ and $k_{sb2}$ ... Force constants for the stretch-bend terms, $k_{ss}$ ... force constants for the stretch-stretch terms. The terms from missing angles are 0.

| **Angle** | $\mathbf{k_{sb1}}$**[mdyn/(radÅ)]** | $\mathbf{k_{sb2}}$**[mdyn/(radÅ)]** | $\mathbf{k_{ss}}$**[mdyn/(Å)]** |
|---|---|---|---|
| $C_{c2o1}$-$O_{eth}$-Zn | 0.0409 | -0.0617 | 0.1485 |
| $C_{c1o2}$-$O_{co2,1}$-Zn | -0.5563 | 0.1807 | 0.5136 |
| Zn-$O_{co2,2}$-Zn | -0.1420 | -0.1515 | 0.3057 |
| $O_{co2,1}$-Zn-$O_{eth}$ | 0.0981 | 0.2357 | 0.1906 |
| $O_{co2,2}$-Zn-$O_{co2,2}$ | 0.2703 | 0.2701 | -0.0594 |
| Zn-$O_{eth}$-Zn | -0.1189 | -0.1571 | 0.3111 |
| $C_{c2h1}$-$C_{c2o1}$-$C_{c3}$ | 0.4099 | 0.3737 | 0.5420 |
| $O_{eth}$-Zn-$O_{eth}$ | -0.1250 | -0.1267 | 0.0062 |
| $O_{co2,1}$-Zn-$O_{co2,2}$ | 0.1984 | -0.0623 | -0.0814 |
| $C_{c3}$-$C_{c1o2}$-$O_{co2,2}$ | 0.3278 | 0.4030 | 0.4186 |
| $C_{c3}$-$C_{c1o2}$-$O_{co2,1}$ | 0.5810 | 1.1900 | 0.5931 |
| $C_{c1o2}$-$O_{co2,2}$-Zn | -0.1046 | 0.1400 | 0.3061 |

Table B.15: Dihedral parameters for MOF-74 (Zn). $V_1$, $V_2$ and $V_3$ ... force constants. The terms from missing dihedrals are 0.

| **Dihedral** | $\mathbf{V_1}$[**kcal/mol**] | $\mathbf{V_2}$[**kcal/mol**] | $\mathbf{V_3}$[**kcal/mol**] |
|---|---|---|---|
| $C_{c2o1}$-$O_{eth}$-Zn-$O_{eth}$ | 0.0000 | 0.0053 | 0.0000 |
| $O_{co2,2}$-$C_{c1o2}$-$C_{c3}$-$C_{c2h1}$ | 0.0000 | 0.7933 | 0.0000 |
| Zn-$O_{co2,2}$-Zn-$O_{co2,2}$ | 0.0000 | 14.5406 | 0.0000 |
| $O_{co2,1}$-$C_{c1o2}$-$O_{co2,2}$-Zn | 0.0000 | 0.1391 | 0.0000 |
| H-$C_{c2h1}$-$C_{c3}$-$C_{c1o2}$ | 0.0000 | 8.7746 | 0.0000 |
| $O_{eth}$-$C_{c2o1}$-$C_{c3}$-$C_{c2h1}$ | 0.0000 | 14.9927 | 0.0000 |
| Zn-$O_{co2,2}$-Zn-$O_{eth}$ | 0.0000 | 0.0231 | 0.0000 |
| Zn-$O_{eth}$-Zn-$O_{eth}$ | 0.0000 | 0.0776 | 0.0000 |
| $O_{co2,2}$-$C_{c1o2}$-$C_{c3}$-$C_{c2o1}$ | 0.0000 | 0.0114 | 0.0000 |
| $O_{co2,1}$-$C_{c1o2}$-$C_{c3}$-$C_{c2h1}$ | 0.0000 | 0.8910 | 0.0000 |
| $C_{c2o1}$-$C_{c2h1}$-$C_{c3}$-$C_{c1o2}$ | 0.0000 | 1.7449 | 0.0000 |
| $C_{c1o2}$-$O_{co2,1}$-Zn-$O_{eth}$ | 0.0000 | 0.0450 | 0.0000 |
| $C_{c1o2}$-$O_{co2,1}$-Zn-$O_{co2,2}$ | 0.0000 | 0.0029 | 0.0000 |
| $C_{c1o2}$-$O_{co2,2}$-Zn-$O_{co2,2}$ | 0.0000 | 0.4415 | 0.0000 |
| H-$C_{c2h1}$-$C_{c2o1}$-$C_{c3}$ | 0.0000 | 1.0082 | 0.0000 |
| $C_{c1o2}$-$O_{co2,2}$-Zn-$O_{eth}$ | 0.0000 | 0.0168 | 0.0000 |
| $O_{co2,2}$-$C_{c1o2}$-$O_{co2,1}$-Zn | 0.0000 | 0.0058 | 0.0000 |
| Zn-$O_{eth}$-Zn-$O_{co2,2}$ | 0.0000 | 0.1441 | 0.0000 |
| $O_{eth}$-$C_{c2o1}$-$C_{c3}$-$C_{c1o2}$ | 0.0000 | 2.2724 | 0.0000 |
| $C_{c3}$-$C_{c2h1}$-$C_{c2o1}$-$C_{c3}$ | 0.0000 | 8.0191 | 0.0000 |
| Zn-$O_{co2,2}$-Zn-$O_{co2,1}$ | 0.0000 | 1.8444 | 0.0000 |
| H-$C_{c2h1}$-$C_{c2o1}$-$O_{eth}$ | 0.0000 | 10.3863 | 0.0000 |
| $C_{c2o1}$-$C_{c2h1}$-$C_{c3}$-$C_{c2o1}$ | 0.0000 | 5.7923 | 0.0000 |
| $C_{c2o1}$-$O_{eth}$-Zn-$O_{co2,2}$ | 0.0000 | 0.0006 | 0.0000 |
| $C_{c3}$-$C_{c2h1}$-$C_{c2o1}$-$O_{eth}$ | 0.0000 | 1.8192 | 0.0000 |
| H-$C_{c2h1}$-$C_{c3}$-$C_{c2o1}$ | 0.0000 | 4.0828 | 0.0000 |
| $C_{c2h1}$-$C_{c2o1}$-$C_{c3}$-$C_{c2h1}$ | 0.0000 | 2.3366 | 0.0000 |
| $C_{c2h1}$-$C_{c2o1}$-$O_{eth}$-Zn | 0.0000 | 1.1300 | 0.0000 |
| $O_{co2,1}$-$C_{c1o2}$-$C_{c3}$-$C_{c2o1}$ | 0.0000 | 0.0004 | 0.0000 |
| $C_{c3}$-$C_{c1o2}$-$O_{co2,2}$-Zn | 0.0000 | 6.7641 | 0.0000 |
| $C_{c2h1}$-$C_{c2o1}$-$C_{c3}$-$C_{c1o2}$ | 0.0000 | 7.4030 | 0.0000 |
| $C_{c2o1}$-$O_{eth}$-Zn-$O_{co2,1}$ | 0.0000 | 0.0114 | 0.0000 |
| $C_{c3}$-$C_{c2o1}$-$O_{eth}$-Zn | 0.0000 | 1.0804 | 0.0000 |
| $C_{c1o2}$-$O_{co2,2}$-Zn-$O_{co2,1}$ | 0.0000 | 0.0018 | 0.0000 |

Table B.16: Out-of-plane angle bending parameters (improper torsions) for MOF-74 (Mg). $k_o$ ... force constant, $\theta_\mathbf{0}$ ... reference angle.

| **Improper torsion** | $\mathbf{k_o}$[**mdyn**/(**radÅ**)] | $\theta_\mathbf{0}$[°] |
|---|---|---|
| $O_{eth}$-$C_{c2o1}$-Zn-Zn | 0.0002 | 51.6343 |
| $O_{co2,2}$-$C_{c1o2}$-Zn-Zn | 0.0000 | 45.0048 |
| $C_{c2o1}$-$C_{c2h1}$-$C_{c3}$-$O_{eth}$ | 0.0359 | 0.0000 |
| $C_{c3}$-$C_{c1o2}$-$C_{c2h1}$-$C_{c2o1}$ | 0.0397 | 0.0000 |
| $C_{c1o2}$-$C_{c3}$-$O_{co2,1}$-$O_{co2,2}$ | 0.1798 | 0.0000 |
| $C_{c2h1}$-$C_{c2o1}$-$C_{c3}$-H | 0.0100 | 0.0000 |